



<https://theses.gla.ac.uk/>

Theses Digitisation:

<https://www.gla.ac.uk/myglasgow/research/enlighten/theses/digitisation/>

This is a digitised version of the original print thesis.

Copyright and moral rights for this work are retained by the author

A copy can be downloaded for personal non-commercial research or study, without prior permission or charge

This work cannot be reproduced or quoted extensively from without first obtaining permission in writing from the author

The content must not be changed in any way or sold commercially in any format or medium without the formal permission of the author

When referring to this work, full bibliographic details including the author, title, awarding institution and date of the thesis must be given

Enlighten: Theses

<https://theses.gla.ac.uk/>
research-enlighten@glasgow.ac.uk

DOSE COMPUTATION FOR THERAPEUTIC ELECTRON BEAMS

By

MARTIN MACKENZIE GLEGG BSc, MIPEM

**Thesis submitted to the University of Glasgow for the
degree of Master of Science (Medical Science).**

This work was undertaken at the West of Scotland Health Boards,
Department of Clinical Physics and BioEngineering, Radiotherapy Physics Division,
Beatson Oncology Centre, Western Infirmary, Glasgow.

JUNE 2001

ProQuest Number: 10646010

All rights reserved

INFORMATION TO ALL USERS

The quality of this reproduction is dependent upon the quality of the copy submitted.

In the unlikely event that the author did not send a complete manuscript and there are missing pages, these will be noted. Also, if material had to be removed, a note will indicate the deletion.



ProQuest 10646010

Published by ProQuest LLC (2017). Copyright of the Dissertation is held by the Author.

All rights reserved.

This work is protected against unauthorized copying under Title 17, United States Code
Microform Edition © ProQuest LLC.

ProQuest LLC.
789 East Eisenhower Parkway
P.O. Box 1346
Ann Arbor, MI 48106 – 1346

ABSTRACT

The accuracy of electron dose calculations performed by two commercially available treatment planning computers, Varian Cadplan and Helax TMS, has been assessed. Measured values of absorbed dose delivered by a Varian 2100C linear accelerator, under a wide variety of irradiation conditions, were compared with doses calculated by the treatment planning computers.

Much of the motivation for this work was provided by a requirement to verify the accuracy of calculated electron dose distributions in situations encountered clinically at Glasgow's Beatson Oncology Centre. Calculated dose distributions are required in a significant minority of electron treatments, usually in cases involving treatment to the head and neck. Here, therapeutic electron beams are subject to factors which may cause non-uniformity in the distribution of dose, and which may complicate the calculation of dose. The beam shape is often irregular, the beam may enter the patient at an oblique angle or at an extended source to skin distance (SSD), tissue inhomogeneities can alter the dose distribution, and tissue equivalent material (such as wax) may be added to reduce dose to critical organs.

Technological advances have allowed the current generation of treatment planning computers to implement dose calculation algorithms with the ability to model electron beams in these complex situations. These calculations have, however, yet to be verified by measurement.

This work has assessed the accuracy of calculations in a number of specific instances. Chapter two contains a comparison of measured and calculated planar electron isodose distributions. Three situations were considered: oblique incidence, incidence on an irregular surface (such as that which would be arise from the use of wax to reduce dose to spinal cord), and incidence on a phantom containing a small air cavity. Calculations were compared with measurements made by thermoluminescent dosimetry (TLD) in a WTe electron solid water phantom.

Chapter three assesses the planning computers' ability to model electron beam penumbra at extended SSD. Calculations were compared with diode measurements in a water phantom. Further measurements assessed doses in the junction region produced by abutting an extended SSD electron field with opposed photon fields.

Chapter four describes an investigation of the size and shape of the region enclosed by the 90% isodose line when produced by limiting the electron beam with square and elliptical apertures. The 90% isodose line was chosen because clinical treatments are often prescribed such that a given volume receives at least 90% dose. Calculated and measured dose distributions were compared in a plane normal to the beam central axis. Measurements were made by film dosimetry.

While chapters two to four examine relative doses, chapter five assesses the accuracy of absolute dose (or *output*) calculations performed by the planning computers. Output variation with SSD and field size was examined. Two further situations already assessed for the distribution of relative dose were also considered: an obliquely incident field, and a field incident on an irregular surface.

The accuracy of calculations was assessed against criteria stipulated by the International Commission on Radiation Units and Measurement (ICRU). These set upper limits on the error in calculated dose of 2% (or 2 mm in the position of a given dose).

Using these criteria, the 2D dose distributions examined in chapter two were calculated with acceptable accuracy in most situations. The most notable exception was a 10% overestimation in dose made by both planning computers for points downstream of the small air cavity. This was caused by the assumption of an infinite lateral extent to the air cavity made while assessing dose to points immediately beneath the cavity.

The calculated position of the 90% isodose line in relation to field defining apertures (considered in chapter three) proved accurate in all circumstances. As a

result, it has been proposed that the TMS planning system produce a library of dose distributions relating to the set of standard elliptical apertures used in breast boost radiotherapy at the Beatson Oncology Centre.

Beam penumbra at extended SSD was modelled accurately by the planning computers at SSD values up to and including 110 cm. At higher SSDs, the position of the centre of the penumbra was modelled successfully, but unacceptable errors in the penumbra width occurred. Adjacent photon and electron fields were found to produce minimum dose inhomogeneity in the junction region if fields were positioned with a gap between the geometric field edges (as defined by the light field). The gap varied within a range of 1 – 4 mm, dependent on electron energy and SSD.

The calculation of absolute dose, assessed in chapter five, achieved less accuracy than the relative dose calculations considered previously. Errors in excess of 2% in the calculations of both planning systems were often found for extended SSD fields. At the standard SSD, TMS produced large errors (up to 8%) in output for field sizes less than 5 cm square. The assessment revealed fundamental flaws in the algorithms employed by both planning systems in the calculation of monitor units. Neither manufacturer has made a commitment to remedy these problems in the immediate future.

In conclusion, the Varian Cadplan and Helax TMS treatment planning systems produce acceptable accuracy in the calculation of relative dose from therapeutic electron beams in most commonly encountered situations. When interpreting clinical dose distributions, however, knowledge of the limitations of the calculation algorithm employed by each system is required in order to identify the minority of situations where results are not accurate. The calculation of absolute dose is too inaccurate to implement in a clinical environment.

CONTENTS

| | |
|-----------------------|------|
| Title | i |
| Abstract | ii |
| Contents | v |
| List of illustrations | ix |
| List of tables | xi |
| Author's note | xii |
| Acknowledgements | xiii |

Chapter 1: INTRODUCTION

| | | |
|-----|---|---|
| 1.1 | The clinical use of electron beams | 1 |
| 1.2 | Theoretical models of clinical electron beams | 2 |
| 1.3 | Pencil beam algorithms | 2 |
| 1.4 | Published assessments of pencil beam algorithms | 3 |
| 1.5 | Assessments performed in this work | 4 |

Chapter 2: PLANAR ISODOSE DISTRIBUTIONS IN A SOLID WATER PHANTOM

| | | |
|-------|---|----|
| 2.1 | Introduction | |
| 2.1.1 | Electron transport in tissue-equivalent materials | 7 |
| 2.1.2 | Current scatter algorithms | 8 |
| 2.2 | Materials and Methods | |
| 2.2.1 | Thermoluminescent dosimeters | 9 |
| 2.2.2 | The phantom | 10 |
| 2.2.3 | Clinical beam experiments | 11 |
| 2.4 | Results | 13 |
| 2.5 | Discussion | |
| 2.5.1 | Measurement uncertainties | 25 |
| 2.5.2 | Calculation uncertainties | 28 |
| 2.5.3 | Measured and calculated central axis depth doses | 28 |
| 2.5.4 | Oblique incidence | 29 |
| 2.5.5 | Bolus edge phantoms | 30 |

CONTENTS (continued)

| | | |
|-------------------|---|----|
| 2.5.6 | Cylindrical air cavity | 31 |
| 2.5.7 | Performance of the TMS and Cadplan scatter algorithms | 32 |
| Appendix A2.1 | Calibration of thermoluminescent dosimeters (TLDs) | 34 |
| Appendix A2.2 | Flow diagram of Microsoft Excel Visual Basic routine used for conversion of TLD point doses to isodose lines. | 36 |
| | | |
| Chapter 3: | BEAM PENUMBRA AT EXTENDED FSD | |
| 3.1 | Introduction | 38 |
| 3.2 | Materials and Methods | |
| 3.2.1 | Electron beam set-ups | 39 |
| 3.2.2 | Measurement apparatus | 39 |
| 3.2.3 | Diode measurements | 41 |
| 3.2.4 | Abutting photon and electron fields | 42 |
| 3.3 | Results | 44 |
| 3.4 | Discussion | |
| 3.4.1 | Uncertainties in measured and calculated doses | 53 |
| 3.4.2 | Calculation algorithms | 54 |
| 3.4.3 | Comparison of measured and calculated doses | 55 |
| 3.4.4 | Target Coverage Factors (TCFs) | 57 |
| 3.4.5 | Abutting photon and electron fields | 59 |
| Appendix A3.1 | Dose response characteristics of measurement diode | 61 |
| | | |
| Chapter 4: | BEAM PROFILES WITH OSTALLOY CUTOUTS | |
| 4.1 | Introduction | 62 |
| 4.2 | Materials and Methods | |
| 4.2.1 | Field set-up | 64 |
| 4.2.2 | Corrections to the measurements | 65 |

CONTENTS (continued)

| | | |
|--|--|-----|
| 4.3 | Results | |
| 4.3.1 | The 10 cm x 10 cm cutout | 66 |
| 4.3.2 | Non-linear film response | 68 |
| 4.3.3 | Breast boost cutouts | 71 |
| 4.4 | Discussion | |
| 4.4.1 | The effect of bremsstrahlung on film response | 75 |
| 4.4.2 | Measurement and calculation uncertainties | 76 |
| 4.4.3 | Discrepancies between the measured and calculated data | 77 |
| Appendix A4.1 | Dose response of the measurement film | 80 |
| Chapter 5: CALCULATION OF ABSOLUTE DOSE | | |
| 5.1 | Introduction | 81 |
| 5.2 | Materials and Methods | |
| 5.2.1 | Field set-up and phantom geometry | 82 |
| 5.2.2 | Measurement devices | 85 |
| 5.3 | Results | |
| 5.3.1 | Experiment 1. Variation of output with SSD | 87 |
| 5.3.2 | Experiment 2. Variation of output with field size | 95 |
| 5.3.3 | Experiments 3 and 4. Oblique incidence and bolus fields | 95 |
| 5.4 | Discussion | |
| 5.4.1 | Measurement and calculation uncertainties | 96 |
| 5.4.2 | Experiment 1. Variation of output with SSD | 97 |
| 5.4.3 | Experiment 2. Variation of output with field size | 100 |
| 5.4.4 | Experiments 3 and 4. Oblique incidence and bolus fields | 101 |
| Appendix A5.1 | Conversion from ionisation to absorbed dose with Roos 34001 chamber | 103 |
| Chapter 6: CONCLUSIONS | | |
| | | 104 |

CONTENTS (continued)

| | |
|-------------|-----|
| Future work | 107 |
| References | 109 |

LIST OF ILLUSTRATIONS

| | | |
|-----------|---|----|
| 2.1 | Phantom cross-sections for experiments in table 2.1. | 13 |
| 2.2 - 2.4 | Depth ionisation and thermoluminescence for beam energies 6 – 16 MeV. | 15 |
| 2.5 – 2.7 | Comparison of measured and calculated %CADD for beam energies 6 - 16 MeV. | 16 |
| 2.8 | Oblique incidence: comparison of measured and TMS isodose distributions. | 17 |
| 2.9 | Oblique incidence: comparison of measured and Cadplan isodose distributions. | 18 |
| 2.10 | Square bolus: comparison of measured and TMS isodose distributions. | 19 |
| 2.11 | Square bolus: comparison of measured and Cadplan isodose distributions. | 20 |
| 2.12 | Tapered bolus: comparison of measured and TMS isodose distributions. | 21 |
| 2.13 | Tapered bolus: comparison of measured and Cadplan isodose distributions. | 22 |
| 2.14 | Small air cavity: comparison of measured and TMS isodose distributions. | 23 |
| 2.15 | Small air cavity: comparison of measured and Cadplan isodose distributions. | 24 |
| 2.16 | Comparison of measured and calculated hot spot dose behind bolus edges. | 25 |
| A2.1 | Distribution of TLD sensitivities. | 34 |
| 3.1 | Arrangement of water phantom and diode for profile measurements. | 40 |
| 3.2 | Field edge positions for abutting fields. | 43 |
| 3.3 - 3.7 | Measured and calculated dose profiles at extended SSD for a 10 x 10 cm field. | 45 |
| 3.8 | Target Coverage Factors. | 50 |

LIST OF ILLUSTRATIONS (continued)

| | | |
|----------|---|----|
| 3.9 | Dose profiles across the junction of abutting photon and electron fields. | 51 |
| A3.1 | Dose response of diode detector. | 61 |
| 4.1 | Comparison of calculated and measured doses for a 10 x 10 cm square aperture. | 69 |
| 4.2 | Measured and calculated penumbra widths for a 10 x 10 cm square cutout. | 70 |
| 4.3 | Ratio of optical density in the penumbra to the central axis for a 10 x 10 cm aperture. | 70 |
| 4.4 | Film exposures of breast boost cutout 4. | 72 |
| 4.5 | Axes for optical density measurements on breast boost treatment apertures. | 73 |
| 4.6 | Measured and calculated doses for breast boost cutout 4. | 74 |
| A4.1 | Variation of optical density with applied monitor units for measurement film. | 80 |
| 5.1, 5.2 | Variation of measured and calculated output with SSD for a 10 x 10 cm field. | 88 |
| 5.3, 5.4 | Variation of measured and calculated output with SSD for a 5 x 5 cm field. | 89 |
| 5.5 | Calculated and measured virtual SSDs for a 10 x 10 cm field. | 91 |
| 5.6 | Calculated and measured virtual SSDs for a 5 x 5 cm field. | 92 |
| 5.7, 5.8 | Variation of output with field size for 6 and 16 MeV electron fields. | 93 |
| 5.9 | Measured and calculated outputs: oblique field. | 94 |
| 5.10 | Measured and calculated outputs: tapered bolus. | 94 |

LIST OF TABLES

| | | |
|-----|--|----|
| 2.1 | Experiments comparing TLD measurements with calculations. | 12 |
| 3.1 | Optimum gaps for abutting photon and electron fields. | 52 |
| 4.1 | Diode measurements of 90% and 10% dose for a square aperture. | 67 |
| 4.2 | Comparison of film measurements and TMS calculation of 90% dose for a square cutout. | 67 |
| 4.3 | Comparison of film measurements and TMS calculation of 10% dose for a square cutout. | 68 |
| 5.1 | Summary of experiments comparing measured and calculated monitor units. | 85 |
| 5.2 | Discrepancies between calculated and measured output at 110 and 120 cm SSD. | 91 |

AUTHOR'S NOTE

Throughout the text, reference is made to the commercial organisation Helax AB, and its product, the TMS treatment planning system. The author would like to point out that, following a corporate merger in 1999, the name of this company changed to MDS Nordion AB, and that of the treatment planning system to Helax-TMS.

ACKNOWLEDGEMENTS

The author wishes to acknowledge the valuable advice given by the project supervisor, Dr R C Lawson. The generous support and encouragement given by Mr Fraser Brunton is also gratefully acknowledged.

Advice and assistance received from Dr G M Ford and Dr S G McNee were much appreciated.

CHAPTER 1

INTRODUCTION

1.1 The clinical use of electron beams

The benefits of high energy electrons for the treatment of cancer were first reported in 1952 [1]. In the following decades, electron therapy established itself as a valuable alternative treatment modality to the more common X-ray therapy. By 1990, the clinical benefits of electron treatments had been noted for a diverse range of treatment sites including nodal disease of the neck; skin carcinomas; the salivary gland; and low pelvic tumours [2-4]. The value of post-operative electron radiotherapy to the resection margins of the breast following lumpectomy was recognised internationally [5,6]. Treatments to the head and neck, breast and skin form the majority of electron treatments carried out in current clinical practice.

To be suitable for electron therapy, a treatment volume must be confined to within a few centimetres of the skin surface. If this condition is met, the characteristic electron depth dose profile, involving a region of uniform high dose at shallow depths followed by a rapid decline in dose, results in full dose delivery to the target, while sparing the underlying normal tissues. This is a crucial advantage, and is the main reason for persisting with electron therapy; in other respects electrons have many disadvantages. Most of these are related to the ease with which electrons scatter away from dense objects, and scatter into less dense objects. This can result in a very non-uniform distribution of absorbed dose, and makes the interaction of electrons with inhomogeneous absorbers (such as a patient) difficult to model theoretically.

The majority of electron treatments are given as a single field with normal incidence. The simplicity of this set-up, together with the difficulties in modelling electron behaviour, meant early electron treatments were prescribed with reference to a single central axis depth dose. Computer assisted calculations of dose distribution were seen as unnecessary and even undesirable. However, as the use of computers in treatment planning became widespread in the late 1960s and the

1970s, this situation began to change. As early as 1967 [7], it was recognised that, in treatments of the head and neck, for example, irregularities in the patient surface, or the presence of tissue inhomogeneities like the trachea, could result in non-uniform dose distributions, or the displacement of the high dose region to greater or lesser depth. Failure to account for these effects, by adopting too simplistic a planning approach, could have damaging consequences for treatments delivered in close proximity to critical structures such as spinal cord.

1.2 Theoretical models of clinical electron beams

In both the United States and Europe, efforts were made to address the inaccuracies in electron dose calculations by implementing computer algorithms based on the interpolation of measured data [7,8]. No attempt was made to model electron scatter in the patient explicitly; regions of high or low density were handled by applying an equivalent path length correction to dose in a “line of sight” downstream of the inhomogeneity. While this simplification was capable of producing treatment plans giving a general impression of dose distribution, accuracy could not be assured in situations involving irregular beam entry surfaces, oblique incidence, or tissue inhomogeneities.

To improve the accuracy of calculated electron dose distributions, it was realised that the basic transport processes undergone by electrons in a scattering medium would have to be considered explicitly. Two alternative descriptions of the transport processes have been developed. The first, due to Bethe *et al* [9], relies on a diffusion approximation of electron behaviour, while a later theory developed by Eyges [10] examines multiple scattering events. The importance of scattering theory in the modelling of clinical electron beams is discussed further in chapter two.

1.3 Pencil beam algorithms

By the 1980s, attempts to implement scattering theory in a practical way for clinical electron beams led to the development of the pencil beam algorithm [11].

In this system, the electron beam is modelled as a series of infinitesimally small beams which enter the patient in a grid pattern and spread out with depth in the absorber. This approach was similar to many already adopted for photon beam algorithms. The pattern of electron scatter away from a central axis predicted by both the diffusion and multiple scattering models was represented by a Gaussian function. The mathematical formalism behind the Gaussian spread technique for electron pencil beams was developed independently by Hogstrom *et al* in the United States [12], and by Brahme and his co-workers in Sweden [13.] Early implementations of the algorithm gave encouraging results in the modelling of clinical beams incident on irregular surfaces and inhomogeneous phantoms [14]. The pencil beam model subsequently gained widespread acceptance.

Pencil beam algorithms have undergone a series of refinements since their introduction. An important improvement was the replacement of the single Gaussian (or *Hogstrom*) model of radial spread with the summation of three Gaussian functions [15]. This latter approach makes a better assessment of the contribution to the spread of pencil beams made by secondary electrons, which are not included in the scattering theory of Eyges. It also contains a reduction factor to account for range straggling, a quantum mechanical phenomenon resulting in a reduced path length for electrons undergoing large angle scattering events. Both treatment planning systems considered in this work, Varian Cadplan and Helax TMS, use pencil beams based on the three Gaussian beam approach. There are differences, however, in the way each planning system implements the algorithm in the calculation of relative absorbed dose. These are discussed in chapter two.

1.4 Published assessments of pencil beam algorithms

There has been considerable effort made towards assessing the accuracy of modern pencil beam calculation algorithms. The majority of published work is directed towards photon calculations, but there has also been interest in assessing electron calculations. Evaluations of planning systems based on the Hogstrom algorithm have been reported by McShan *et al* [16], Cheng *et al* [17] and by Muller-Runkel and Sang-Hyun [18].

The only published assessment of the Helax TMS system is that due to Blomquist *et al* [19], who examined software version 2.10J in the calculation of relative electron dose for a variety of phantom geometries. Monitor unit calculations were not considered. In general, the TMS calculations were found to be within +/- 2% of measured values, and an improvement over those reported as resulting from the Hogstrom algorithm. Greater inaccuracies were reported in a number of specific instances. These included oblique incidence of the beam, where a 7 mm discrepancy in penumbra position was reported, and incidence on a phantom containing a small air space.

Published reports on the accuracy of the Cadplan algorithm are limited to the work of Samuelson *et al* [20]. This work reported on the accuracy of relative dose and monitor unit calculations produced by Cadplan version 2.62. As with TMS, the calculations were generally accurate to within +/- 2% in most situations.

Exceptions to this were, however, reported in situations involving the modelling of small air cavities, and for relative off-axis doses in large fields. Here, errors of up to 7% were attributed to limitations in the modelling of the electron scattering foil.

1.5 Assessments performed in this work

The test results presented in later chapters of this current work complement existing publications, and have the additional benefit of providing a direct comparison of the performance of the TMS and Cadplan calculation algorithms. The scarcity of published assessments of monitor unit calculations (particularly for TMS) is addressed in chapter five, which is devoted to this topic. Much of the motivation for some specific tests originated from an acute need for the evaluation of dose distributions resulting from clinical treatments performed at Glasgow's Beatson Oncology Centre (B.O.C.). This was particularly true of the evaluation of breast boost cutouts reported in chapter four. Here, the aim was to provide clinicians with information on the nature of the field penumbra near the edge of commonly used field defining devices. The investigation of electron / photon junctions in chapter three, and the experiments assessing the planning computers'

ability to predict relative dose in the vicinity of a bolus edge (described in chapter two) were also of immediate clinical relevance. The use of bolus to reduce dose to spinal cord, and the matching of electron and photon fields (ultimately for the same reason) are common in treatments of the head and neck in the B.O.C.

Chapter four, unlike the other chapters, considers only the TMS planning system. This is because, when this work was carried out, the facility for electron planning had yet to be commissioned on Cadplan. There would be limited benefit in extending the assessment to include Cadplan because the specific aim was to provide clinicians at the B.O.C. with information on the use of specially shaped field-defining cut-outs used in breast boost treatments. This was achieved satisfactorily with the aid of measurements made with radiographic film and calculations performed on the TMS system.

During the course of experimental work, both planning systems underwent a process of continuous development. Helax TMS graduated from version 2.9E to version 4.1A while Varian Cadplan developed from version 2.7.9 to version 3.1.1. These changes reflected improvements to the photon calculation algorithms and user interfaces only. The particular software version under examination is given for both systems in each chapter. Neither planning system underwent any significant changes to the electron dose calculation algorithm, nor have any changes been made since the work presented here was completed [21,22]. All comparisons of measured and calculated data can, therefore, be considered applicable to the current software versions. At the time of writing, these were TMS v5.0A and Cadplan v6.0.8.

A valid judgement on the success of calculations made by treatment planning computers requires the definition of acceptance criteria for their accuracy. The International Commission on Radiation Units and Measurements (ICRU) stipulated appropriate criteria in report number 42 (on the use of computers in radiotherapy) [23]. On the subject of quality assurance, the report states that a computed dose distribution may be considered accurate “if it differs from relative dose measurements by less than 2% (or 2 mm in the position of isodose lines in

special circumstances involving very steep dose gradients) in points of relevance to the treatment". These criteria have been used to assess the accuracy of dose calculation for the majority of this work. If other criteria are appropriate, these are justified in the context of the specific situation being examined.

CHAPTER 2

PLANAR ISODOSE DISTRIBUTIONS IN A SOLID WATER PHANTOM

2.1 Introduction

2.1.1 Electron transport in tissue-equivalent materials.

In many clinical situations therapeutic electron beams are used in combination with beam modifiers such as bolus, or encounter non-standard patient geometries including oblique incidence and/or the presence of air cavities. Accurate prediction of the dose distribution in these situations requires detailed modelling of electron transport processes, both within the patient and in any overlying bolus material. The theory underlying electron transport in solids was first described by Eyges and is known as the Fermi-Eyges small angle scattering theory [10]. In this theory, primary electrons are assumed to undergo two types of interaction with charged particles in the absorber. Firstly, inelastic collisions with atomic electrons; and secondly, elastic long range collisions with nuclei. It is assumed that these collisions result in only small angle deflections to the path of the primary electrons.

Eyges expressed the lateral displacement $G_{(x,z)}$ of a small electron beam as follows:

$$G_{(x,z)} = \frac{1}{\sqrt{2\pi\sigma_{x(z)}}} \exp\left(-\frac{x^2}{2\pi\sigma_{x(z)}^2}\right) \quad 2.1$$

Where $\sigma_{(x,z)}$ is a lateral spatial spread parameter dependent on the depth z and lateral displacement x in the absorber. In this context, a “small electron beam” is one whose initial diameter is small in comparison with the range of primary electrons in the absorber. The spread parameter determines the characteristic features of the electrons’ lateral spread. It was given by the expression

$$\sigma_{x(z)}^2 = \frac{1}{2} \int_0^z \frac{\theta^2}{\rho l} (z') \rho(z') (z - z')^2 dz' \quad 2.2$$

Where $\theta^2/\rho l$ is the mass angular scattering power and ρ is the physical density of the absorber.

Modern computer systems are capable of providing numerical solutions to the theory for clinical electron beams via Monte Carlo simulations [24-26]. The calculations, however, remain too time-consuming to be implemented in day-to-day clinical practice.

2.1.2 Current scatter algorithms

In the early 1980s considerable effort was made to apply scattering theory to the modelling of clinical beams in a practicable way. The first models to be introduced were based on pencil beam algorithms developed independently by Hogstrom *et al* [12] and Brahme *et al* [13]. Later, another algorithm was reported by Werner *et al* [27]. The term “pencil beam” refers to a mono-directional electron beam with a “small” diameter as defined above. After intersecting a patient or phantom surface, the beam spreads out with depth as electrons are scattered. The resulting distribution of energy deposition resembles the tip of an upturned pencil. Pencil beams originating from all parts of the phantom contribute to the dose at a given point at depth. These contributions are summed to yield the final dose.

The accuracy of pencil beam calculations depends crucially on the algorithm employed to model the spread of the pencil beam with depth. In order to save calculation time, electron scatter has not yet been modelled explicitly. Equations 2.1 and 2.2 are not implemented directly, but an approximation is used which, in the case of the Hogstrom algorithm, models the spread of electrons with a radially symmetric Gaussian function i.e. proportional to $\exp(-\theta^2/\sigma^2)$. This concept was developed further by Lax *et al* [15] who replaced the single Gaussian beam model with a summation of three Gaussians. This implementation makes a better assessment of the contributions made to the spread of pencil beams by large angle scattering and range straggling. Parameters for the Gaussian beams are derived from pre-calculated Monte Carlo kernels in homogeneous media and then scaled

for layered inhomogeneous media by the method described by Lax and Brahme [28]. It is this latter model on which both the TMS and Cadplan treatment planning systems base their electron dose calculations. The TMS algorithm was, however, supplied with updated Gaussian parameters following the work of Andreo and Ahnesjö in 1991 [29].

2.2 Materials and Methods

2.2.1 Thermoluminescent dosimeters

Dose calculations from the Helax TMS 4.1A and Varian Cadplan 2.7.9 planning computers were compared with measurements made by thermoluminescence dosimetry in a solid water phantom. The phantom is described below.

Thermoluminescent dosimeters (TLDs) were of the square chip variety with a flat surface area of width and length 3.0 mm and depth 0.9 mm (QADOS Ltd, Unit 9 Compton Place, Surrey Avenue, Camberely, Surrey GU15 3DX). They were made from a proprietary material, *LiF100*, which consists of lithium fluoride doped with a variety of impurities. Among the impurities, divalent positive ions residing in the interstitial lattice spaces are thought to play an important role in enhancing the thermoluminescence process [30]. Electrons ejected from the lattice by ionising radiation are trapped in metastable excited energy states provided by the impurities and, following promotion to a higher energy level by thermal lattice vibrations, drop to the ground state with the emission of photons in the visible spectrum. This final emission is proportional to the original ionising radiation incident on the material.

The suitability of lithium fluoride for reproducible and accurate thermoluminescence dosimetry has been previously noted by the ICRU [31]. TLDs have a large response per unit volume, enabling the use of small sizes for measurement. Since there are often steep absorbed dose gradients in clinical electron beams, the small size makes TLDs very useful. Prior to their use in the comparison experiments, the TLDs were assessed for sensitivity, and an individual calibration factor assigned to each. This process is described in detail in appendix

A2.1. The mean standard deviation in sensitivity for a series of measurements made with any individual TLD was calculated as 1.0%.

Mayles *et al* [32] conclude that the percentage standard error in any individual measurement of thermoluminescence can be found by the addition, in quadrature, of this standard deviation with a factor related to the number of repetitions made in the initial calibration measurements. As shown in appendix A2.1, the result of this addition is a standard error in thermoluminescence of +/- 1.1% for a single measurement. Estimates of relative absorbed dose result from taking the ratio of two thermoluminescence measurements: one at the location in question, the other at the normalisation point. The total standard error in relative absorbed dose may thus be estimated by adding the standard errors in each of these two measurements in quadrature. This gives a total uncertainty in measurements of relative absorbed dose of 2%. This is at the lower end of commonly quoted values for individually calibrated chips of LiF100, but is not without precedent in the literature [33].

2.2.2 The phantom

TLDs were situated in precisely milled cut-outs made in a slab of WTe solid water, an epoxy resin based water substitute (St Bartholomews Hospital, 2nd floor 80 Bartholomew Close, West Smithfield, London EC1A 7BE). Measurements were made in a phantom which consisted of separate sections of WTe, each with a square cross-section of 25 cm x 25 cm. Sections of various thickness were available which allowed the slab accommodating the TLDs to be placed at various depths. The thickness of each solid water section was measured with a micrometer and found to be within +/- 0.1 mm of the nominal thickness. By first measuring its weight with an electronic balance, the density of WTe was determined as 1.027 +/- 0.005 gcm⁻³. In accordance with IPEMB recommendations [34], a minimum of 10 cm backscatter material was employed throughout. Exposures were made with a Clinac 2100C linear accelerator (Varian Associates, Palo Alto, California, USA) at electron beam energies in the range 6 to 20 MeV.

Nisbet and Thwaites [35] reported that depth ionisation curves measured in WTe and in water are in agreement to within ± 0.5 mm for electron beams with incident energies in the range 5 to 17 MeV. Furthermore, the equivalence of depth ionisation measured with a p-type diode detector in water, and depth dose in water, has been noted by the ICRU [31]. A comparison showing the equivalence of depth ionisation in water to depth thermoluminescence in WTe would, therefore, confirm the equivalence of depth thermoluminescence in WTe to depth dose in water. To confirm this, central axis depth ionisation curves were obtained with a diode detector in a water phantom and compared to relative thermoluminescence readings obtained with TLDs at corresponding depths in WTe. Beam energies of 6, 12 and 16 MeV were considered at a field size of 10 cm x 10 cm and SSD of 100 cm. The diode detector used was a p-type device manufactured by Scanditronix (QADOS Ltd, address as above). The device was interfaced to a Therados DPD5 electrometer (Therados Instrument AB, Dalgatan 15, Uppsala, Sweden).

2.2.3 Clinical Beam Experiments

A series of five experiments comparing measured with calculated dose distributions were now performed. Table 2.1 contains a description of each experiment, whilst figure 2.1 shows the cross-sections of each phantom. The first experiment examined the planning computers' ability to predict central axis depth dose. Succeeding experiments were designed to test the ability of the planning computers to predict planar dose distributions resulting from beam set-ups encountered clinically. These are described below. Where possible, a beam energy of 12 MeV was employed since this is the most commonly encountered energy in treatments of the head and neck.

Oblique incidence: this is often inevitable in electron treatments of the head and neck. The experiment examined a 30° beam incident on a plane phantom. A SSD of 102 cm, rather than the standard treatment SSD of 100 cm, was required to prevent the treatment applicator colliding with the phantom.

Bolus Edges: the addition of wax bolus over a portion of the treatment area is commonly used to limit dose to underlying structures such as spinal cord. A typical bolus depth of 2.0 cm was used. To illustrate the importance of the bolus geometry, both squared-off (90°) and smoothed (45°) edges were considered. Polymethylmethacrylate (PMMA) was used as the bolus material to provide a more precise and reproducible shape than that possible with wax (which is used clinically). The geometry was two-dimensional i.e. the bolus extended beyond the field edges in the direction normal to the measurement plane. The beam was incident normally on the phantom.

Trachea: irradiation of the neck is occasionally given at a sufficiently anterior angle of incidence, or with sufficiently energetic electrons, that the presence of the trachea cannot be ignored when assessing the resulting dose distribution. To simulate the trachea, a 1.5 cm diameter hollow cylinder was machined along the length of a solid water section at a depth (to the cylinder centre) of 4.0 cm. This experimental geometry was, therefore, also two-dimensional. A beam energy of 20 MeV was used so that the air space fell within the high dose region of the depth dose curve. This situation ensures that perturbations in dose caused by the air space will not be swamped by the steep dose gradient of the fall-off region. The beam is incident normally on the phantom.

| Experiment | SSD (cm) | Energy (MeV) | Field Size (cm) | Measurement dimension | | | Measurement Technique |
|--------------------------------|-------------|-----------------|--------------------|-----------------------|---|-----|--------------------------|
| | | | | X | Y | Z | |
| 1. Central axis depth dose. | 100 | 6,12,16 | 10 x 10 | 0 | 0 | Var | Diode |
| 2. Oblique incidence. | 102 | 12 | 10 x 10 | Var | 0 | Var | TLD |
| 3. 90° Bolus edge. | 100 | 12 | 19 x 19 | Var | 0 | Var | TLD |
| 4. 45° bolus edge. | 100 | 12 | 19 x 19 | Var | 0 | Var | TLD |
| 5. Trachea. | 100 | 20 | 15 x 15 | Var | 0 | Var | TLD |

Table 2.1. Summary of experiments performed to compare TLD measurements with planning computer calculations. *Var* indicates that the measurements were carried out at various points. X and Y refer to the photon collimator X and Y axis directions. The Z dimension runs parallel to the beam central axis and so indicates depth below the phantom surface.

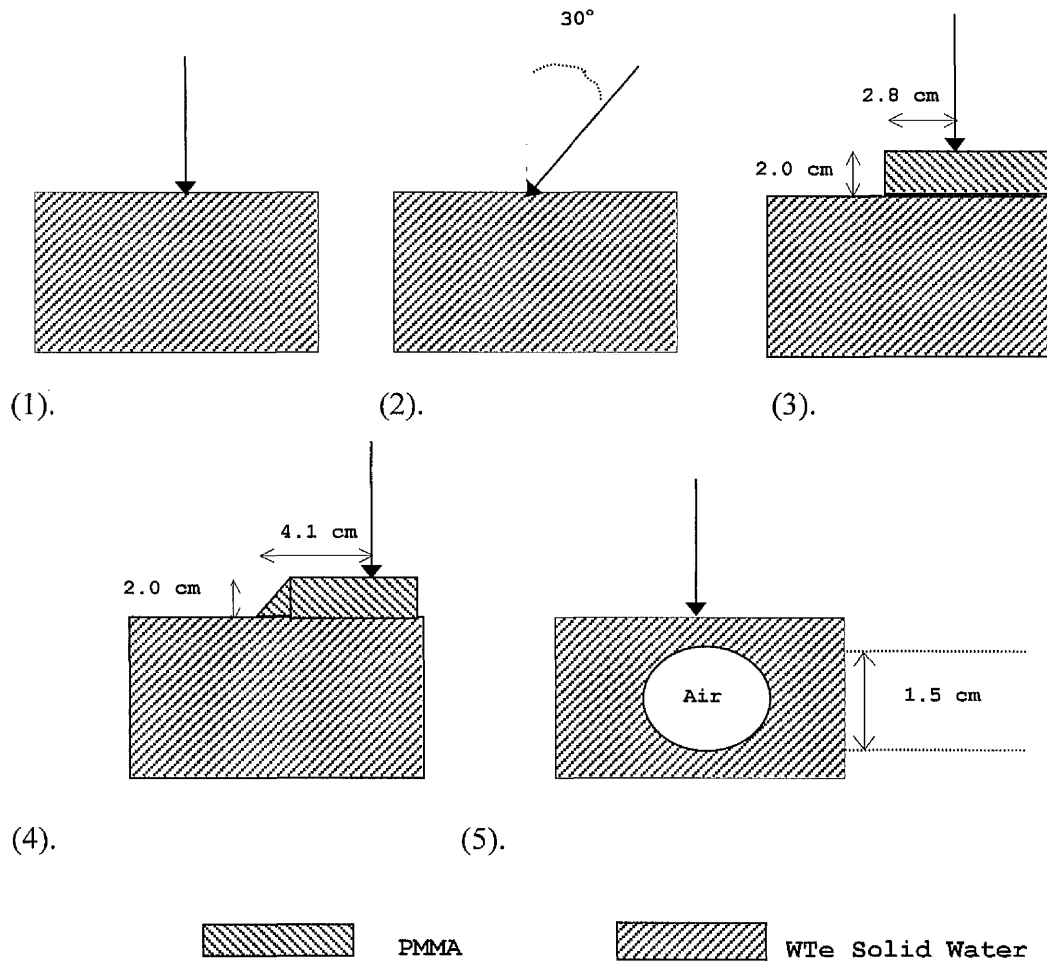


Figure 2.1. Phantom cross-sections used for experiments listed in table 2.1. Single arrows represent the electron beam central axis. (1) Normal incidence. (2) Oblique incidence of 30° . (3) 90° bolus edge. (4) 45° bolus edge. (5) Cylindrical air cavity of 1.5cm diameter.

2.4 Results

Figures 2.2 – 2.4 show depth ionisation curves measured with a diode in a water phantom together with the corresponding depth thermoluminescence curves recorded with TLDs in solid water. Curves are individually normalised to the depth of maximum dose (D_{\max}). As discussed above, the ICRU have established that depth ionisation in water measured by a p-type diode detector is equivalent to relative absorbed dose over the range of electron beam energies considered in this work. The depth ionisation curves shown in figures 2-4 may thus be regarded as a description of the variation of absorbed dose with depth in water.

Central axis depth dose. Diode measurements of central axis depth dose are compared with calculated values from the planning computers in figures 2.5-2.7. Curves are individually normalised to D_{\max} .

Clinical beam experiments. Measured and calculated two-dimensional dose distributions resulting from an obliquely incident beam and beams incident on phantoms containing bolus and air spaces are shown in figures 2.8 – 2.15. TLD measurements were made at a series of discrete points forming a two-dimensional grid in the X-Z plane. This data was processed using a software algorithm developed specifically for the purpose using the Visual Basic programming language running under Microsoft Excel 97. On execution of the program, the discrete measurements are transformed to the equivalent isodose distribution. The algorithm used is presented as a flow diagram in appendix A2.2. Output from the program allows measured data to be compared directly with isodose distributions produced by the planning computers. In all cases, dotted lines represent measured data whilst solid lines represent calculated data. Lateral position “0” represents the beam central axis entry point in the collimator x direction.

The diode measurements shown in figures 2.2 – 2.4 show that the D_{\max} depth for 12 MeV electrons is approximately 2.7 cm and that for 20 MeV electrons is approximately 1.7 cm. Consequently, the normalisation point for the obliquely incident field was set at an oblique depth of 2.7 cm along the beam central axis, and at a vertical depth of 1.7 cm for the trachea experiment. In both cases the measured and calculated data have the same normalisation point. For the bolus edge experiments, the D_{\max} depth on the central axis lies in a region of rapidly changing dose, making it unsuitable as a normalisation point. Dose distributions were, therefore, normalised at a distance of approximately 7 cm from the beam central axis and depth equal to the D_{\max} depth. The bolus edge phantoms produced scatter effects which lead to doses in excess of 120%, localised in small areas. For clarity, the maximum isodose displayed is 110%. The values of hot spots are shown separately in figure 2.16.

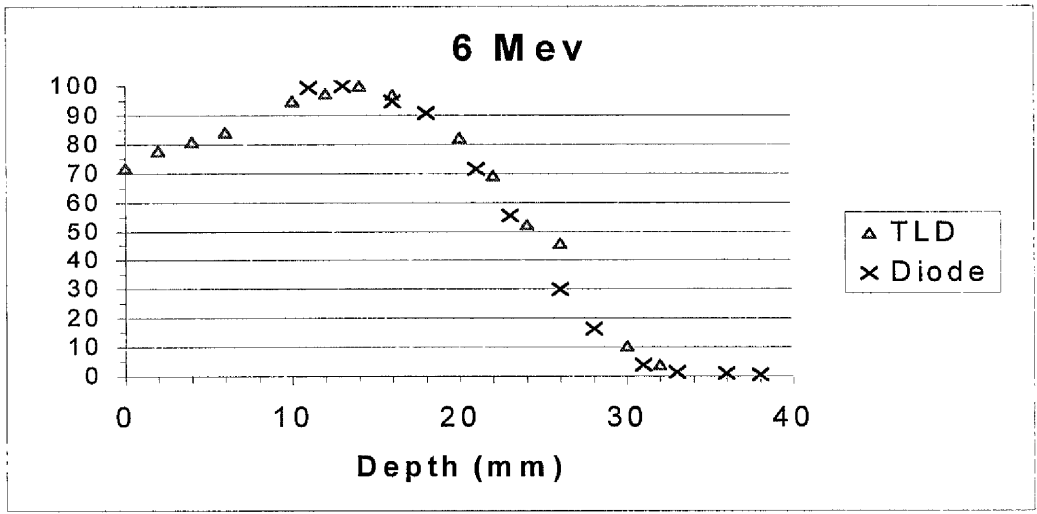


Figure 2.2. Relative depth ionisation in water (measured by diode), and depth thermoluminescence in WTe solid water for a 6 MeV electron beam.

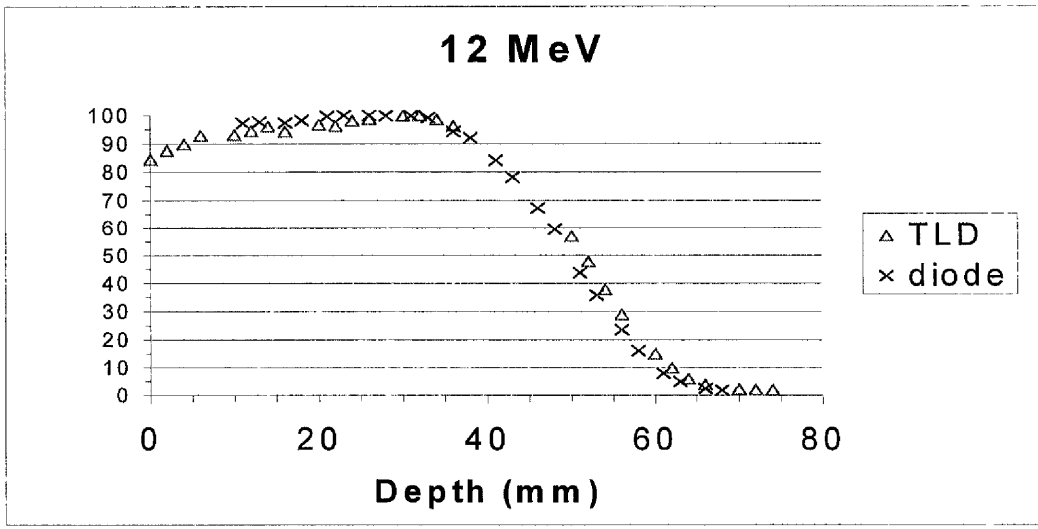


Figure 2.3. Relative depth ionisation in water (measured by diode), and depth thermoluminescence in WTe solid water for a 12 MeV electron beam.

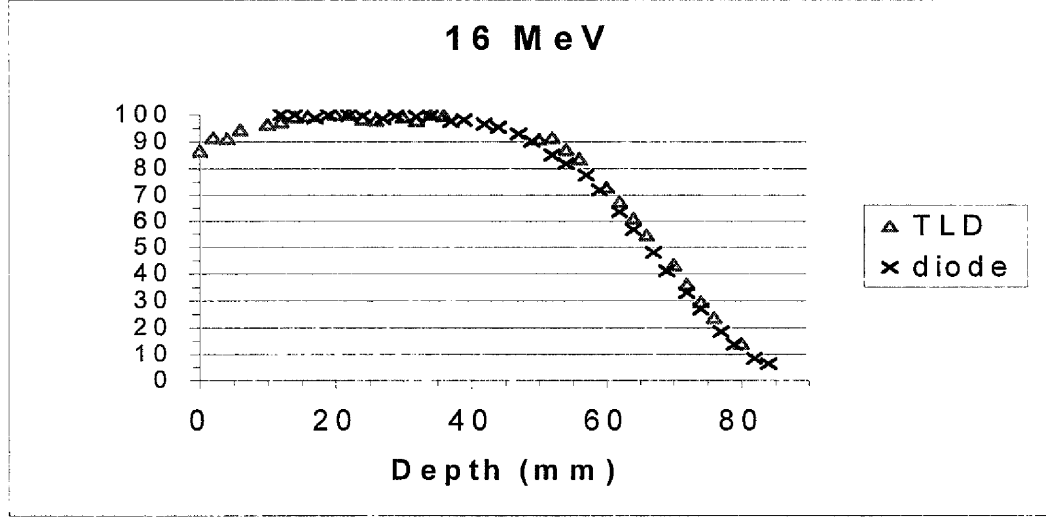


Figure 2.4. Relative depth ionisation in water (measured by diode), and depth thermoluminescence in WTe solid water for a 16 MeV electron beam.

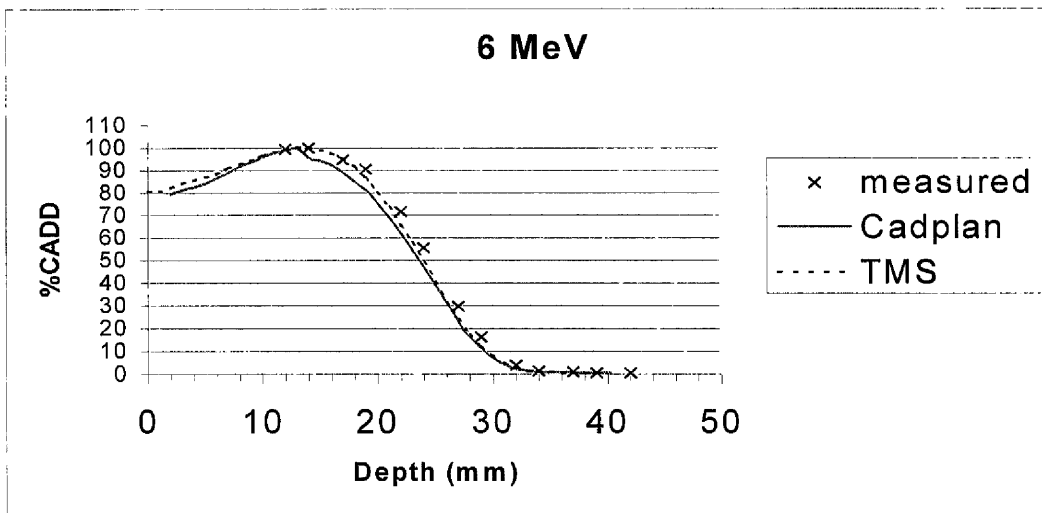


Figure 2.5. Comparison of measured and calculated %Central Axis Depth Dose (%CADD) for a 6 MeV, 10x10 field. Measurements made with a diode in water, calculations from Helax TMS and Varian Cadplan.

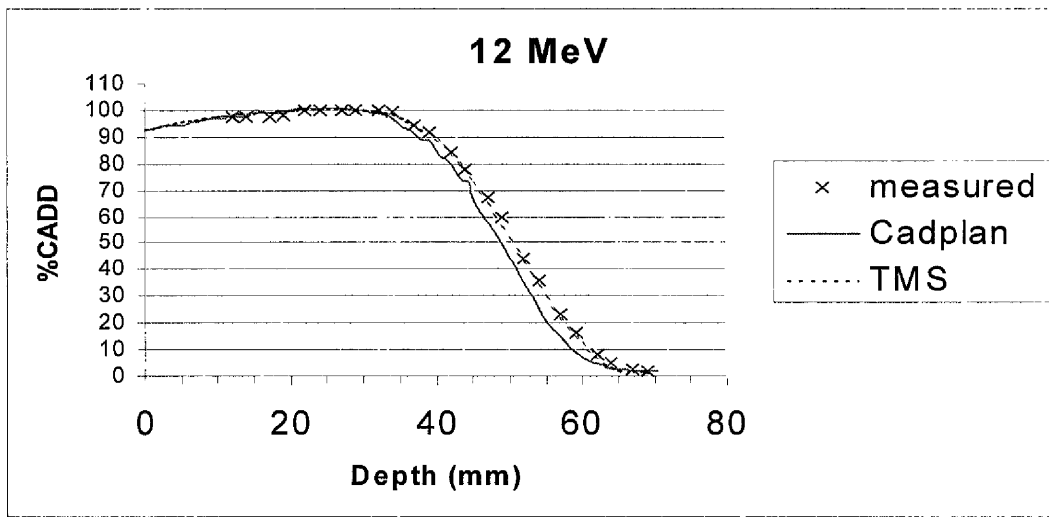


Figure 2.6. Comparison of measured and calculated %Central Axis Depth Dose (%CADD) for a 12 MeV, 10x10 field. Measurements made with a diode in water, calculations from Helax TMS and Varian Cadplan.

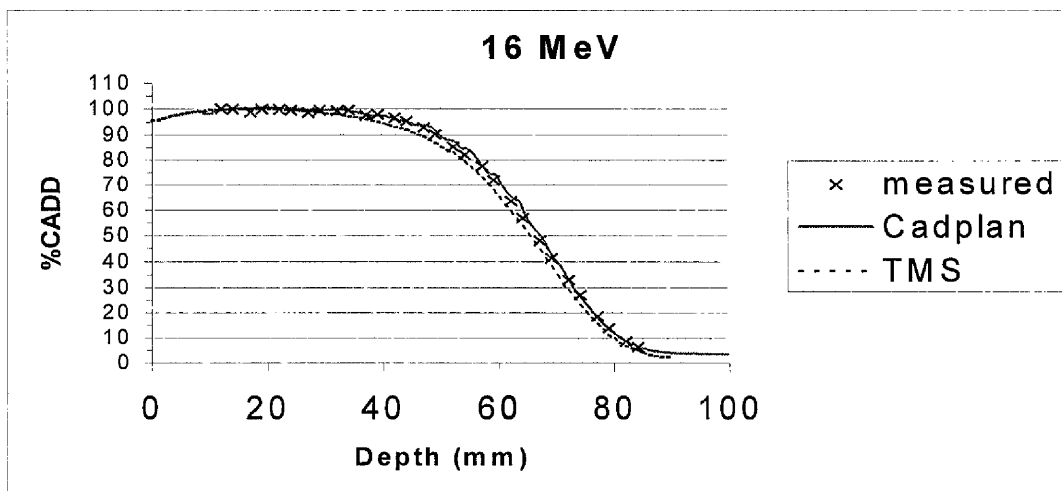


Figure 2.7. Comparison of measured and calculated %Central Axis Depth Dose (%CADD) for a 16 MeV, 10x10 field. Measurements made with a diode in water, calculations from Helax TMS and Varian Cadplan.

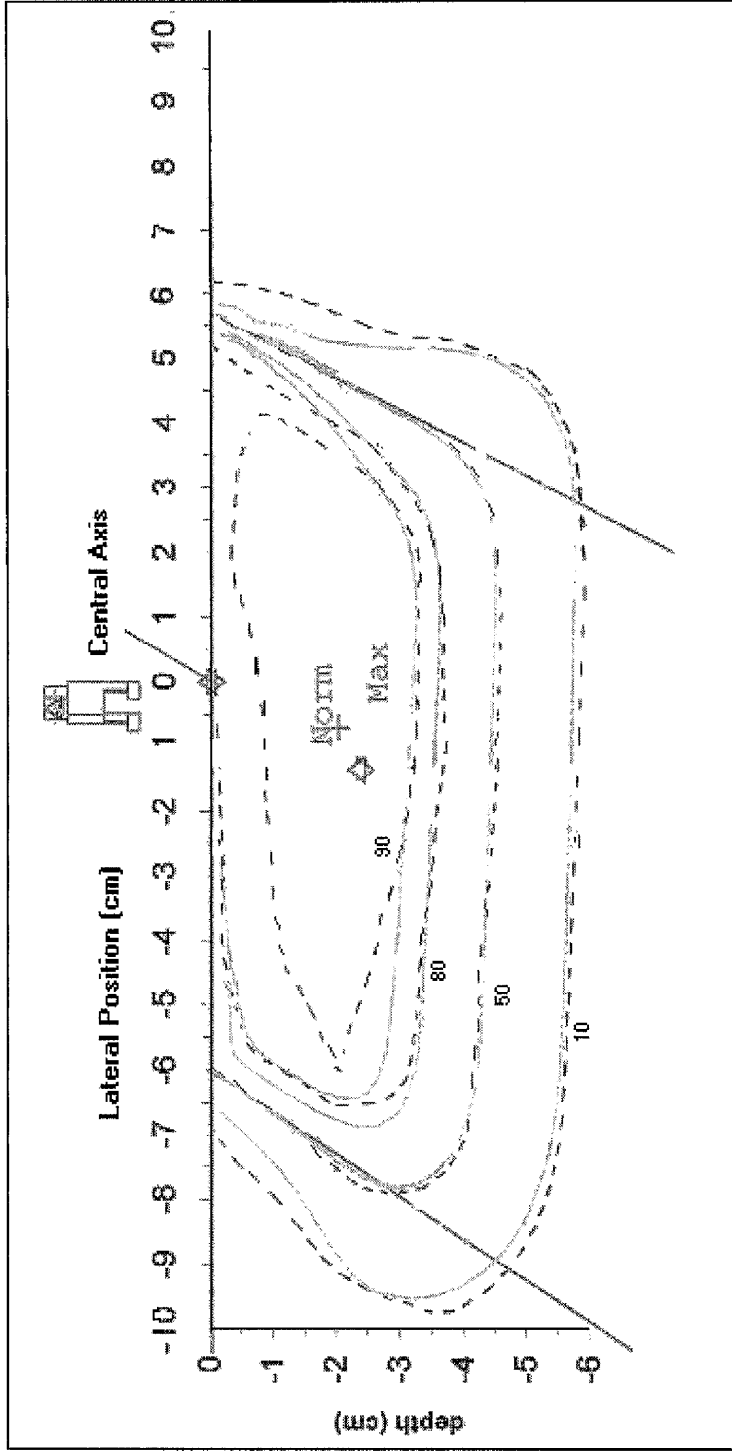


Figure 2.8. Comparison of measured and calculated doses for a 12 MeV, 10 x 10 cm electron beam incident at an angle of 30 degrees to the vertical. Dotted lines represent TLD measurements made in WTe solid water, solid lines represent the Helax TMS calculation. Field direction indicators, "Norm" and "max" points are features of the TMS isodose plot.

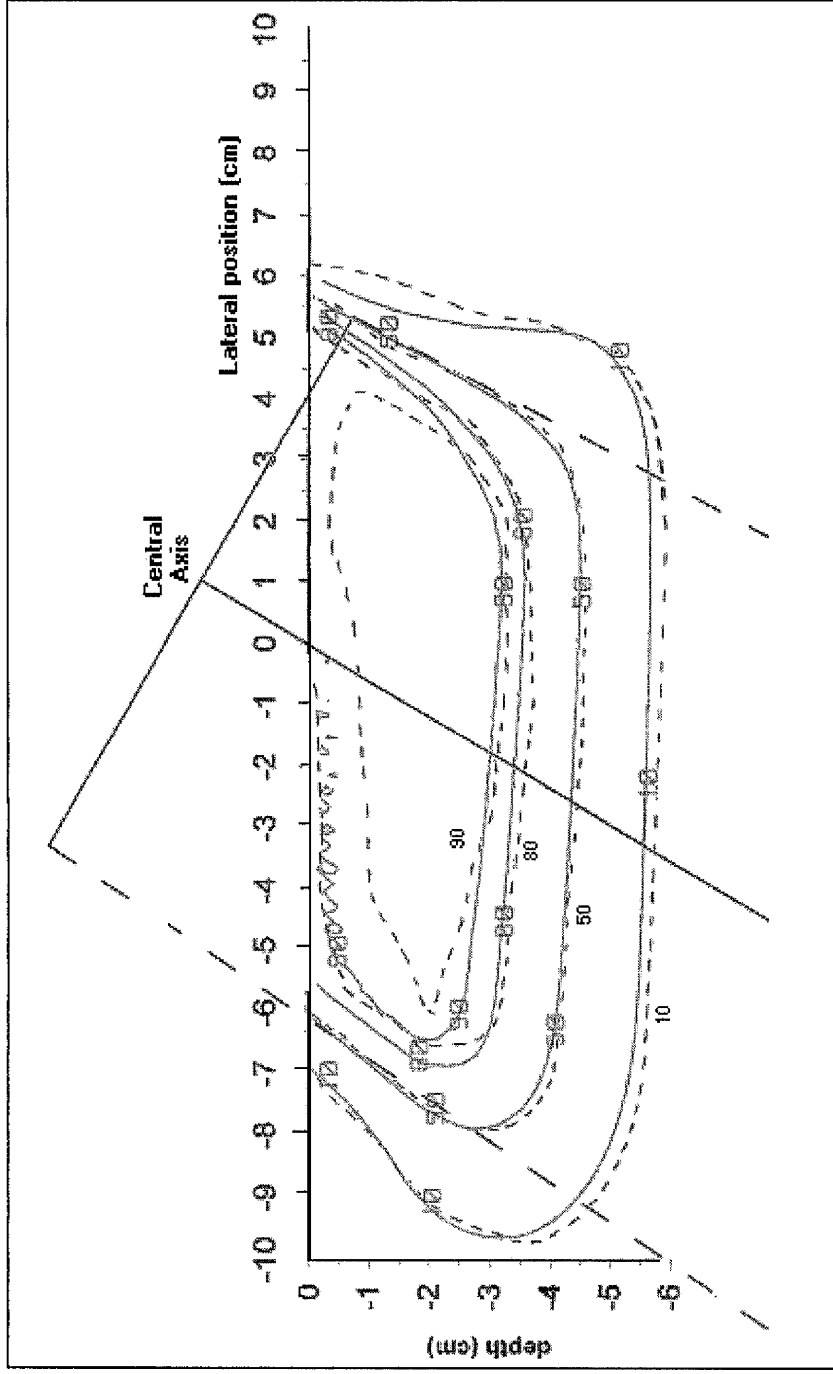


Figure 2.9. Comparison of measured and calculated doses for a 12 MeV, 10 x 10 cm electron beam incident at an angle of 30 degrees to the vertical. Dotted lines represent TLD measurements made in WTe solid water, solid lines represent the Varian Cadplan calculation. Field edges and central axis from the Cadplan plot are reproduced.

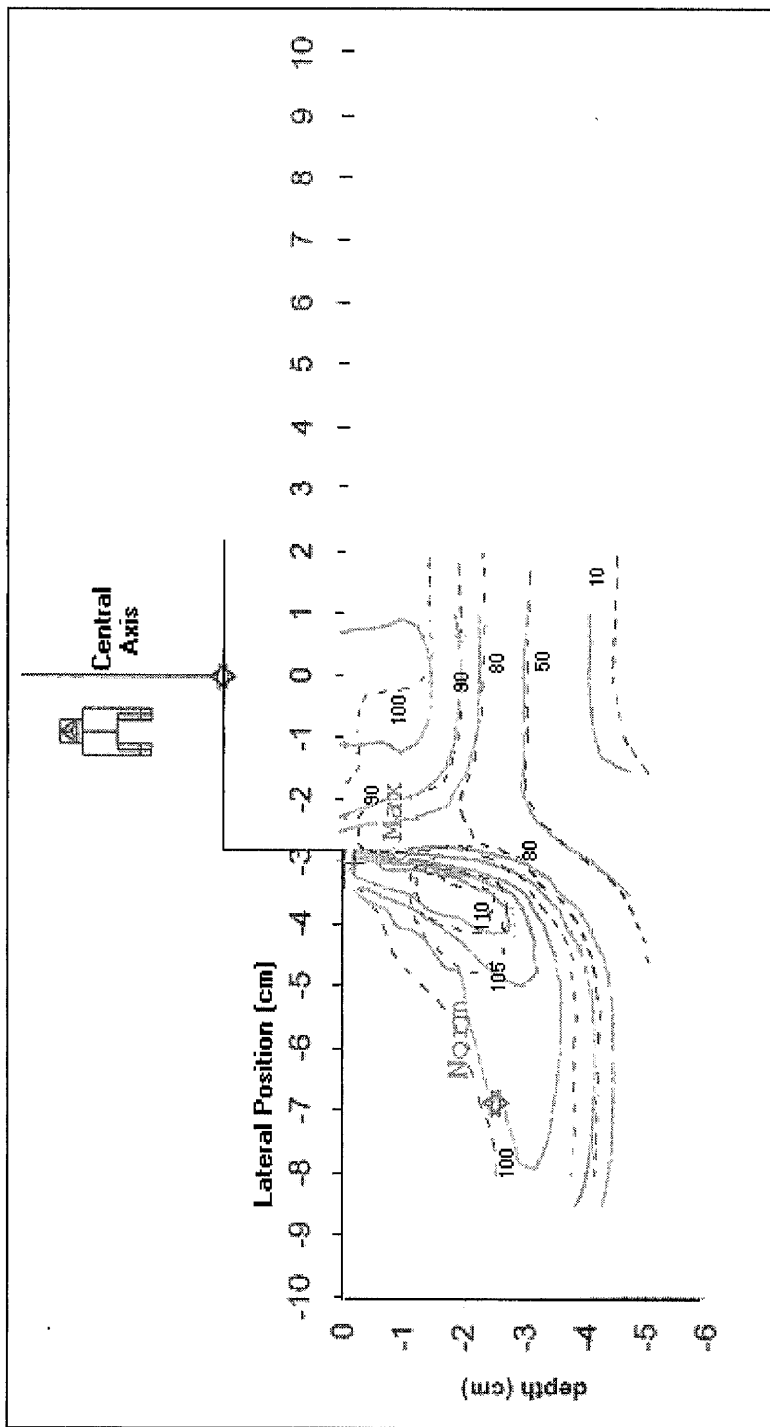


Figure 2.10. Comparison of measured and calculated doses for a 12 MeV, 19 x 19 cm electron beam incident on WTe solid water overlaid with a squared-off PMMA block. Dotted lines represent TLD measurements made in WTe solid water, solid lines represent the Helax-TMS calculation. Field direction indicators, "Norm" and "Max" points are features of the TMS isodose plot.

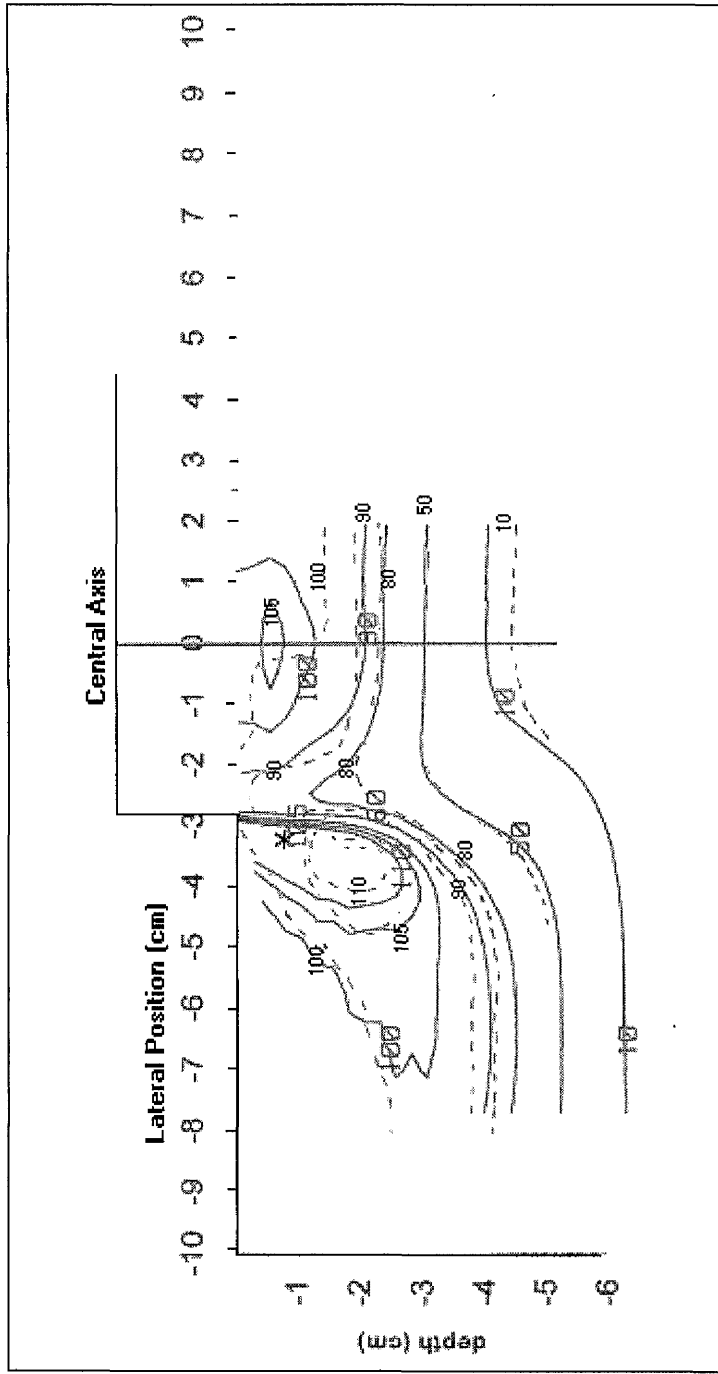


Figure 2.11. Comparison of measured and calculated doses for a 12 MeV, 19 x 19 cm electron beam incident on WTe solid water overlaid with a squared-off PMMA block. Dotted lines represent TLD measurements made in WTe solid water, solid lines represent the Caplan calculation.

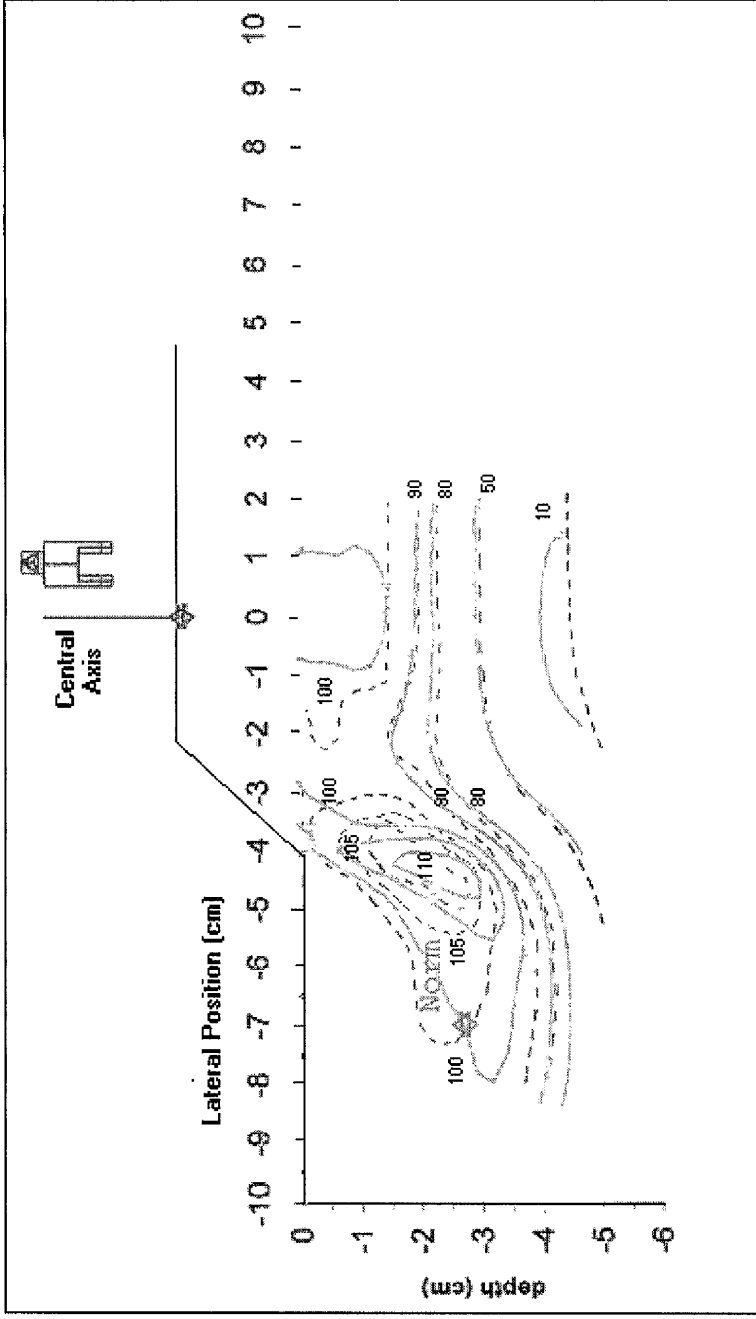


Figure 2.12. Comparison of measured and calculated doses for a 12 MeV, 19 x 19 cm electron beam incident on WTe solid water overlaid with a tapered PMMA block. Dotted lines represent TLD measurements made in WTe solid water, solid lines represent the Helax-TMS calculation. Field direction indicators, "Norm" and "Max" points are features of the TMS isodose plot.

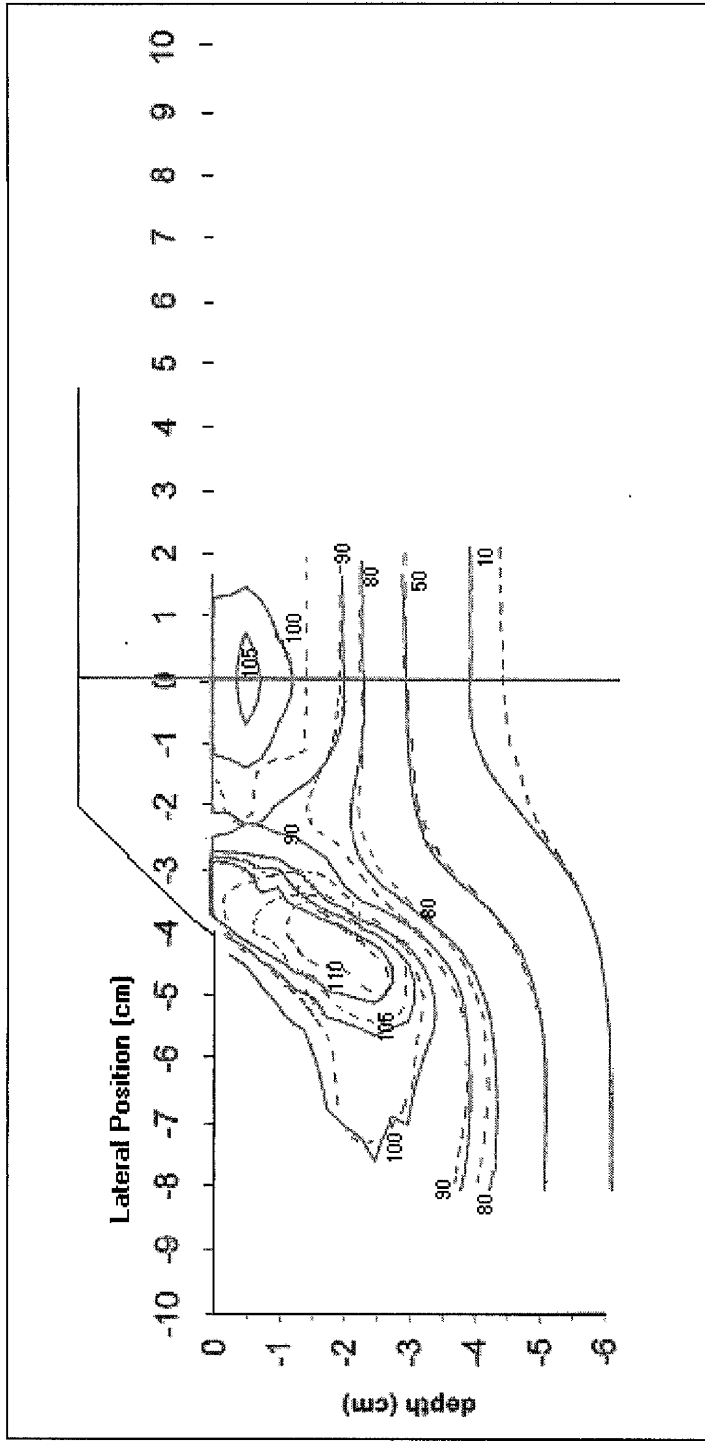


Figure 2.13. Comparison of measured and calculated doses for a 12 MeV, 19 x 19 cm electron beam incident on WTe solid water overlaid with a tapered PMMA block. Dotted lines represent TLD measurements made in WTe solid water, solid lines represent the Caplan calculation.

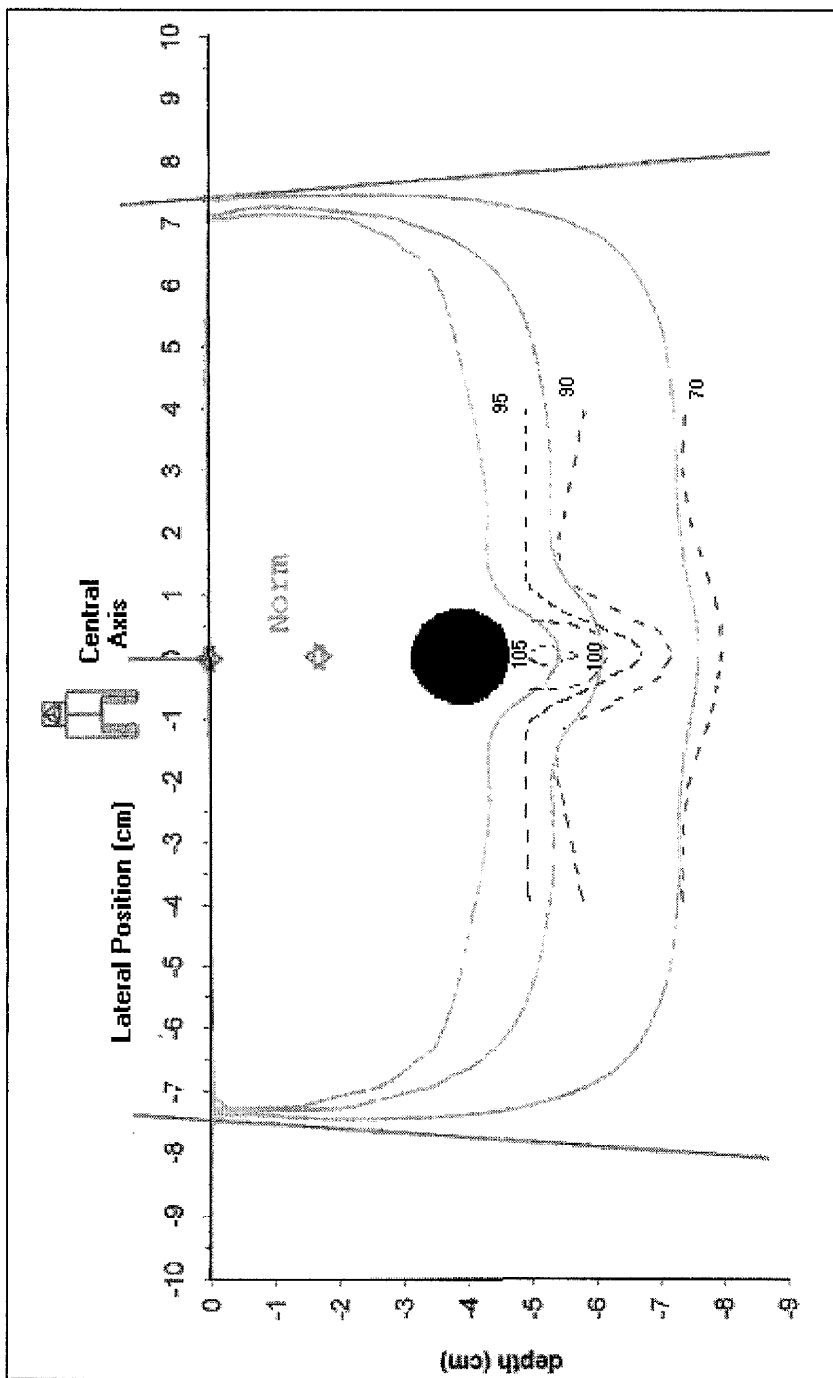


Figure 2.14. Comparison of measured and calculated doses for a 20 MeV, 15 x 15 cm electron beam incident on a WTe solid water phantom containing a 1.5 cm diameter air space (shown in black). Dotted lines represent TLD measurements (curtailed 4 cm downstream of the air space); solid lines represent the Helax-TMS calculation. Field direction indicators and "Norm" point are features of the TMS isodose plot. 100% and 105% isodose lines are present for the measured data only.

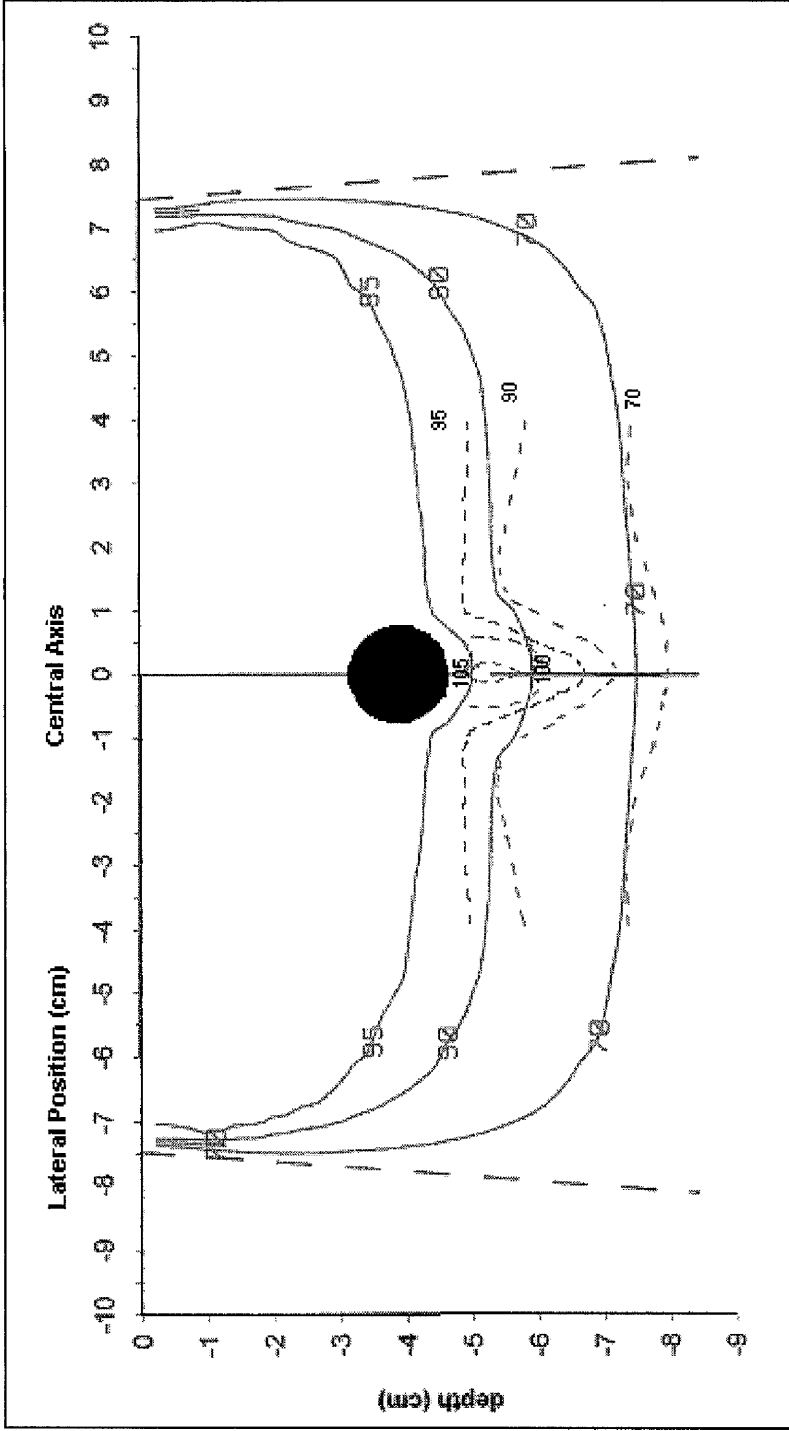


Figure 2.15. Comparison of measured and calculated doses for a 20 MeV, 15 x 15 cm electron beam incident on a WTe solid water phantom containing a 1.5 cm diameter air space (shown in black). Dotted lines represent TLD measurements (curtailed 4 cm downstream of the air space); solid lines represent the Cadplan calculation. The beam central axis and field edges from the Cadplan isodose plot are reproduced. 100% and 105% isodose lines are present for the measured data only.

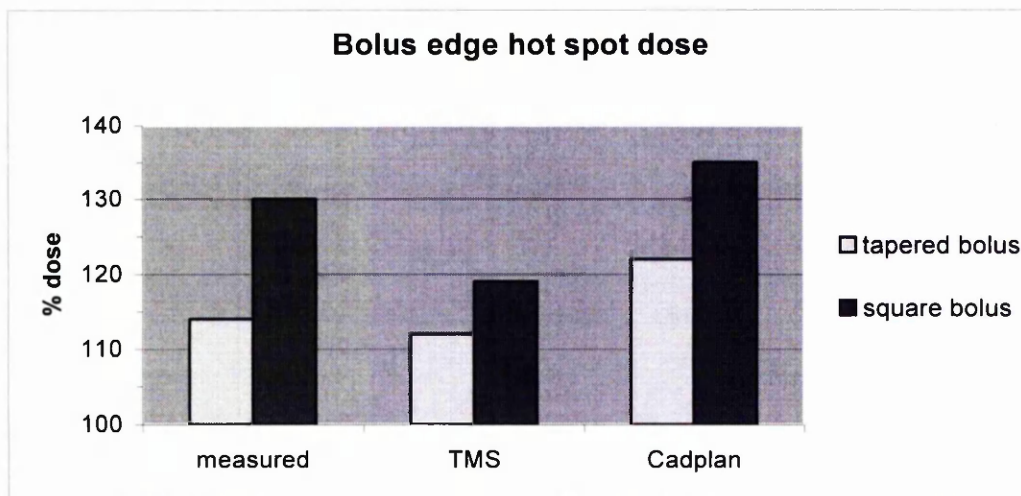


Figure 2.16. Comparison of measured and calculated doses for the hot spot behind a 45° tapered bolus edge and a 90° square bolus edge, for a 12MeV electron beam. Measurements made by TLD in WTe solid water, calculations by planning computers.

2.5 Discussion

The objective of this work was to assess the ability of two treatment planning systems, Helax TMS 4.1A and Varian Cadplan 2.7.9, to calculate electron depth dose distributions accurately. In an attempt to reproduce the variety of conditions encountered clinically, both simple and complex phantoms have been used in a comparison of measured and calculated relative depth dose. The clinical situations considered were: oblique incidence; incidence near a bolus edge, and incidence on an area overlaying the trachea. Measurements were made with a diode in a water phantom and by thermoluminescence dosimetry in a WTe solid water phantom.

2.5.1 Measurement uncertainties

There are no formal protocols describing the use of TLDs in the measurement of electron depth dose. Before any conclusions can be drawn from its use, it is therefore, important to compare relative absorbed dose measured in this way with a method traceable to national standards. Currently, the national standard directs that depth ionisation measured with a designated ion chamber in a water phantom

is converted to absorbed dose by applying a series of environmental and chamber-related correction factors and an air kerma calibration [34]. As was noted in the results section, the ICRU have noted that depth ionisation measurements made with a diode in a water phantom can be regarded as being indicative of relative absorbed depth dose without the need for correction [31]. Diode measurements are thus indirectly traceable to national dosimetric standards. For simplicity therefore, the accuracy of TLD measurements was assessed by comparison with relative depth ionisation measured by a diode in a water phantom.

Both diode and TLD measurements were subject to some uncertainty in precision and accuracy. The diode could be positioned with an estimated uncertainty of ± 0.25 mm. The precision in measuring the position at which a certain dose occurs was thus no better than ± 0.25 mm. In regions of high dose gradient the precision with which doses can be measured with a diode also depends on the *accuracy* of measurement (this will be discussed in chapter 3). This depends crucially on the size of the active volume over which the changing dose is averaged. Taking these factors into account, the overall uncertainty in the position at which a given dose occurs is likely to be ± 1.0 mm for diode measurements. The position of TLD dosimeters in the solid water phantom could be estimated with an uncertainty of approximately ± 0.25 mm.

Measurements with TLDs were, in addition, subject to several factors which limit the accuracy of the recorded dose. As discussed in Appendix A2.1, each TLD is subject to a random statistical fluctuation in sensitivity amounting to an uncertainty in dose of $\pm 2.0\%$. In measuring central axis depth dose, additional uncertainty in dose results from the dose-averaging process which takes place over the depth of the TLD. In the dose fall-off region, where dose changes rapidly with depth, this effect may be more significant than statistical fluctuations. For a TLD depth of 0.9 mm, the uncertainty in depth with which a given recorded dose actually occurs is approximately ± 0.5 mm.

The purpose of comparing TLD measurements of relative depth thermoluminescence with the relative depth ionisation of a diode was to establish

the significance of systematic errors present in the TLD measurements. Any TLD measurements of megavoltage electron fields in a solid phantom are subject to systematic errors. The most important of these are the depth dependence of TLD sensitivity and the perturbation in dose caused by the presence of the TLDs themselves. Scatter effects cause the variation in TLD sensitivity with depth in the phantom. At depths in excess of the D_{\max} depth, the average scatter angle of electrons increases, and electrons will, therefore, strike the TLD over a broader range of angles. Mobit *et al* [36] report a maximum variation with depth of 5% in sensitivity for LiF 100 TLDs in an electron beam of 5 MeV incident energy. The maximum variation decreased to 1% for a 20 MeV beam. Perturbation effects are due to the difference in densities of LiF and water. For a higher density material such as LiF, there is expected to be a net out-scatter of electrons. As a result, any TLD dosimeter situated in a solid water phantom will experience a greater in-scatter of electrons from other TLDs in the immediate vicinity. If this effect varies with energy (and hence depth), an error in relative depth dose measurements occurs.

The clinical situations examined in this work involved electron beams with incident energies in the range 12 – 20 MeV and often required TLDs to be positioned within 1.0 cm of each other, well within the practical range of electrons. It is necessary, therefore, to establish that scatter and perturbation effects are insignificant or to correct for them. An examination of the data comparing TLD measurements with those of a diode reveals that, in the dose fall-off region, the depths at which the same normalised thermoluminescence and ionisation occur generally agree to within 1.0 mm for the two measurement methods. In the dose plateaux, measured dose values obtained by the two methods agree to within 1.5% for the 16 MeV beam and to within 2% and 3% for the 6 and 12 MeV beams respectively. These differences are within the combined uncertainties of the measurements. There is thus no evidence to suggest the presence of a significant systematic difference between %depth thermoluminescence and %depth dose. TLD measurements of relative depth thermoluminescence were, therefore, converted to relative depth dose without applying any correction.

2.5.2 Calculation uncertainties

As well as being dependent on the basic competency of the pencil beam scatter algorithm, the accuracy of calculated data is limited by the size of the density and calculation grids, and by the number and spacing of the pencil beams. Both TMS and Cadplan were set to use calculation grids with a spacing of 2.5 mm. Since doses are obtained by an interpolation between grid points, this parameter plays an important role in limiting the accuracy with which relative dose can be predicted in the dose fall-off region of a %CADD curve.

More fundamentally, %CADD calculations performed by TMS and Cadplan rely heavily on the initial dosimetry measurements used to configure the algorithms. For both planning systems, calculated %CADD depends primarily on an estimate of the most probable energy at the phantom surface, E_0 . The user provides this parameter at the commissioning stage. E_0 was estimated by first obtaining a measured %CADD curve and extracting the value of R_{50} , the depth of 50% absorbed dose, for each beam energy. Values of E_0 were then obtained by multiplying values of R_{50} by the conversion factor 2.33 MeV cm^{-1} as recommended by the IPEMB [34]. The last stage of commissioning involves making fine adjustments to the values of E_0 such that the calculated %CADDs match the measured values. Any discrepancy between the treatment planning systems' predictions of %CADD and the measurements performed in this work will, therefore, reflect either differences between the commissioning measurements and those of this work or an error in the algorithm used to calculate %CADDs based on a value of E_0 .

2.5.3 Measured and calculated central axis depth doses

There is generally good agreement between TMS and the measured data for %CADD. In the dose fall-off region the depth at which a given calculated dose occurs is accurate to within 1.0 mm at depths greater than the D_{max} depth for all three beam energies considered (6, 12 and 16 MeV). In the dose plateaux, doses calculated by TMS are within 1% of the measured value in the vast majority of

cases, and within 2% for the remainder. Cadplan shows a similar degree of accuracy in most instances. For the 12 MeV beam there is a small displacement in the calculated curve towards shallower depths. The displacement, however, is within the measurement tolerance of 1.0 mm and so is insignificant. The most problematic area appears to be the shoulder of the depth dose curve where TMS underestimates the depth dose by approximately 3% for the 16MeV field. Cadplan shows a similar error for the 6 MeV field. One possible explanation for these errors is the failure of the planning computers to model explicitly electrons scattered from the sides of the applicator and cutout. These scattered electrons increase the %dose at shallow depths and cause the non-inverse square behaviour of electron beams observed at extended SSD [37].

Since the planning systems' calculations are essentially based on measured data, accurate prediction of %CADD does not require a successful implementation of the pencil beam scatter algorithm. This aspect of the depth dose calculation is, however, required in the prediction of dose distributions arising from the clinical beams described in experiments 2-5.

2.5.4 Oblique incidence

The first clinical beam experiment involved a 10 x 10 cm field obliquely incident on a plane phantom such that the beam central axis lay at an angle of 30° to the normal to the phantom surface. Oblique incidence effectively reduces the SSD at the proximal field edge and increases it at the distal edge. Non-standard SSDs change the shape of the beam penumbra (this is discussed further in chapter 3). It has also been demonstrated that oblique incidence reduces the vertical depth at which the dose maximum and 80% isodose line appear [38].

Both planning systems reproduce the general form of the measured isodose distribution produced by the oblique field adequately. The measured and calculated data both demonstrate the shift of the central axis dose maximum towards the surface. This corresponds closely with the chosen normalisation point which, at 2.7 cm along the central axis, has a vertical depth of 2.3 cm. The

reduction in depth of the 80% isodose line in comparison to the normal incidence %CADD data is also apparent in the measured and calculated data.

TMS shows excellent agreement with the measured data in the dose fall-off region and is accurate, for the most part, to within 1 mm in the beam penumbra. The calculated position of the 10% isodose is, however, only accurate to within 4mm at the distal penumbra and 5 mm at the proximal penumbra, TMS placing the line closer to the central axis than the measured data in both cases. Qualitatively, this is in agreement with Blomquist *et al*, who reported a 7 mm discrepancy at the low dose side of the distal penumbra for a field with 45° angle of incidence [19]. ICRU report 42 [23] states that errors in the dose calculation should amount to no more than 2 mm in isodose position in regions of high dose gradient or 2% of the dose in regions of low dose gradient. TMS predictions of penumbra for obliquely incident beams must, therefore, be interpreted with caution.

Cadplan predicts the dose fall-off region for the oblique field with slightly less accuracy than TMS, consistently underestimating the dose at a given depth. This is consistent with the findings of Samuelsson *et al* [20]. The discrepancy with measured data is, however, 2 mm or less and so just acceptable. In the beam penumbra, Cadplan predicts isodose position with acceptable accuracy everywhere except at the low dose margin. Maximum errors in isodose positions are 2 mm and 4 mm for the distal and proximal edges respectively. These are less than the discrepancies shown by TMS, though the requirement for caution when interpreting penumbra is still necessary.

2.5.5 Bolus edge phantoms

The clinical use of squared-off (90°) bolus edges is usually discouraged because electrons scattered from the bolus material create a severe hot spot immediately beneath and lateral of the bolus edge. This hot spot is clearly evident in both the measured and calculated isodose distributions shown in figures 2.10 and 2.11. A measured value of 130% was obtained for the hot spot while TMS and Cadplan calculated 119% and 135% respectively. As the volume which actually receives

the highest dose is very small, the exact value of this dose is of limited clinical significance. Of more relevance is the size of the area enclosed by the 105% and 110% isodose lines. Here there is sufficient qualitative agreement between both planning systems and the measured data to make the calculated isodoses a reasonably useful prediction of the size of the area receiving the high dose. Interpretation of the calculated isodoses requires caution, however. Both planning systems, for example, mistakenly portray the 110% isodose line extending up to the phantom surface when the measured data indicates that it occupies a minimum depth of 12 mm. An overestimation of the scatter contribution to relative dose at shallow depths behind the bolus edge would explain this error.

To reduce the severity of scatter-induced hot spots, bolus material is often tapered. An examination of the measured data from the 45° bolus edge experiment (shown in figures 2.12 and 2.13) indicates that this precaution does indeed reduce the hot spot dose. The highest dose measured under the tapered bolus was 114%, compared to 130% for the 90° edge. It is notable, however, that use of the tapered bolus fails to produce a significant corresponding decrease in the size of the area enclosed by the 110% isodose line. TMS agrees closely with the measured value of the hot spot while Cadplan overstates the severity of the hot spot by 8%. TMS is also more accurate in its prediction of the size and shape of the regions enclosed by the 105% and 110% isodose lines.

2.5.6 Cylindrical air cavity

The last experimental phantom simulated irradiation of the region overlaying the trachea. A comparison of the measured and calculated isodose distributions shown in figures 2.14 and 2.15 (pages 23 and 24) immediately reveals some marked discrepancies. At points lying laterally on either side of the air space, the depth of the 95% isodose line is incorrectly calculated by both planning systems. This is not related to the presence of the air space and is similar to the error in the position of the shoulder of the %CADD curve apparent in the TMS calculation of a 16 MeV field incident on a plane phantom (discussed above).

More importantly, both planning computers fail to predict the severity of the hot spot lying downstream of the air cavity. The measured data reveals the existence of a significant area receiving doses in excess of that at D_{\max} , with a hotspot of 107%. The planning computers both show maximum doses of 97%, a discrepancy of 10%. There is, in fact, a notable similarity between the dose distributions predicted by the two planning computers. Both systems continue to underestimate the dose for a considerable depth below the air space. For example, at a depth of 15 mm below the downstream edge of the air space, both planning systems still underestimate the dose by 10%. This is in broad agreement with the findings of Blomquist *et al* [19] for TMS though the maximum underestimation in dose reported in this earlier publication was 5%. At greater depth, dose gradients are dominated by the general fall-off in dose with depth, and the perturbation caused by the trachea becomes less obvious.

2.5.7 Performance of the TMS and Cadplan scatter algorithms

The bolus edge and air space phantoms present difficult tests for the planning computers. An accurate calculation of dose in the vicinity of the bolus and air space requires detailed modelling of the scatter processes undergone by electrons. The scatter algorithms employed by the two planning systems are similar and it would seem reasonable, therefore, to expect the two systems to calculate similar isodose distributions. This is generally true, with the exception of the hot spot values in the bolus edge phantoms. It is important to remember that the pencil beam scatter algorithms employed by the planning systems provide only an approximation of the multiple scattering events undergone by electrons. The scatter contribution which arises from pencil beams depends crucially on the values of the parameters chosen to characterise the spread of the Gaussian beams. In situations with extreme geometries such as the 90° bolus edge, the calculation of hot spots is very sensitive to these parameters' values and it is unsurprising to find discrepancies between the two planning computers and the measured data.

The discrepancies between calculated and measured dose beneath the cylindrical air cavity also arise from limitations in the implementation of the pencil beam algorithm. Both TMS and Cadplan use a semi-infinite slab approximation to

model pencil beams which encounter an inhomogeneity. This model assumes that the inhomogeneity has infinite lateral extent. The effects of this assumption were considered in detail by Lax [39], who concluded that the resulting failure to model the net in-scatter of electrons through the sides of an air cavity could produce a significant underestimation of the dose downstream of it. This is consistent with the results recorded in this work.

Appendix A2.1

Calibration of Thermoluminescent Dosimeters (TLDs)

Dose measurements were made with a batch of 100 TLD dosimeters. To allocate an individual calibration factor to each TLD, their relative sensitivity was determined by exposing the whole batch to the same dose of radiation and then reading each TLD. A mean luminescence reading was calculated for the batch and the relative sensitivity of each TLD found by taking the ratio of its reading to that of the mean. The average relative sensitivity in the batch is, therefore, exactly 1.

This entire process was performed six times and a mean of the six resulting relative sensitivities calculated for each TLD. These values were used as the calibration factors in subsequent measurements. The distribution of mean TLD sensitivities is shown below:

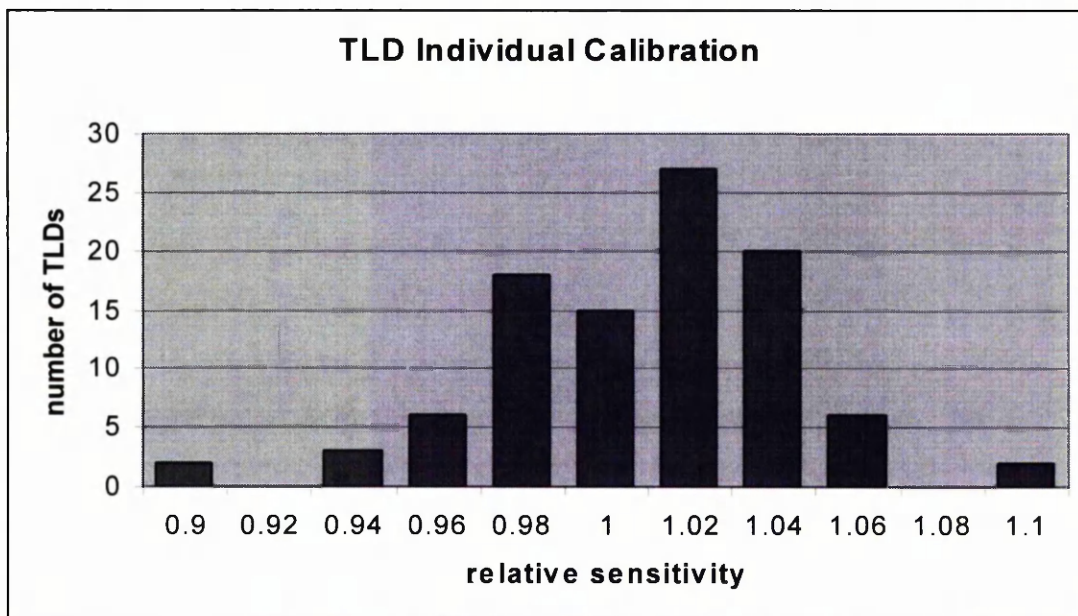


Figure A2.1. Frequency distribution of the relative sensitivity of 100 *LiF100* TLD dosimeters used in the measurement of 2D isodose distributions in WTe solid water.

The percentage standard deviation in the six values of relative sensitivity was now calculated for each TLD. This figure gives an indication of the reproducibility of measurements made with the corresponding TLD. For the entire batch, the mean

value of the percentage standard deviation, S , was 1.0%. Since the material, volume and shape of the TLDs are very similar, there is no reason to suppose that the true standard deviation varies between TLDs and so this mean figure was regarded as indicative of the reproducibility in sensitivity for each of the TLDs.

The standard error of subsequent TLD measurements is given by the expression

$$SE = \left(S^2/p + S^2/q + S^2/m \right)^{1/2} \quad (1)$$

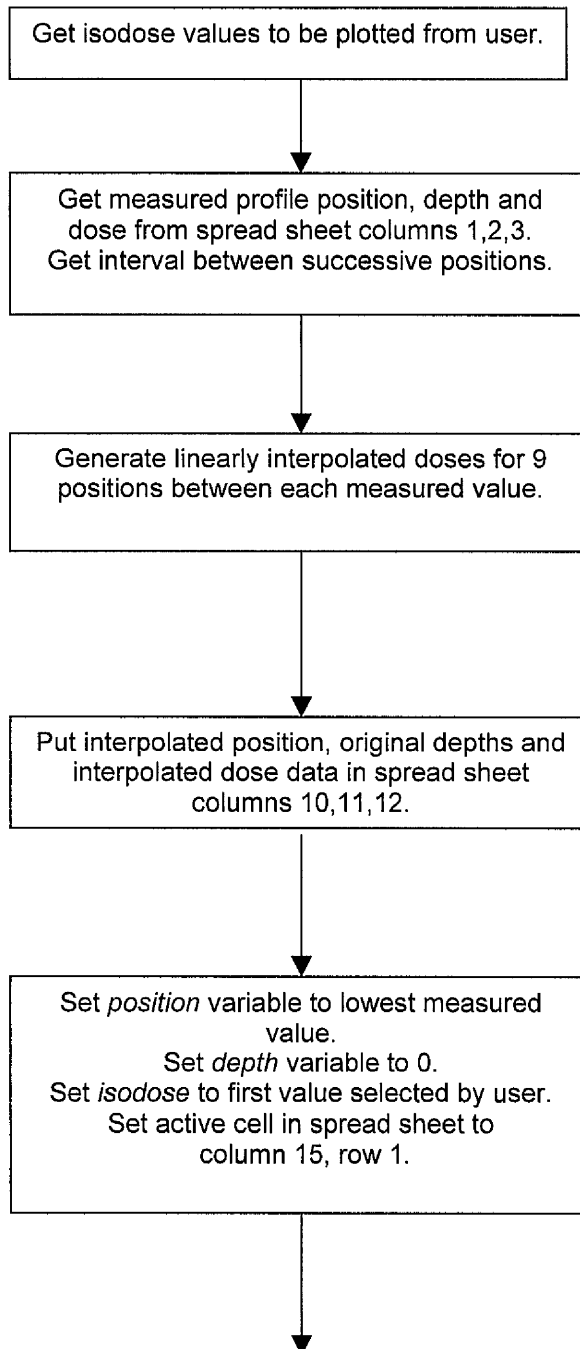
Where S is the standard deviation in the sensitivity of one TLD, p is the number of chips used to provide an absolute dose calibration, q is the number of chips used for the measurement in question, and m is the number of times the sensitivity of the given chip was assessed during the initial calibration process.

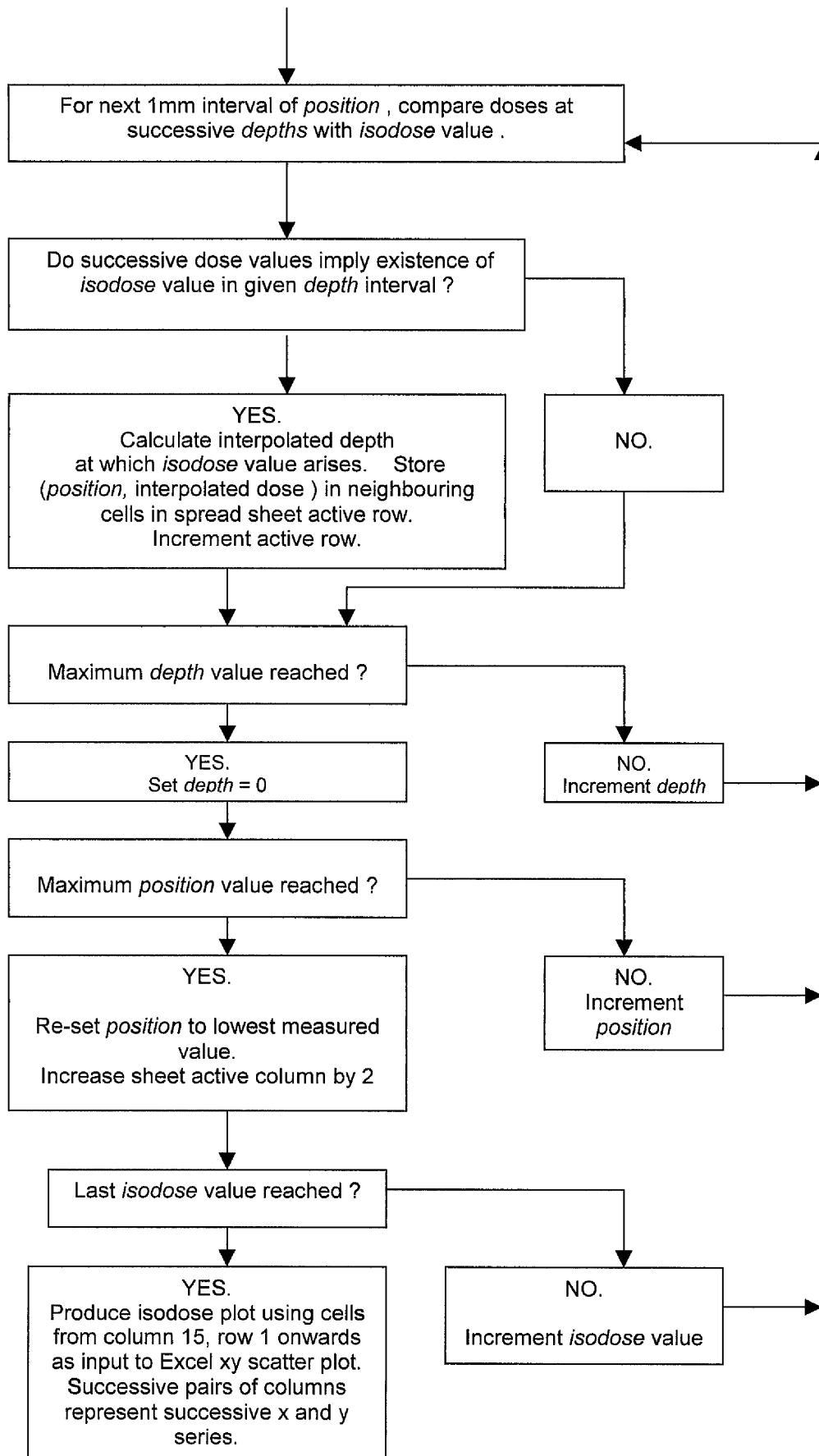
For relative dose measurements, the first term in equation (1) can be omitted. The respective values of q and m were 1, and 6, for this work. Equation (1) then gives a value of 1.1% for the standard error in a single measurement of thermoluminescence.

Appendix A2.2

Flow diagram of Microsoft Excel Visual Basic routine used for conversion of TLD point doses to isodose lines.

This routine operates on measured data residing in the first 3 columns of an Excel spreadsheet. The program processes this data and deposits the results in the same spreadsheet from column 15 onwards. Isodose plots are produced by using the processed data as input to the Excel graphs routine. Program variables in *italics*.





CHAPTER 3

BEAM PENUMBRA AT EXTENDED SSD

3.1 Introduction

The use of megavoltage electrons in the treatment of cancers of the head and neck is well established [2, 40 – 42]. Single field electron treatments are often useful for superficial lesions, while a combination of electron and photon fields are used for deeper lesions. In this latter case, lateral parallel opposed photon fields are often used to irradiate the primary disease until spinal cord tolerance is reached. The margins of the photon field are then moved anteriorly and an abutting electron field introduced to treat the cervical nodes. Dose homogeneity in the junction region is often an important consideration, and therefore the penumbra characteristics of abutting electron and photon beams require careful examination [43 – 45]. Unfortunately, the tendency of patients' shoulders to interfere with the electron applicator often necessitates treatment be given at extended SSD, and so a knowledge of the electron beam's penumbra at both standard and extended SSD is necessary.

It has been noted before that the penumbra characteristics of electron beams do not conform to the inverse square law [46,47]. This is due to the contribution of scattered electrons from the applicator, cutout and air column to the beam fluence at the phantom surface. The way in which scatter affects the relation between SSD and dose on the beam central axis has been previously modelled by use of a virtual source position [31,37,48]. This approach, however, has limitations. The virtual source position is machine specific and varies with energy and field size. Moreover, it has proved to be an inadequate description of the way penumbra location and width are affected by SSD, and alternatives such as Target Coverage Factor (TCF) have been proposed [49].

Both the Helax TMS and Varian Cadplan treatment planning computers implement a form of the virtual source approximation in their description of electron beam behaviour at extended SSD. Parameters affecting the width and position of the

penumbra at 100 cm SSD are defined by the user at the commissioning stage. Beam penumbra at extended SSD is modelled by a theoretical extrapolation of these parameters. Explicit measurements of the beam profile are not used by either planning system. This study compares the computers' prediction of electron beam penumbra at standard and extended SSD with measured data and assesses the optimum relative position of abutting photon and electron fields in clinical situations.

3.2 Materials and Methods

3.2.1 Electron beam set-ups

Measured and calculated dose profiles were obtained for a 10 x 10 cm field size (defined at 100 cm SSD). SSDs of 100, 105, 110 and 115cm were considered, the latter figure representing the largest SSD considered acceptable for clinical use at the Beatson Oncology Centre. Measured doses were compared with those calculated by Helax TMS v4.0A and Varian Cadplan v2.7.9. A calculation grid spacing of 1.0 mm was used for both computers.

Exposures were made with a Clinac 2100C linear accelerator (Varian Associates, as before) capable of producing electrons with energies 6, 9,12,16 and 20 MeV. Cutouts were housed in a 10 x 10 cm applicator designed such that the distance from the physical electron source to the mid depth of the cutout was 94.0cm. The applicator accepts field-defining cutouts constructed of low melting point ostalloy. At the Beatson Oncology Centre these have a thickness of 11mm irrespective of the electron energy in use. An interlock prevents operation of the accelerator unless a cutout is in place. To achieve a 10 x 10 cm field size, therefore, a square annulus of ostalloy with inner dimensions of 10 x 10 cm at 100 cm SSD is used with the nominal 10 x 10 cm applicator.

3.2.2 Measurement apparatus

Measurements were made with a diode in a water phantom. Solid state dosimetry

has been shown to be an ideal method of relative dose measurement in electron beams [50,51]. In comparison to ion chambers, the signal to noise ratio is very high as a result of the high sensitivity of diodes. Of particular relevance to penumbra measurements are diodes' comparatively small active volume and therefore high spatial resolution. The detector used in this work was a Scanditronix n-Si diode (QADOS Ltd, as before). This is a n-type detector with a sensitive volume of 0.3 mm^3 and an effective detection area of 2.5 mm diameter. The device was interfaced to a Therados DPD5 electrometer (Therados Instrument AB, Dalgatan 15, Uppsala, Sweden).

During measurements, the diode was situated in a polymethylmethacrylate (PMMA) cylindrical holder of thickness 2.5 mm, which could be moved along an axis perpendicular to the beam central axis. The water phantom containing this holder had dimensions of 40 x 40 x 40 cm, and was designed to be irradiated through its 5 mm PMMA side using a gantry angle of 90° or 270° . This arrangement is shown in figure 3.1.

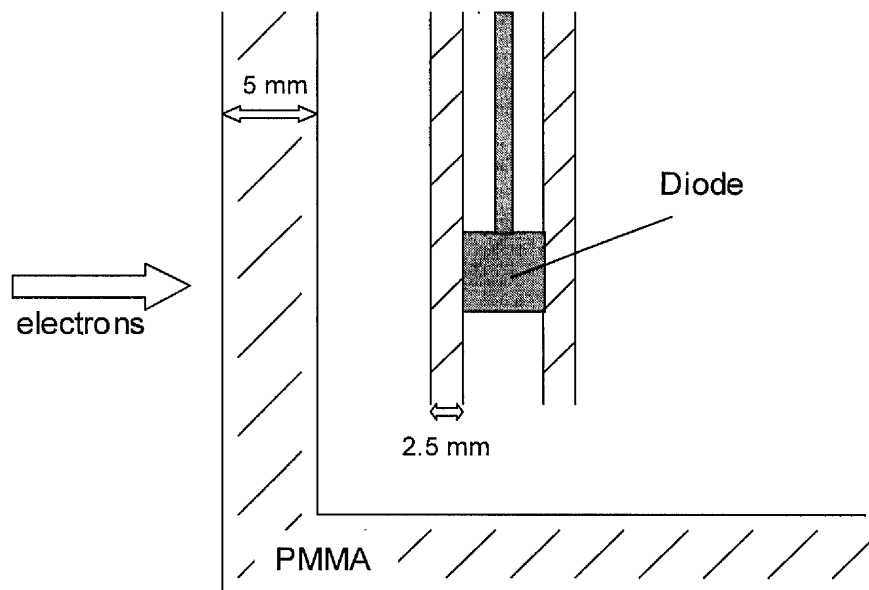


Figure 3.1. Arrangement of water phantom and diode for electron beam profile measurements. Electrons traverse 5mm of PMMA before entering water, then a further 2.5 mm of PMMA before reaching the diode detector.

Before entering the water, beams were thus subject to 5 mm of PMMA and later traversed 2.5 mm of PMMA before entering the detector. A total thickness of 7.5 mm of PMMA was therefore traversed by the electron beam for all measurements. Using a value of 1.15 for the ratio of the electron density of PMMA to that of water, and making the assumption that the mass stopping powers of PMMA and water are approximately equal [31], it is evident that this thickness is equivalent to approximately 8.7 mm of water. The depth of water between the phantom wall and PMMA holder was varied according to the electron energy such that the total water equivalent depth was approximately equal to the depth of dose maximum at 100 cm SSD for each energy. These total depths were 1.5cm for 6MeV beams, 2.1cm for 9 and 12 MeV and 1.7cm for 16 and 20 MeV.

3.2.3 Diode measurements

Before commencing profile measurements, the linearity of the diode's response to absorbed dose was established for electron beam energies of 6 and 16 MeV. This was achieved by comparing diode readings with absorbed dose as detected by the ion chambers of the linear accelerator. The results are shown in appendix A3.1. Interestingly, there is a small difference in the ratio of diode reading to monitor units for the two energies. This is more likely to reflect energy dependence in the response of the diode than it is to reveal a calibration error in the accelerator monitor chambers. The linearity of diode response for beam energies 6 and 16 MeV was assumed to imply a linear response at the other available beam energies.

Prior to each set of measurements, the water phantom (with diode *in situ*) was left in the accelerator room for a period of at least 1.5 hours to achieve temperature equilibrium. Measurements were made using a gantry angle of 90°. Electron beam profiles were obtained by measuring at a series of discrete points along an axis perpendicular to the beam central axis and to the plane of rotation of the accelerator gantry (this corresponds to the photon collimator Y axis).

Measurements were made at beam energies 6, 9, 12, 16, and 20 MeV and at SSDs in the range 100 cm to 115 cm. Each measurement was repeated 3 times and an arithmetic mean taken. To reduce systematic errors due to variations in machine

output and diode sensitivity (the latter caused mainly by temperature fluctuations), the central axis dose was re-measured after every three off-axis measurements.

For the measured data, target coverage factors (TCFs) have also been calculated according to the definition given by Das *et al* [52]

$$\text{TCF}(n) = \frac{W_n}{W_{50}}$$

Where W_n is the width of the $n\%$ isodose line at a given SSD and W_{50} is the geometric field width at 100 cm SSD. Widths are measured at the depth of dose maximum. TCF(90), for example, represents the ratio of the width of the 90% isodose line to the geometric field size.

3.2.4 Abutting photon and electron fields

To assess the junction region between abutting photon and electron beams, electron beam profiles were added to photon beam profiles measured separately. Two beam set-ups were considered. Both set-ups consisted of isocentric parallel opposed 6 MV photon fields measuring 10 x 10 cm at their isocentre, abutted to a single fixed SSD electron field having dimensions 10 x 10 cm at 100 cm SSD. For the first beam set-up, a SSD of 100 cm was used for the electron field. The second set-up modelled extended SSD treatments by using a SSD of 110 cm for the electron field. The beam set-ups are shown in figure 3.2.

For each beam set-up two photon dose profiles were obtained. Each was measured at a photon Focus to surface distance (FSD) of 92.0 cm, the first at a depth in water of 2.0 cm and the second at a depth of 14.0 cm. The measurement protocol for obtaining relative off-axis doses was the same as that described above for electrons. Adding doses from the corresponding off-axis points of the two profiles results in a combined profile equivalent to that which would be obtained by a single measurement at 2.0 cm depth in a phantom of total separation 16.0 cm exposed to parallel opposed photon fields with a common isocentre at the mid

point of the phantom and a source to isocentre distance of 100.0 cm. A separation of 16 cm is typical of those encountered clinically in neck irradiations.

The photon and electron profiles were assigned relative weighting factors such that the dose delivered by the electron field to the depth of dose maximum on its central axis was the same as that delivered by the combined photon fields to their isocentre. A weighted sum was then calculated to yield the combined photon and electron beam profile resulting from abutting fields. Profiles were combined by firstly selecting a notional distance between photon and electron beam central axes. Photon and electron doses at corresponding points were then summed to yield the combined profile. The size of the gap which would appear between the light field edges of abutting photon and electron field edges is determined by the relative position of the central axis of the two fields. Adding profiles such that a point 50 mm from the photon central axis coincides with a point 50 mm from the

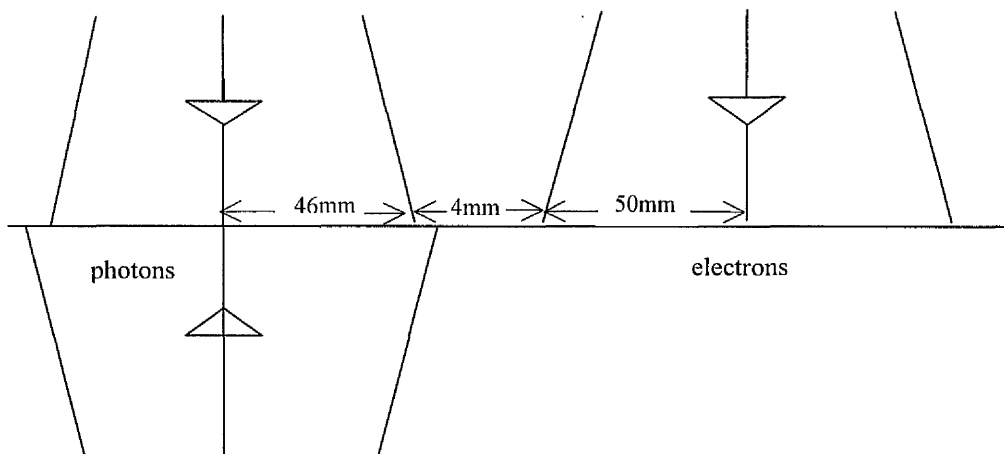


Figure 3.2. Field edge positions for abutting isocentric photon and fixed SSD electron fields at the surface of a 16 cm separation phantom. Central axis separation of 100 mm. Photon isocentre is at a depth of 8 cm.

electron central axis is equivalent to a gap of 4 mm at the phantom surface for a 100 cm SSD electron field, as illustrated in figure 3.2.

3.3 Results

Figures 3.3 – 3.7 show beam profiles for electron energies from 6 to 20 MeV. At each energy, measurements are compared with data calculated by the TMS and Cadplan planning computers. In each case, *Y position* represents distance from the beam central axis and *% dose* represents the ratio of the off-axis dose to that on the central axis. Measurements and calculations were made at, or near, the depth of dose maximum for each energy. These depths were 1.5 cm for the 6 MeV field, 2.1 cm for the 9 and 12 MeV fields and 1.7 cm for the 16 and 20 MeV fields. Since the field defining cutouts are symmetrical, only one half of the profile was recorded.

Target Coverage Factors for the 10%, 50% and 90% isodose lines resulting from a single electron field have been calculated from the measured data and are shown in figure 3.8. Trend lines describing the relation between TCF and SSD are displayed. These have been extrapolated 5 cm beyond the shortest and longest SSD at which measurements were made. The justification for this is given in section 3.4 (Discussion). TCF(10), indicative of the area enclosed by the 10% isodose line, increases more rapidly with SSD than TCF(50) or TCF(90). Generally, TCF(90) varies very slowly with SSD, indicating that the useful treatment area is not increased by increasing the beam's SSD.

Figure 3.9 shows measured dose profiles across the junction region for abutting photon and electron fields. Clinically, the most commonly encountered energies are 9, 12 and 16 MeV. For each of these, electron field SSDs of 100 cm and 110 cm are considered. In each case, the electron field central axis is located at position "0" on the horizontal axis. The electron and photon fields are, therefore, on the left and right of the junction respectively. Separately measured photon and electron fields were manually added to produce the final profile. During this process the size of the gap between photon and electron light field edges was varied in order to find its optimum length. The optimum gap size was taken as the

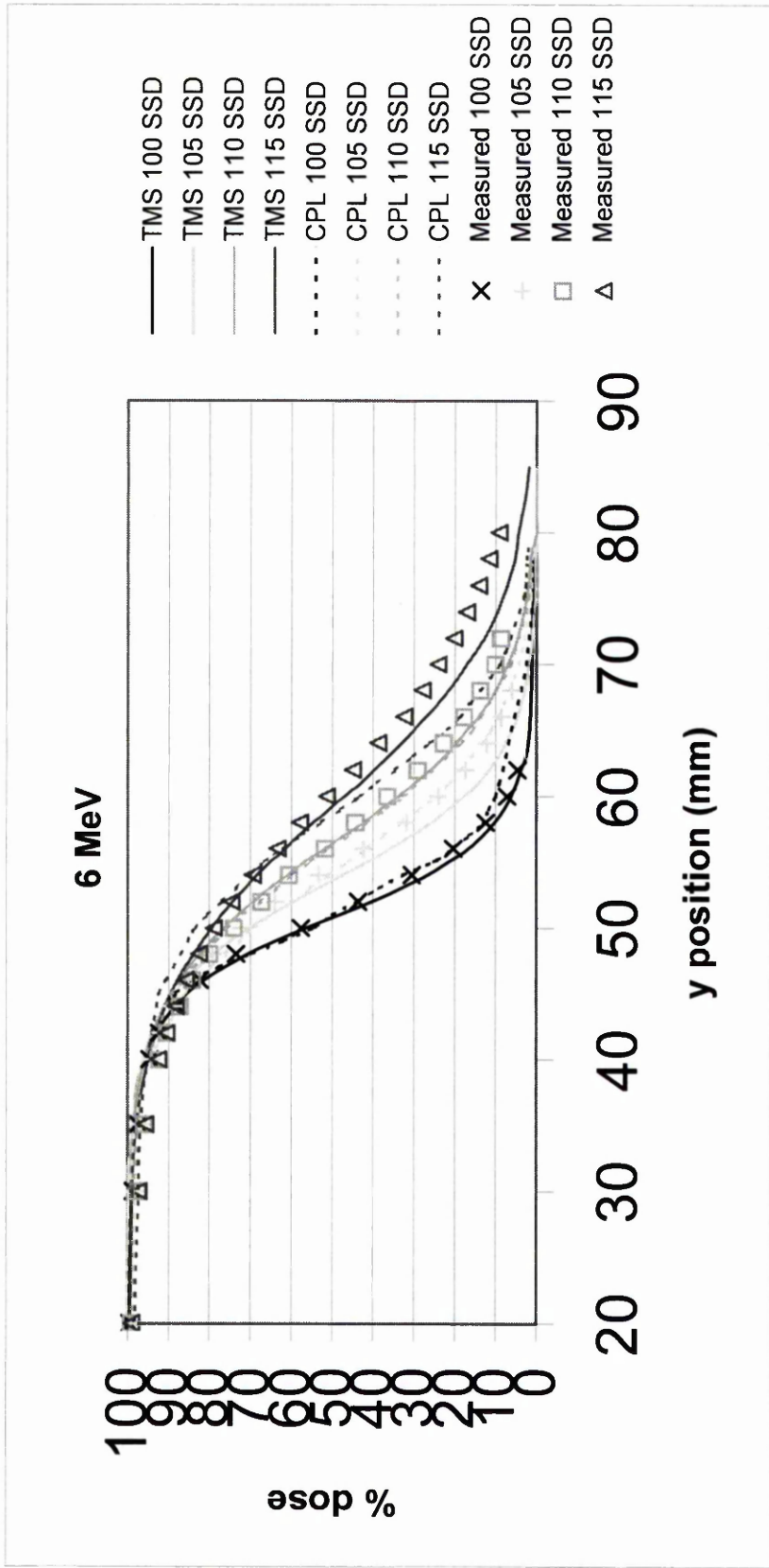


Figure 3.3. Comparison of measured and calculated dose profiles at the Dmax depth for a 6 MeV, 10 x 10 cm electron beam. SSDs of 100, 105, 110 and 115 cm are shown. "y position" represents distance from the beam central axis. For clarity, errors of +/- 1 mm on measured doses are not displayed.

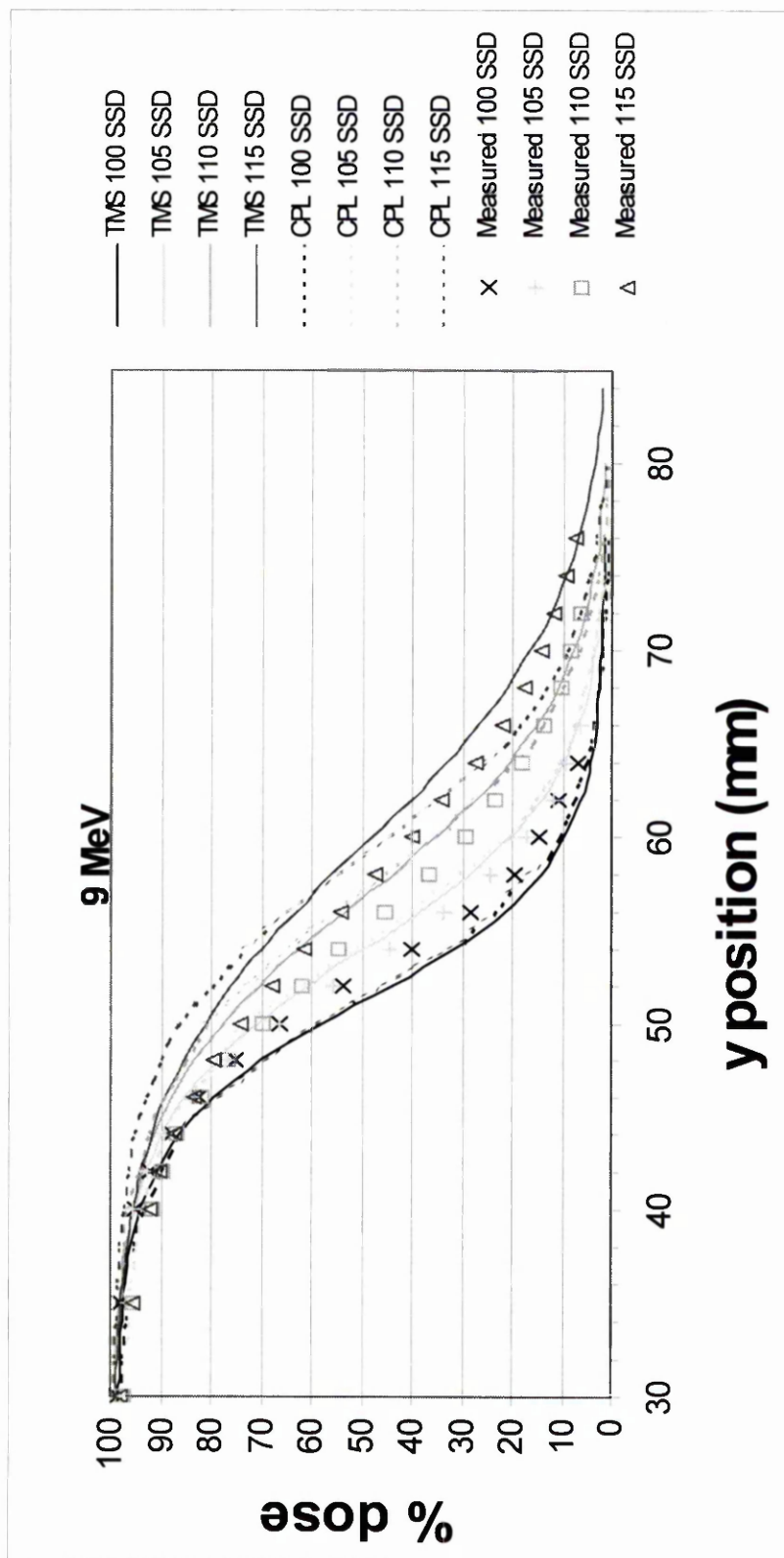


Figure 3.4. Comparison of measured and calculated dose profiles at the Dmax depth for a 9 MeV, 10 x 10 cm electron field. SSDs of 100, 105, 110 and 115 cm are shown. "y position" represents distance from the beam central axis. For clarity, errors of +/- 1 mm on measured doses are not displayed.

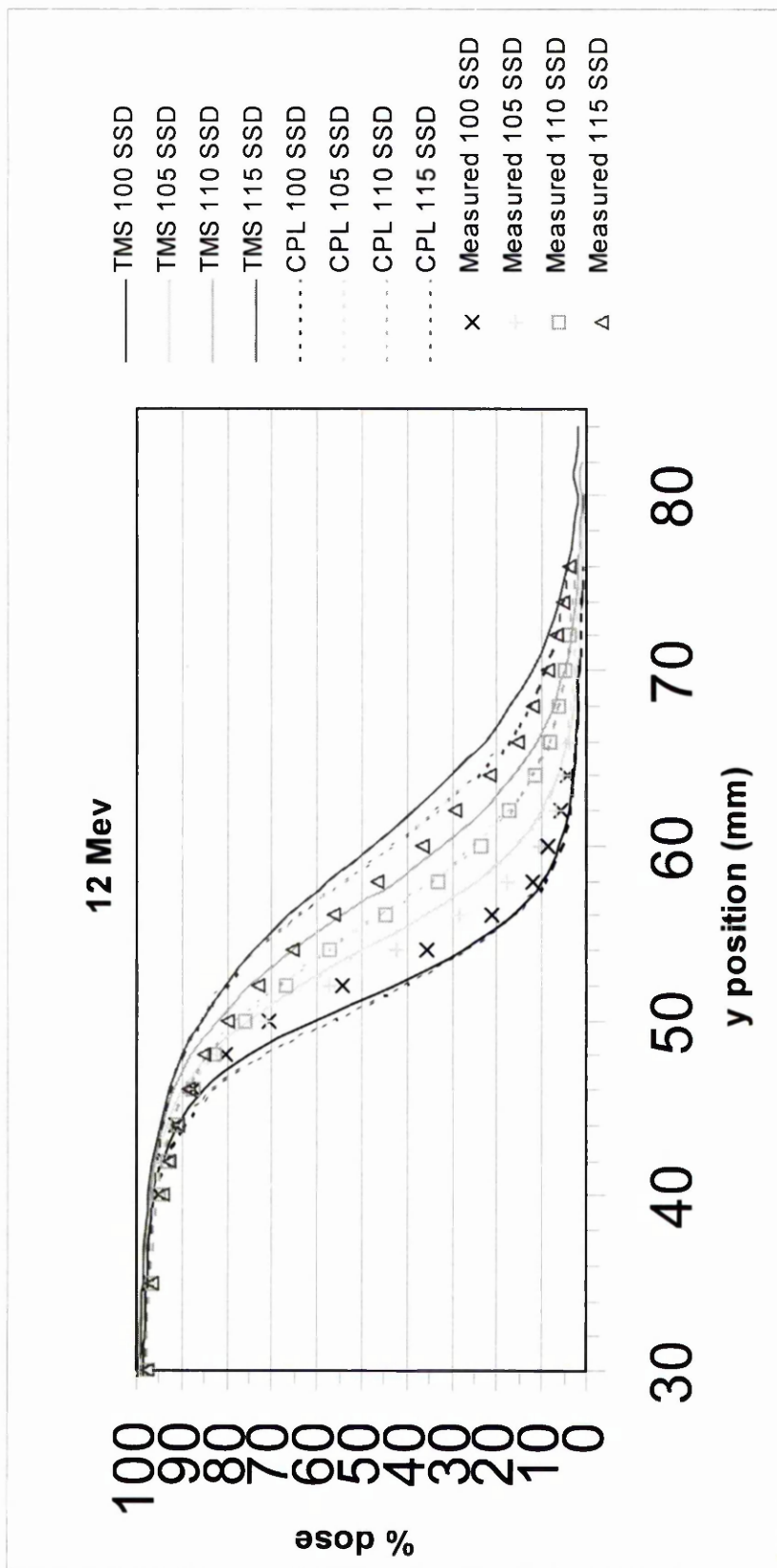


Figure 3.5. Comparison of measured and calculated dose profiles at the Dmax depth for a 12 MeV, 10 x 10 cm electron field. SSDs of 100, 105, 110 and 115 cm are shown. "y position" represents distance from the beam central axis. For clarity, errors of +/- 1 mm in measured doses are not displayed.

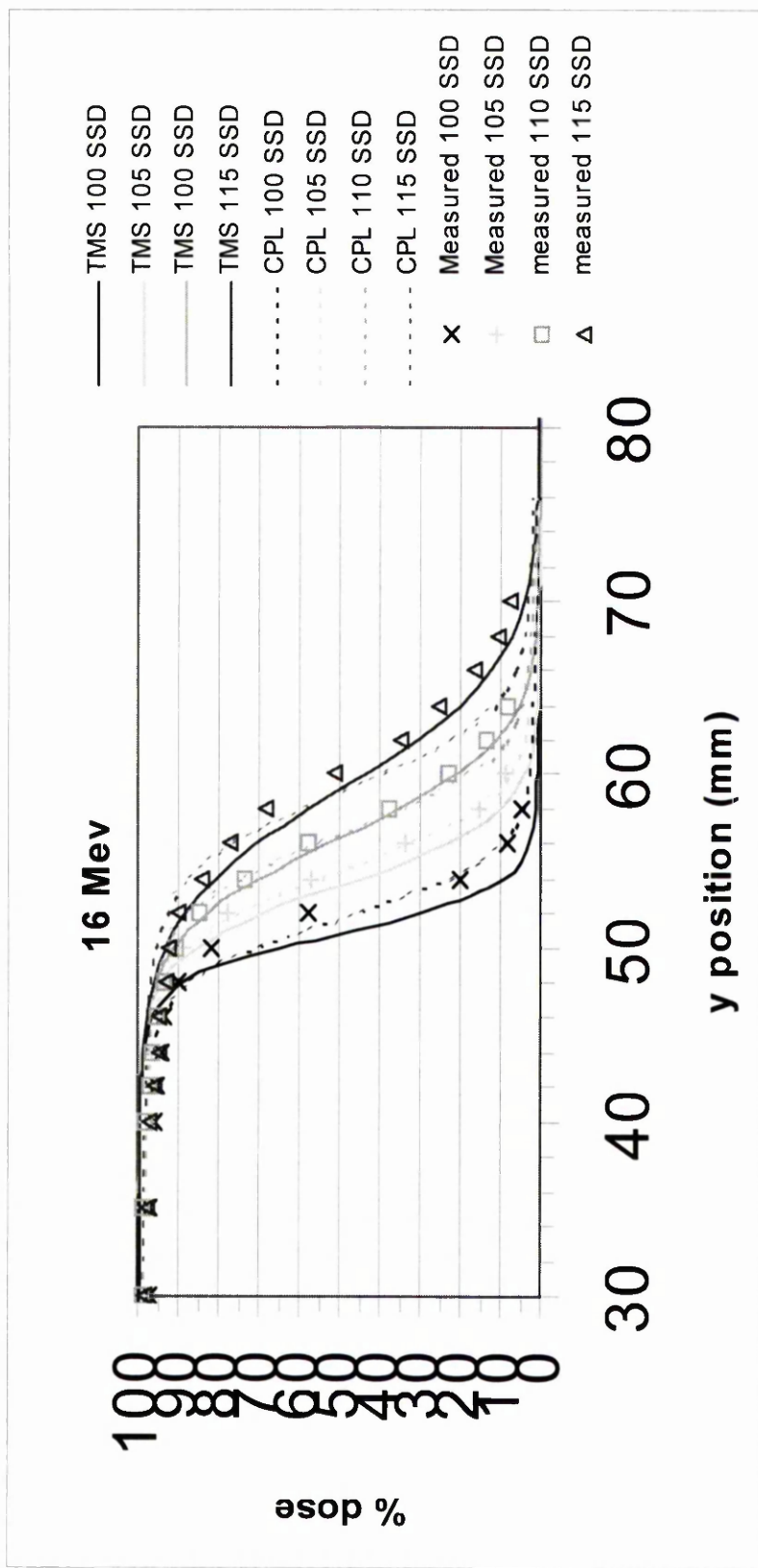


Figure 3.6. Comparison of measured and calculated dose profiles at the Dmax depth for a 16 MeV, 10 x 10 cm electron field. SSDs of 100, 105, 110 and 115 cm are shown. "y position" represents distance from the beam central axis. For clarity, errors of +/- 1 mm in measured doses are not displayed.

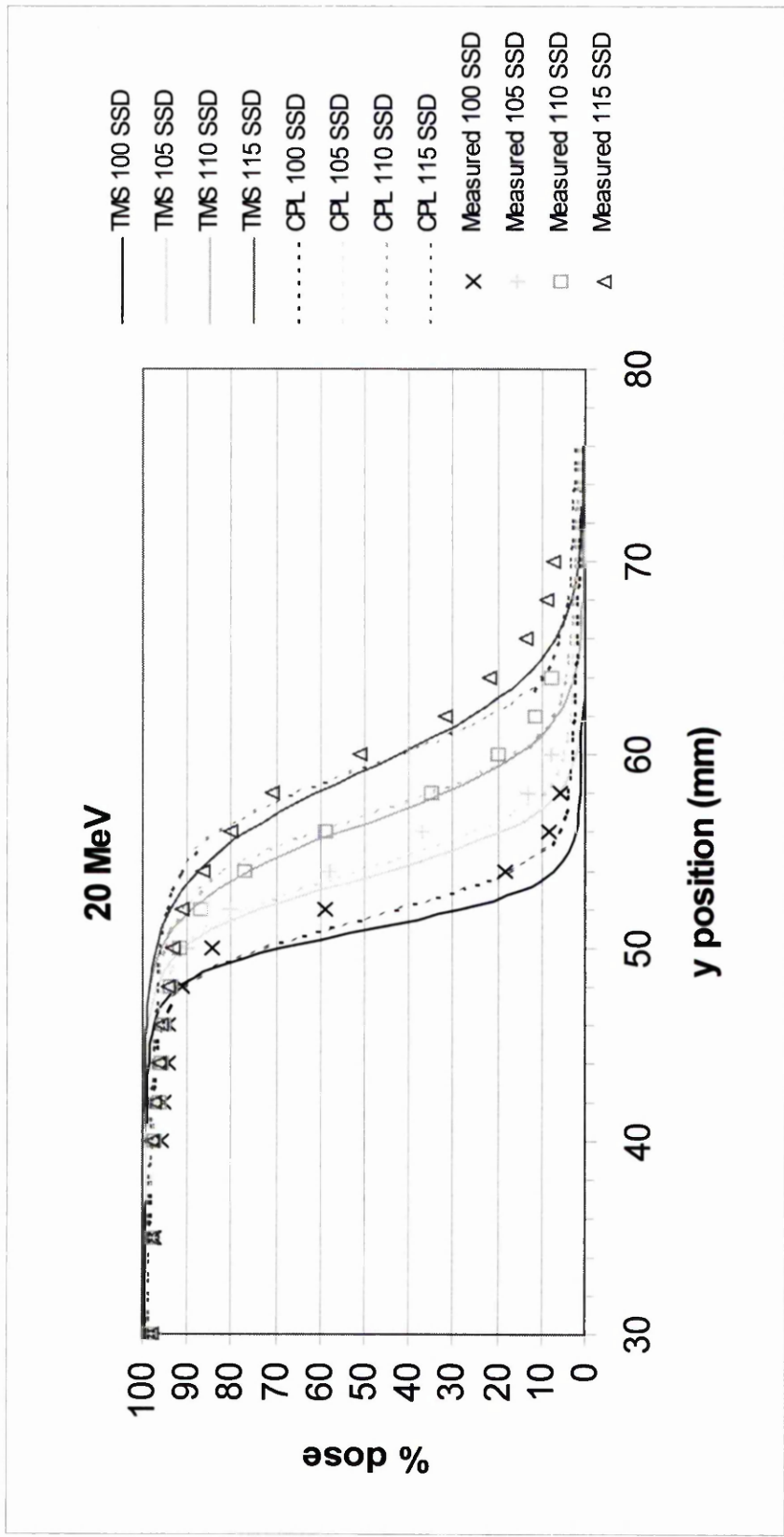


Figure 3.7. Comparison of measured and calculated dose profiles at the Dmax depth for a 20 MeV, 10 x 10 cm electron field. SSDs of 100, 105, 110 and 115 cm are shown. "y position" represents distance from the beam central axis. For clarity, errors of +/- 1 mm in measured doses are not displayed.

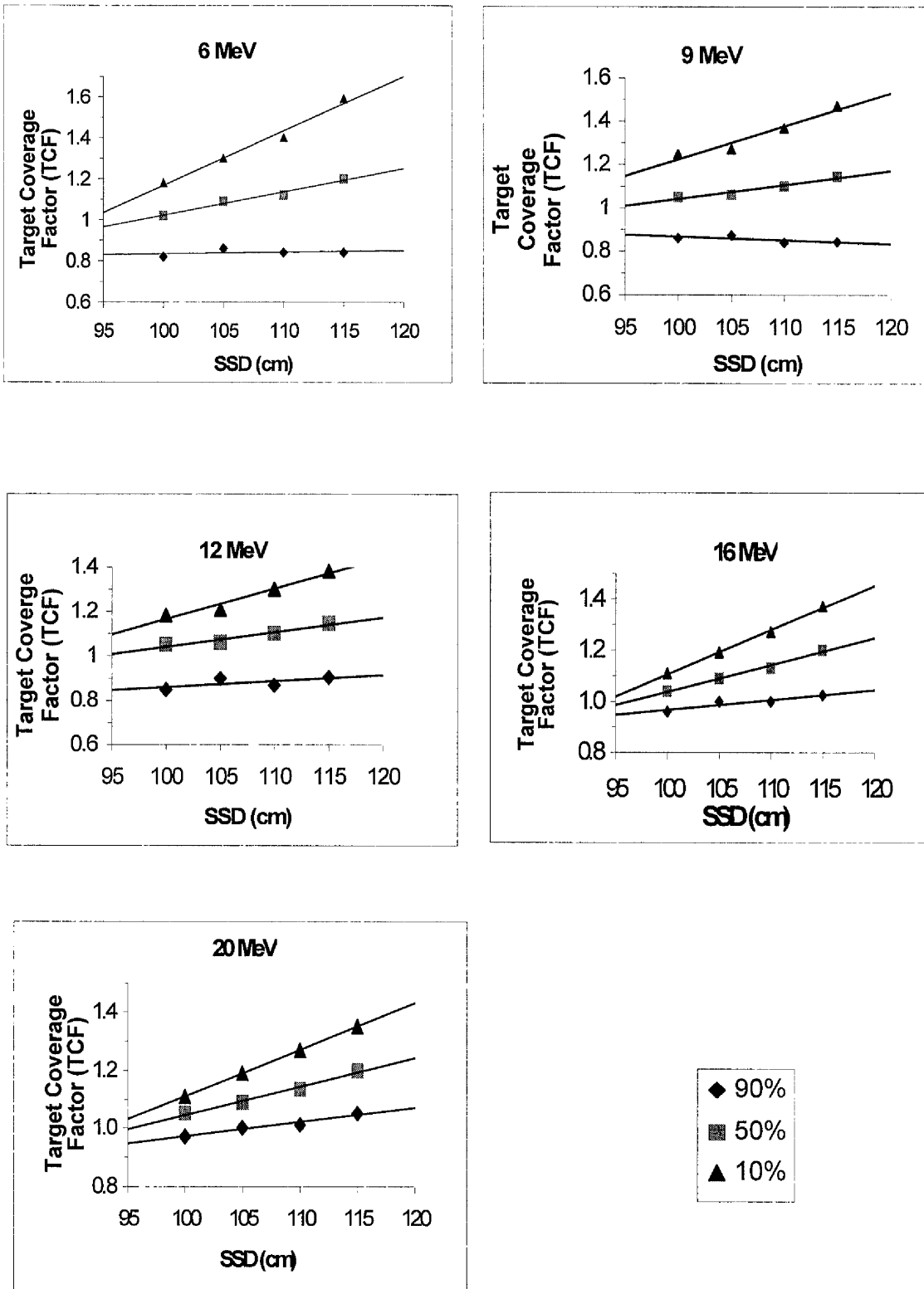


Figure 3.8. Target Coverage Factors (TCF) factors for electron beams of energy 6 – 20 MeV. TCF represents the ratio of the width of a given isodose line to the geometric field size at 100 cm SSD. Error bars in TCF of +/- 1.5% have been omitted for clarity.

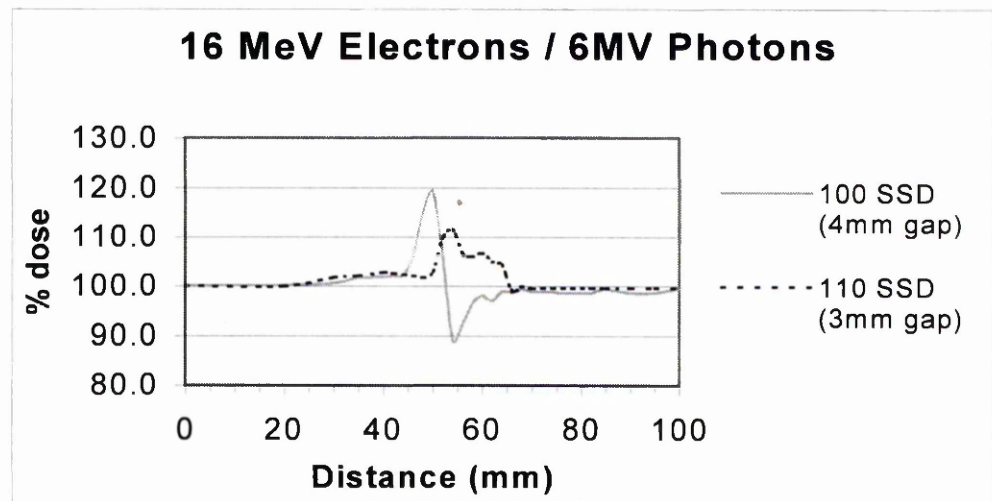
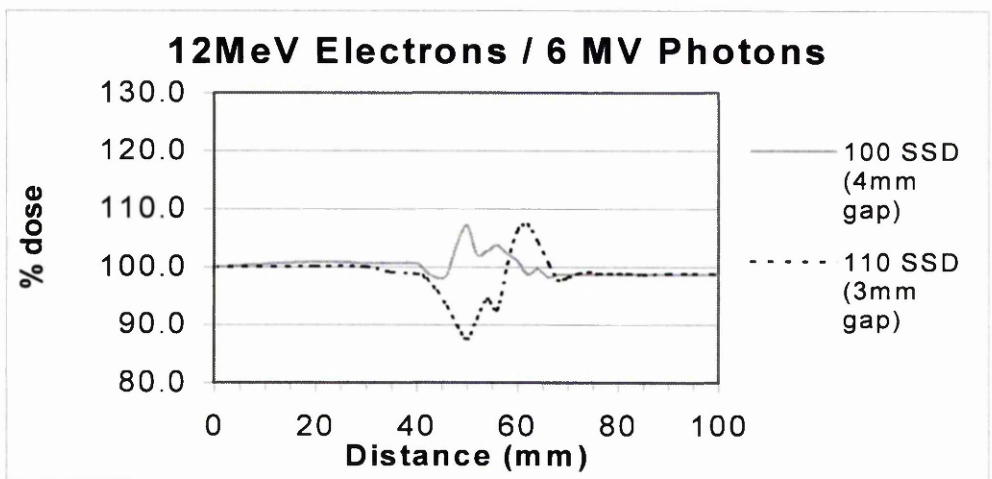
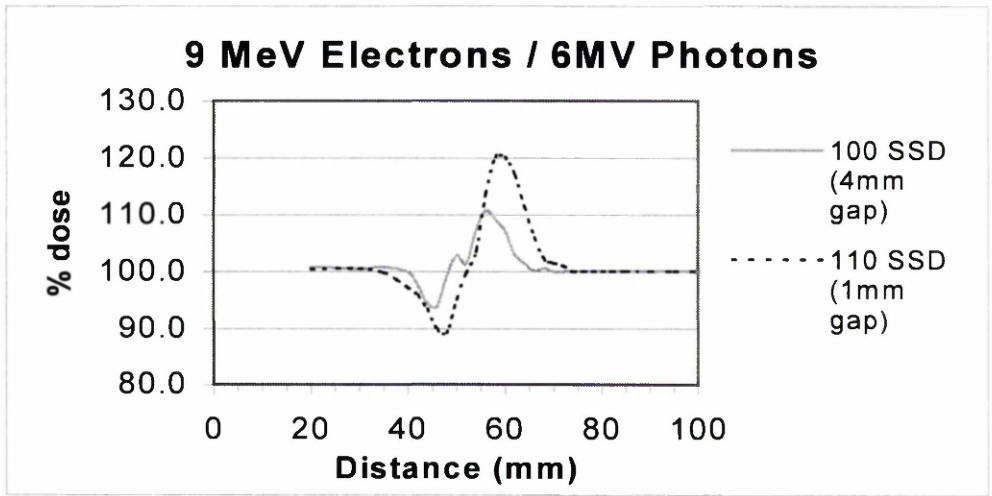


Figure 3.9. Dose profiles at the Dmax depth for a 16 cm separation phantom irradiated with isocentric parallel opposed photon fields abutted with a single fixed SSD electron field. Electron fields are to the left of the junction. Electron energies of 9, 12 and 16 MeV are shown. Photon energy is 6 MV. Gaps between the fields are the optimum sizes shown in table 3.1

| Electron Energy (MeV) | Electron field SSD | Optimum gap (mm) |
|-----------------------|--------------------|------------------|
| 16 | 100 | 4 |
| 16 | 110 | 3 |
| 12 | 100 | 4 |
| 12 | 110 | 3 |
| 9 | 100 | 4 |
| 9 | 110 | 1 |

Table 3.1. Optimum gap sizes for a 16 cm separation phantom irradiated with isocentric parallel opposed photon fields abutted with a single fixed SSD electron field. Gap sizes are the distances between light field edges.

largest gap which resulted in the minimum dose across the profile being no lower than 90% of the maximum dose on the electron central axis. A minimum of 90% dose was chosen because this is often the minimum dose specified in treatment prescriptions. Table 3.1 gives a summary of the optimum gap sizes. Using an upper limit to the minimum junction dose as the basis for field gap selection has potentially undesirable consequences for the *maximum* dose across the junction. Hot spot doses of 120% are evident for the 9 MeV extended SSD junction, and for the 16 MeV standard SSD junction.

3.4 Discussion

This work has involved the acquisition of dose profiles for a 10 x 10 cm electron beam at standard and extended SSD. Beam energies of 6, 9, 12, 16 and 20 MeV have been considered for SSDs in the range 100 – 115 cm. Measurements made with a diode in a water phantom have been compared to calculated data generated by two treatment planning computers: Helax TMS and Varian Cadplan. Data has been presented in graphical form as plots of dose against Y axis distance and as plots of Target Coverage Factor (TCF) against SSD. TCF provides an indication of how the area covered by an isodose line varies with SSD. Finally, dose profiles

in the junction region of abutting electron and photon fields have been obtained for both standard and extended SSD treatments.

3.4.1 Uncertainties in measured and calculated doses

Both the measured and computed dose profiles are subject to limitations in their accuracy and reproducibility. Measurements were made with a diode detector which could be positioned with an estimated uncertainty of ± 0.25 mm. The precision in measuring the position of an isodose line was thus no better than ± 0.25 mm. The final precision in isodose position is also affected by the *accuracy* of dose detection. Since measurements were taken in a region of rapidly changing dose, accuracy was limited by the size of the active volume of the detector. The diode used in this work had an active volume of diameter 2.5 mm. In the penumbra region, absorbed dose may vary by as much as 60% over this distance, dependent on beam energy and SSD. The accuracy of the measurement is thus compromised by the resultant dose averaging process which occurs over the detector volume.

Diode measurements are also subject to statistical fluctuations in the amount of charge collected for a given dose. It is likely, however, that at the levels of absorbed dose used in this work, these fluctuations are insignificant [50]. It is difficult to quantify the total uncertainty in accuracy but it would seem reasonable to assume that the error imposed by the dose-averaging process combined with the inherent uncertainty in detector position leads to an overall uncertainty in measured isodose line position of ± 1.0 mm in the penumbra.

The computed data has a spatial resolution limited by the calculation grid spacing: in this case 1.0 mm. The accuracy of the computed data is determined by the number and spacing of the pencil beams used to model electron scatter in the phantom and by the accuracy with which the electron fluence profile at the phantom surface is defined. The fluence profile is dependent on machine specific

parameters such as scattering from the photon collimators, applicator and cutout, and on the distance from the cutout to the phantom surface.

3.4.2 Calculation algorithms

Neither the TMS nor Cadplan systems explicitly model electron scattering in the machine head. To describe electron behaviour in extended SSD fields, both systems use the concept of an energy dependent root mean square scattering angle, θ_{rms} , of the in-air electron fluence. This parameter describes the extent to which the average angle of travel of a given electron deviates from the direction of the beam central axis. The TMS and Cadplan physics manuals both recommend θ_{rms} be selected by the user at the commissioning stage. Neither manufacturer suggests explicit values for the parameter; the values used in this work were based on those recommended by Lax [53]. These were then adjusted such that the calculated penumbra shape matched the measurements as closely as possible at 100 cm SSD. A typical value for θ_{rms} was 0.025 radians for a 9 MeV beam.

In TMS, the value of θ_{rms} at the phantom surface is combined with a radial broadening parameter, r_{gap} , to define the angular and radial spreading of the pencil beams at depth in the phantom. A theoretical algorithm first described by Lax and Bramhe [28] is used to increase the values of θ_{rms} and r_{gap} in proportion to the distance from the cutout to the phantom surface, and is the mechanism responsible for broadening beam penumbra at extended SSD.

TMS calculates the position of the centre of the penumbra (the 50% isodose line) by referring to an algorithm based on data from a set of Full Width at Half Maximum (FWHM) measurements made by the user at the commissioning stage. The literature accompanying TMS recommends FWHM measurements are made on a 20 x 20 cm field size at 100 cm and 110 cm SSD, for each electron energy. This data allows TMS to calculate, for each beam energy, a virtual source position (VSP). It is assumed that the VSP is independent of field size. In modelling

electron beams at extended SSD, the 50% isodose position is found by applying an inverse square expansion based on the VSP for the appropriate energy. TMS should, therefore, predict with reasonable accuracy, the position of the 50% isodose line for electron beams of SSD up to and including the FWHM measurement value of 110 cm.

The theory adopted by Cadplan to increase the angular and lateral spreads of pencil beams at depth is, like TMS, based on the work of Lax [53]. There is an important difference in the method used to predict the centre of the penumbra, however.

While TMS bases its calculation on measured FWHM data, Cadplan defines the 50% isodose line position entirely theoretically according to a formalism developed by Huizenga and Storchi [54]. Pencil beams are assigned a weighting according to whether or not their central axis traverses the field defining cutout. The weighting factor may have one of only two values: full weighting (for pencil beams not traversing the cutout), or a weighting reduced by the transmission factor of the cutout.

3.4.3 Comparison of measured and calculated doses

An examination of the measured and calculated field profiles reveals that the 50% isodose position is predicted accurately by both TMS and Cadplan. For all beam energies the calculated and measured positions of 50% dose lie within 2 mm throughout the range of SSDs considered i.e. within the combined uncertainties of the measured and calculated values. A real discrepancy in isodose position of up to 2 mm is generally regarded as acceptable accuracy [23]. Since TMS bases its calculation on measured data, the small discrepancies between its calculations and the measurements are likely to result purely from minor systematic differences between the commissioning measurements and those performed for this work. The success of the alternative theoretical approach to predicting 50% isodose position adopted by Cadplan is confirmed by the similarity of the Cadplan predictions with those of TMS and the measurements.

The positions of the low and high dose edges of the penumbra are predicted with less accuracy by the planning computers. It is notable that, for both systems, modelling of electron interactions in the field-defining cutout is limited to a modification of the effective beam weight to account for the transmission factor of the cutout. No attempt is made to account for the increased scattering power of the cutout material. The resulting increase in θ_{rms} for electrons transmitted by the cutout is, therefore, neglected. It is thus reasonable to expect that pencil beam broadening will be under-estimated by the planning computers and that there will be a consequent under-estimation of penumbra width. This effect should not be apparent at the standard SSD of 100 cm since θ_{rms} is selected by the user to match the measured penumbra, but a significant effect may be expected at extended SSD as the scattered electrons have a greater distance to traverse before reaching the phantom.

There is clear evidence that the calculated isodose positions at the far (low dose) edge of the penumbra are consistent with this failure to predict penumbra broadening. For Cadplan this trend is particularly notable at 115 cm SSD. With the exception of the 12 MeV beam, the calculations consistently place the 10% isodose line inside the measured position. Generally the discrepancy is approximately 4 mm but for the 6 MeV beam it is 9 mm. A similar trend is apparent at 110 cm SSD though here Cadplan's calculations are more accurate: the maximum discrepancy from measured data is 4 mm. The TMS calculations at the far penumbra edge show similar trends to those of Cadplan without exhibiting as large a discrepancy at 6 MeV. The maximum discrepancy from the measured data is 5 mm, again at 6 MeV and 115 cm SSD.

It is evident from a general examination of the beam profiles that the higher energy beams (16 and 20 MeV) are modelled with greater accuracy by both planning systems. This is particularly true at the high dose (near) side of the penumbra at extended SSD. At extended SSD, both systems trend towards greater discrepancies for the 6, 9 and 12 MeV beams. The calculated position of 90% dose is consistently placed further from the beam central axis than its measured position. Cadplan exhibits the greater discrepancies from the measured data: up to

6 mm for a 9 MeV beam at 115 cm SSD. The tendency for both systems to overestimate the distance from the beam central axis to 90% dose is again consistent with a failure to predict penumbra broadening. The fact that this effect is more pronounced at lower beam energies (for which the scattering power of the cutout is increased) is further evidence for the planning systems' underestimation of θ_{rms} for electrons transmitted through the cutout.

For the 9 MeV field, a trial and error approach revealed that the value of θ_{rms} stored in Cadplan had to be doubled from 0.025 radians to 0.05 radians to achieve a match between the measured and calculated penumbra at 115 cm SSD. Making this change, however, had the undesirable effect of broadening the beam penumbra at 100 cm SSD to an unacceptable size.

3.4.4 Target Coverage Factors (TCFs)

It is notable that both planning systems consistently produce errors in isodose position of considerably more than 2 mm at the near and far sides of the penumbra at extended SSD. Calculated isodose distributions in the penumbra must, therefore, be interpreted with extreme caution. If an estimation of isodose position at extended SSD is required clinically, a more realistic approach may be to examine the measured TCF factors.

TCF(90) is likely to be most useful for this purpose, as dose prescription is often to 90% dose for electron treatments. It is interesting to note that TCF(90) varies very slowly with SSD. For beam energies 6-12 MeV its value either increases slowly or remains static with increasing SSD. At 9 MeV, for example, TCF(90) remains in the range 0.87 – 0.84 for SSDs between 100 and 115cm SSD (inclusive). This corresponds to a range of 87 mm – 84 mm of 90% coverage at the Dmax depth, irrespective of SSD. There is, on the other hand, a small increase in the value of TCF(90) with SSD for 16 and 20 MeV beams. At 20 MeV the increase is monotonic and in the range 0.97 to 1.05. These findings contradict those of Das *et al* [49] who predicted a decrease in TCF(90) with increasing SSD for all beam energies.

A possible explanation for the discrepancy between these results and those of Das *et al* may lie in the shape of applicator used with the Clinac 2100C linear accelerator. The applicators used in this work have a rectangular cross-section throughout their length. Das *et al* report using cone-shaped applicators. Since applicator design is a significant factor in determining scattering and beam profile, it is perhaps not surprising to find differences in TCF factors.

While TCF(90) is a static or slowly varying function of SSD, TCF(10) shows a rapid expansion. At the 6 MeV beam energy TCF(10) increases from 1.18 to 1.59 on moving from 100 cm to 115 cm SSD. This corresponds to an additional 4.1 cm in the width covered by the 10% isodose line at Dmax. At 12 MeV TCF(10) increases from 1.18 at 100 cm SSD to 1.38 at 115 cm. The TCF graphs clearly illustrate the diverging path of the 90% and 10% isodose lines as SSD is increased, and further illustrate the penumbra broadening which occurs at extended SSD.

The difference between TCF(10) and TCF(90) is most pronounced at the lower beam energies. At the higher beam energies of 16 and 20 MeV, the differences are smaller but the divergence of the trend lines for the two factors is still very apparent as the SSD is increased.

At the 16 and 20 MeV energies, extrapolation of the trend lines in TCF to SSDs below 100 cm reveals that all values of TCF converge as the SSD approaches a value slightly less than 95 cm. For the 2100C accelerator, the distance from the electron source to the end of the applicator is 94 cm. The convergence of TCF factors near this point for the higher beam energies implies that beam penumbra would shrink to virtually nothing were the applicator brought in contact with the phantom surface (giving an SSD of 94 cm). This is perhaps not surprising since the penumbra results largely from the effects of scatter at the edge of cutout. The scattering power of ostalloy is reduced significantly at higher beam energies. With no air gap to allow beam spreading, a step change in beam fluence from open to closed field would result.

3.4.5 Abutting photon and electron fields

The uniformity of the dose distribution which results from adding an electron field to photon fields depends critically on the nature of their respective penumbra profiles and will, therefore, depend on the SSD of the electron field. This is shown clearly in the graphs which display summed dose profiles for isocentric photon fields in combination with electron fields at 100 cm and 110 cm SSD. For the 9 and 12 MeV electron fields, dose uniformity in the junction region is significantly reduced on moving from 100 cm to 110 cm SSD. Uniformity is poor at extended SSD because the electron field's penumbra is much broader than that of the photon fields. There is a characteristic hot spot on the photon side of the junction due to scattered-in electrons and a corresponding cold spot on the electron side due to scattered-out electrons not being balanced by scattered-in photons.

An interesting reversal of this trend occurs at 16 MeV where the 110 cm SSD field produces the better summed profile. This may be attributed to the fact that, at 100 cm SSD, the 16 MeV electron field has a narrower penumbra than the photon fields. The expanded penumbra at 110 cm SSD provides a better match for the photon fields.

It should be noted that the optimum gap sizes shown in the results refer only to profiles at the D_{max} depth. Dose uniformity at greater depth may differ significantly from that shown at the D_{max} depth, particularly for the higher energy electron fields where the dose plateau extends far beyond the D_{max} depth. Unfortunately, the limitations of treatment planning computers in modelling electron penumbra at extended SSD (as discussed above) make a detailed assessment of the depth dose distribution in the plane normal to the junction region rather difficult. Johnson and Khan [55] measured 1-dimensional dose profiles resulting from abutting photons and 9 MeV electrons at standard and extended SSD and found similar patterns of hot and cold spots to those described in this work. Computer modelling with a commercial planning system of the 2-D distribution failed, however, to predict the extent of the hot and cold spots.

The preceding discussion should illustrate that the decision to use an abutting photon and electron treatment technique requires careful consideration. Treating with a gap any larger than the optimum size indicated here will lead to regions where the dose falls below 90%. This is unacceptable if the junction region is regarded as part of the clinical target volume. The hot spots of 120% dose resulting from the use the optimum gaps in matching photons with electron fields of energies 9 MeV (at 110 cm SSD) 16 MeV (at 100 cm SSD) are undesirable. These hot spots may be acceptable clinically, however, if they occur over a small volume of sub cutaneous tissue. This will be true of the 9 MeV field but not necessarily of the 16 MeV beam where the hot spot is likely to extend to greater depth. For 16 MeV electrons the optimum clinical technique may be to treat at extended SSD in order to achieve better penumbra matching at the junction.

Appendix A3.1

Dose response characteristics of measurement diode

6 MeV Beam Energy:

Measurement Depth = 1.5 cm water equivalent

Dark current corrected to zero

16 MeV Beam Energy:

Measurement Depth = 1.7 cm water equivalent

Dark current corrected to zero

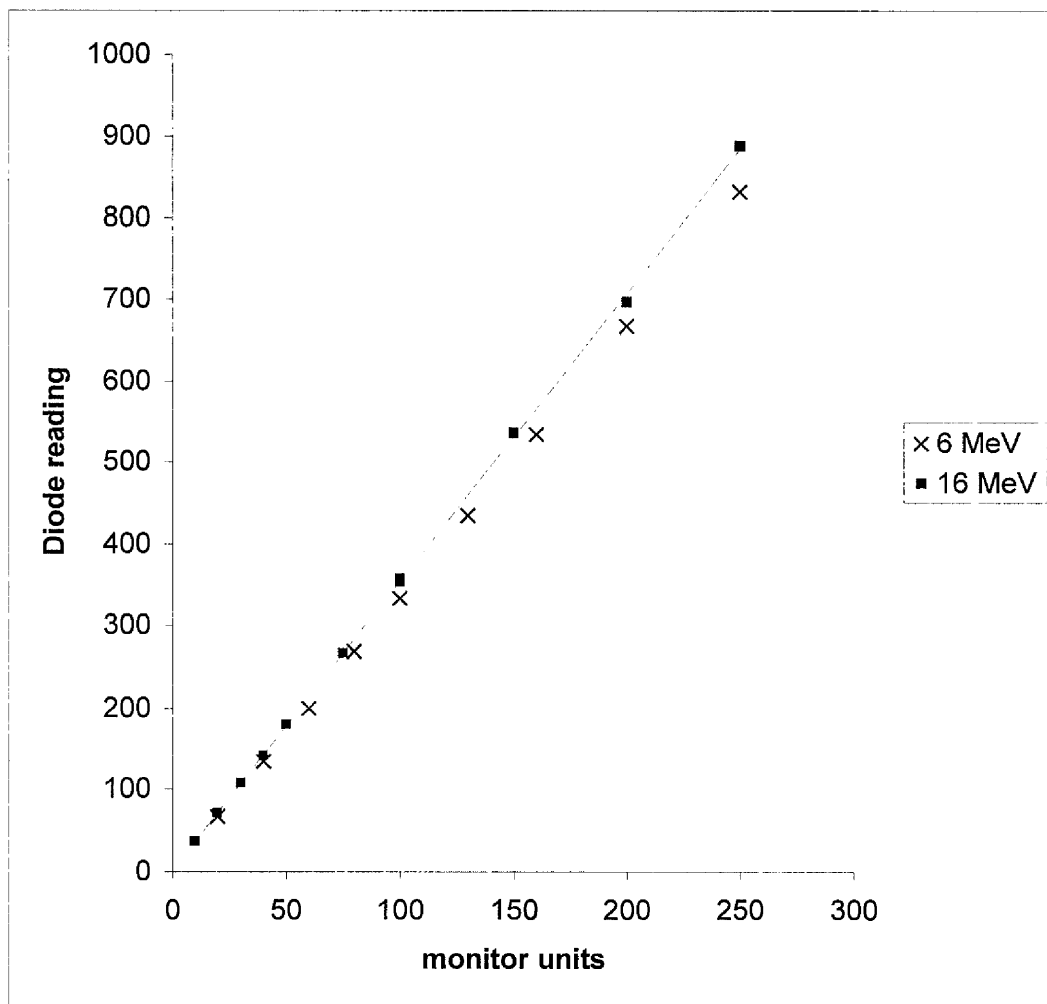


Figure A3.1. Dose response of P-type diode detector for 6 and 16 MeV electron fields.

CHAPTER 4

BEAM PROFILES WITH OSTALLOY CUTOUTS

4.1 Introduction

In the majority of therapeutic electron treatments, secondary collimation of the beam by means of an applicator arrangement is necessary to produce acceptable beam uniformity and to maximise electron fluence at the patient surface. Field shaping to reduce the dose to adjacent normal tissue is then often achieved by the addition of lead or low melting point alloy apertures, or cutouts, to the end of the applicator [56-58]. It has been noted [12] that the angular spread in electron momentum caused by multiple scattering at the accelerator head, applicator side walls and cutout leads to a gradual reduction in electron fluence in the region of the cut-out edge, giving rise to a characteristic penumbra.

Various workers have investigated the nature of the penumbral region by measuring or deriving dose profiles in phantoms resulting from electron fields used with secondary collimation [58,59]. Al-Ghazi *et al* [60] found that the penumbra width increases with energy but is virtually independent of field size. Sabbas *et al* [61] have modelled the characteristics of the penumbra based on the angular spread of electron moments at the collimators and contend that the width and position of the penumbra depends crucially on the electron energy and the design of the accelerator head, applicator and cutout.

In this study, the position of the 90% isodose line in relation to the cutout edge is examined for various cutout shapes. In selected cases an assessment of the 10% isodose line is also made, allowing penumbra width to be estimated. Among the cutout shapes investigated are the range of ellipses used to give electron boost fields to the resection scar area in patients who have undergone breast lumpectomy or wide local excision. The efficacy of electron boost techniques is well established [5, 62-64], though concern has been expressed over the accuracy and precision with which these treatments are prescribed [65,66]. As with any

external beam radiotherapy treatment it is advantageous for the clinician to prescribe a defined minimum dose to a defined region rather than define only the physical edges of a field shaping aperture [67]. This work has established the extent of the 90% dose region in a single plane perpendicular to the beam axis using film dosimetry and compared the results with calculated profiles from a Helax TMS planning computer.

TMS is able to accept detailed specifications of cutout geometry, entered in a beam's eye view. This data is then used to modify the energy fluence matrix which, in turn, is convolved with pre-calculated dose kernels to yield dose within the phantom under consideration [12]. The algorithm can, therefore, model cutouts of arbitrary shape.

A full assessment of the calculated penumbra requires comparison with measurements made in a plane perpendicular to the beam central axis. Film dosimetry has clear advantages in speed and ease of use over other methods when large 2-dimensional dose distributions require to be obtained. Moreover, its accuracy has been established by innumerable studies [31,48,68-70] which conclude that, under controlled conditions, the relationship between net recorded optical density and absorbed dose to the phantom (the sensitometric curve) is independent of electron energy and is generally one of direct proportionality.

This proportionality cannot be assumed for photons, however, due to the energy dependence of the photoelectric and Compton cross-sections for photon interactions in the film [71,72]. Any electron beam which interacts with metallic objects such as the primary collimators, applicator side walls or alloy cutout will inevitably give rise to bremsstrahlung radiation [73,74] which, in turn, contributes to the total absorbed dose received by objects in the beam. It is likely that proportionally greater dose is contributed by bremsstrahlung near the applicator and cutout side walls [75] and therefore the optical density recorded by film in this region cannot be assumed to be directly proportional to absorbed dose.

4.2 Materials and Methods

4.2.1 Field set-up

Isodose profiles were produced for a plain 10 x 10 cm ostalloy cutout together with the range of elliptical cutouts currently regarded as having maximum clinical utility for breast boost treatments.

Exposures were made with a Clinac 2100C linear accelerator (Varian Associates, as before). An applied dose of approximately 45 cGy to the point of maximum central axis dose was used for all exposures. The applicator accepts field defining cutouts constructed of low melting point ostalloy which, in the Beatson Oncology Centre, have a thickness of 11 mm irrespective of the electron energy in use. Both plain and elliptical cutouts were housed in a 10 x 10 cm applicator designed such that the distance from the physical electron source to the mid depth of the cutout was 94.0cm. An interlock prevents operation of the accelerator unless a cutout is in place, and so plain 10 x 10 cm inserts must still be used to achieve this field size.

Dose profiles were recored by placing film in a TEMEX [76] water-equivalent solid phantom in a plane perpendicular to the beam central axis. For all exposures, the distance of the electron source to the phantom surface (SSD) was 100 cm. Films were placed at or near the depth of dose maximum. In all cases, Kodak XV2 therapy verification film was used (Eastman Kodak Company, Rochester, New York 14650, USA). This film has a linear sensitometric curve over the range of absorbed dose considered here [48]. All films were from the same batch and were processed under similar conditions in an automatic film processor.

4.2.2 Corrections to the measurements

Films were read with a transmission scanning densitometer capable of recording optical density along 1-dimensional tracks across the film. The scanner was capable of resolving areas of raised or lowered optical density with diameters of 1mm or greater. Measurements of absorbed dose using this film and densitometer combination were found to be reproducible and of sufficient precision to record single monitor unit increments (see appendix A4.1.).

The difficulties associated with the bremsstrahlung contribution to optical density near the cutout edges were overcome by comparing films with diode measurements for a plain 10 x 10 cm cutout. Diode measurements were made in a water phantom using a p-type detector interfaced to a Therados DPD5 electrometer (Therados AB, Dalgatan 15, Uppsala, Sweden). Measurement depths at each beam energy were chosen to correspond to those used for film measurements. The measurement axis was in the plane of rotation of the accelerator gantry and perpendicular to the beam central axis (this corresponds to the direction of the collimator X axis when collimator angle 0° is set). The distance from the field centre to the point receiving 90% of the absorbed dose to the central axis was noted for the plain cutout at each available energy. Returning to the films, optical density was now measured at the corresponding X axis displacement from the field centre on the film and this optical density, labelled OD_{90} , was henceforth assumed to correspond to 90% of the central axis dose wherever it occurred on the film. A similar methodology was applied to obtain the position of regions corresponding to 10% of central axis dose.

The equivalent squares of the six breast boost cutouts examined in this work were all within the range 6.0 – 7.3. As long as the applicator size and design remain fixed, outputs (in monitor units per Gy) for electron fields show very little variation over this range of equivalent square. Provided, therefore, the same number of monitor units are applied to the breast boost cutouts, OD_{90} can be regarded as

representing 90% of the central axis dose at the same depth for the breast boost cutouts.

Isodose profiles were also generated by a HELAX TMS planning computer. Profiles were calculated for plain and breast boost cutouts for beams incident on a homogeneous water-equivalent phantom. Dose calculation was to a matrix of points separated by 2.5mm.

4.3 Results

4.3.1 The 10 x 10 cm cutout

Table 4.1 gives two X axis displacements, X_{90} and X_{10} . These are the mean distances from the central axis at which, respectively, 90% and 10% of the central axis dose occur for the 10 x 10 cm cutout. For each beam energy, measurements were made at a single depth with a diode in a water phantom. Measurement depths were chosen to coincide with the depth of dose maximum rounded to the nearest 5mm (the maximum depth increment available with the phantom in use). The optical densities, OD_{90} and OD_{10} , at the same X axis locations on the film were recorded and, as discussed above, used as the basis for measuring the position of 90% and 10% dose on films. Table 4.2 shows the mean distance from the field centre on the film to the OD_{90} level for the axis perpendicular to both the plane of rotation of the accelerator gantry and the beam central axis (corresponding to the collimator Y axis and labelled 0°) and for axes at 45° and 315° to the Y axis. Also shown are distances to 90% dose calculated by TMS. Table 4.3 gives the same distances for 10% dose.

| Energy (MeV) | Depth (mm) | X_{90} (mm) | | X_{10} (mm) | |
|-----------------|------------|-----------------|--|-----------------|--|
| | | 10x10 cm cutout | | 10x10 cm cutout | |
| 6 | 10 | 45 | | 58 | |
| 9 | 15 | 46 | | 58 | |
| 12 | 20 | 46 | | 58 | |
| 16 | 15 | 47.5 | | 55 | |
| 20 | 15 | 47.5 | | 56 | |

Table 4.1. Diode measurements in a plane perpendicular to the field central axis for an electron beam defined by a 10 x 10 cm square cutout. Distances are those from the field centre to the 90% and 10% dose levels

| Energy (MeV) | Depth (mm) | Axis distance to 90% (film) | | | Axis distance to 90% (TMS) | | |
|-----------------|---------------|-----------------------------|------|------|----------------------------|-----|------|
| | | 10x10 cm cutout (mm) | | | 10x10 cm cutout (mm) | | |
| | | 0° | 45° | 315° | 0° | 45° | 315° |
| 6 | 10 | 45 | 61 | 60 | 45 | 61 | 61 |
| 9 | 15 | 46.5 | 61 | 62 | 45 | 61 | 61 |
| 12 | 20 | 46.5 | 62 | 62.5 | 45 | 61 | 61 |
| 16 | 15 | 47 | 64.5 | 65 | 47 | 66 | 66 |
| 20 | 15 | 48 | 66 | 67 | 47.5 | 66 | 66 |

Table 4.2. Film measurements and TMS calculations of the 90% dose level for an electron beam defined by a 10 x 10 cm square cutout. Angles denote the angle of a line projecting from the field centre to the edge of the cutout in a plane perpendicular to the beam central axis.

| Energy (MeV) | Depth (mm) | Axis distance to 10% (film) | | | Axis distance to 10% (TMS) | | |
|-----------------|---------------|-----------------------------|------|------|----------------------------|-------------------------|----|
| | | 10x10 cm cutout (mm) | 0° | 45° | 315° | 10x10 cm cutout (mm) | 0° |
| 6 | 10 | 58 | 77 | 77.5 | 55 | 74 | 74 |
| 9 | 15 | 58.5 | 75 | 76 | 56 | 74 | 74 |
| 12 | 20 | 58.5 | 76.5 | 78 | 57 | 75 | 75 |
| 16 | 15 | 55.5 | 74 | 75 | 54 | 73 | 73 |
| 20 | 15 | 57 | 75 | 76 | 54 | 74 | 74 |

Table 4.3. Film measurements and TMS calculations of the 10% dose level for an electron beam defined by a 10 x 10 cm square cutout. Angles denote the angle of a line projecting from the field centre to the edge of the cutout in a plane perpendicular to the beam central axis.

Figure 4.1 illustrates the data shown in tables 4.2 and 4.3 for 6 MeV and 20 MeV fields. The calculated 90% and 10% isodose profiles are shown together with those points at which 90% and 10% dose were measured.

Defining beam penumbra width on the y-axis as the distance between the 10% and 90% isodose lines allows an estimation of this quantity to be made using the 0° data in tables 4.2 and 4.3. Penumbra widths are shown in figure 4.2.

4.3.2 Non linear film response

As an illustration of the non-linear nature of the film response near the cutout edge, a comparison of the recorded optical density at the beam central axis, OD_{CA} , with OD_{90} (the optical density at the position of 90% dose recorded by diode measurement) is shown for the 10 x 10 cm cutout in figure 4.3. Optical densities have been corrected for film background fogging.

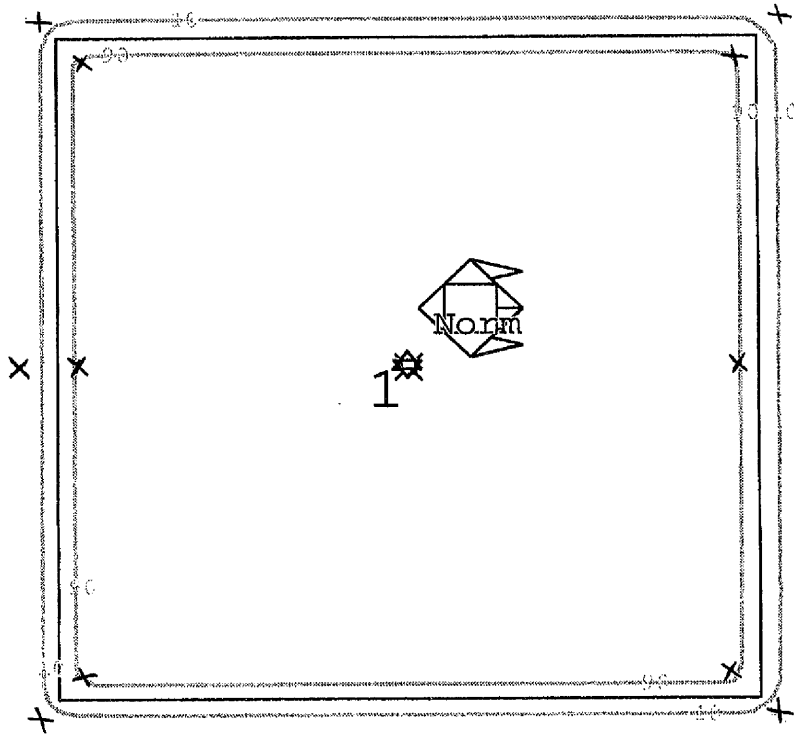
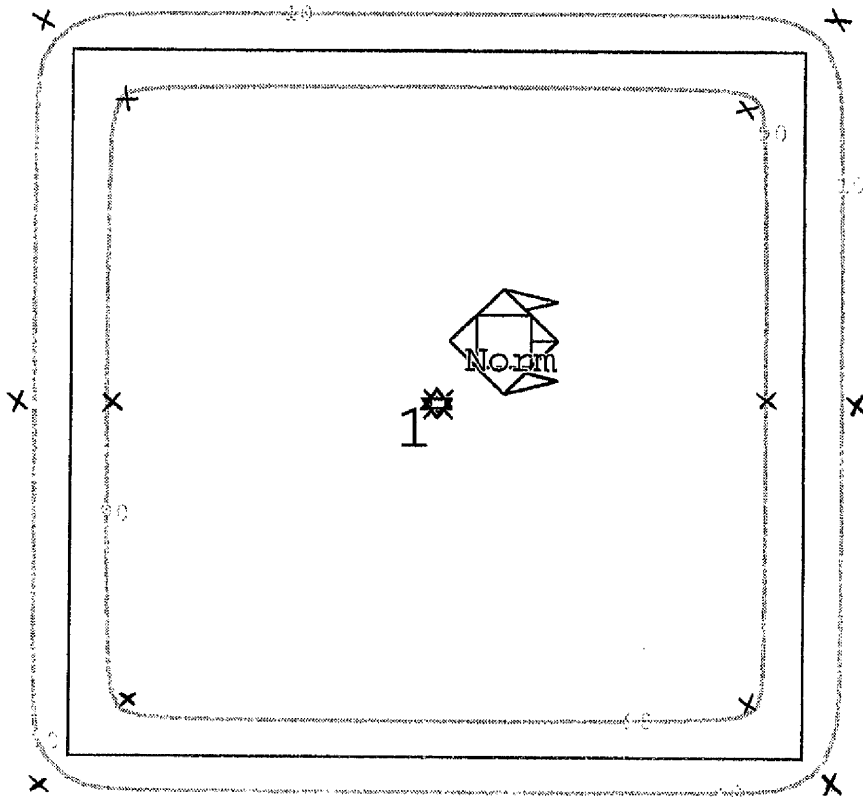


Figure 4.1. Comparison of TMS calculation (solid lines) and measured doses (crosses) for 16 MeV (above) and 6 MeV (below) electron beams. Doses are displayed at the Dmax depth in a plane perpendicular to the beam central axis for a 10 x 10 cm field.



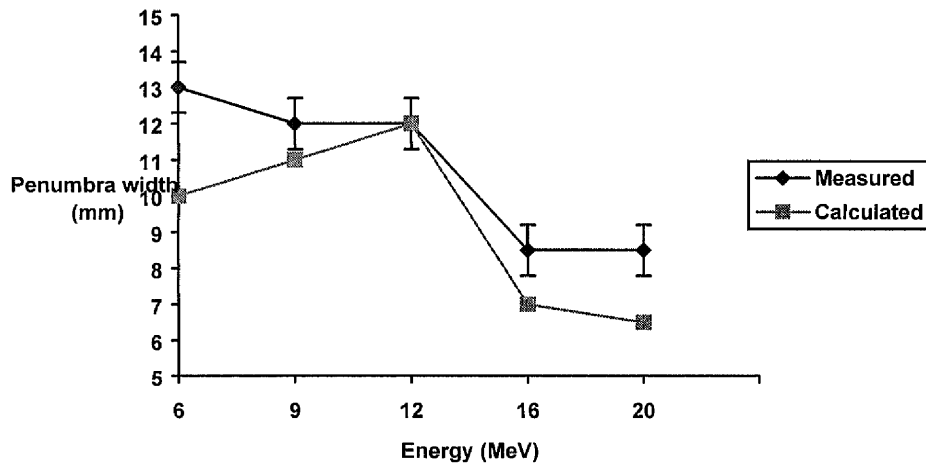


Figure 4.2. Measured and calculated penumbra widths at the Dmax depth for a 10 x 10 cm electron beam.

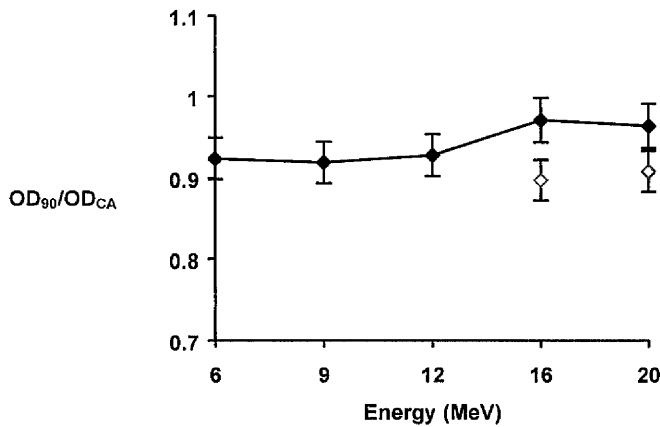


Figure 4.3. Ratio of the film optical density at the position of 90% absorbed dose (OD_{90}) to that on the central axis (10 x 10 cm cutout). Measurements made with electron beams defined by 10 x 10 cm square ostalloy cutouts of two different thicknesses: solid dots - 11mm thickness; hollow dots - 22mm.

A film responding linearly to absorbed dose would produce a value of exactly 0.9 for the ratio of OD_{90} to central axis optical density. For the 10 x 10 cm cutout irradiated under standard conditions, the ratio shown in figure 4.3 lies consistently above 0.9. At electron energies up to and including 12 MeV the measured ratio

lies just within the experimental uncertainty ($\pm 2.5\%$) of 0.9, while at 16 and 20 MeV it is outwith this, indicating a systematic difference in the measurements of film and diode. As discussed above, one possible cause of this is a non-linear film response to bremsstrahlung radiation produced during electron transmission through the cutout. To test this hypothesis, exposures at 16 and 20 MeV were repeated with a double thickness (22mm) of ostalloy used to define the field edge. The reduced electron transmission resulting from the extra ostalloy should lead to reduced bremsstrahlung production. As illustrated in figure 4.3, the ratio of OD_{90} to central axis optical density is indeed reduced to within the experimental uncertainty of 0.9 in this case.

4.3.3 Breast Boost Cutouts

There are six standard breast boost cutouts (BB1 - BB6) in current clinical use at the Beatson Oncology Centre. For each cutout, exposures were made at all five available energies with the same monitor unit reading (and therefore total electron fluence) as that applied to the 10 x 10 cm plain cutout. Measurements were made at the same (energy-dependent) depths used for the plain cutouts. For brevity, only those results relating to breast boost cutout number four (BB4) are shown. Figure 4.4 shows two exposures of BB4 at electron energies 6 and 20 MeV.

The suitability of using the previous value of OD_{90} (i.e. the optical density at the position of 90% dose for a 10 x 10 cm field) for the breast boost cutouts was confirmed by diode measurements of relative absorbed dose in a water phantom made along the 270° degree axis of BB5. This axis intersects the region of maximum curvature on BB5 which is the most eccentric of the breast boost ellipses. The measured position of 90% dose was compared with that position on the film predicted to correspond to 90% dose using the value of OD_{90} obtained previously. For both energies, the discrepancy between the diode and film predictions of the 90% dose position was less than 1mm. Existing values of OD_{90} were, therefore, used to predict 90% dose for subsequent film measurements of the breast boost cutouts.

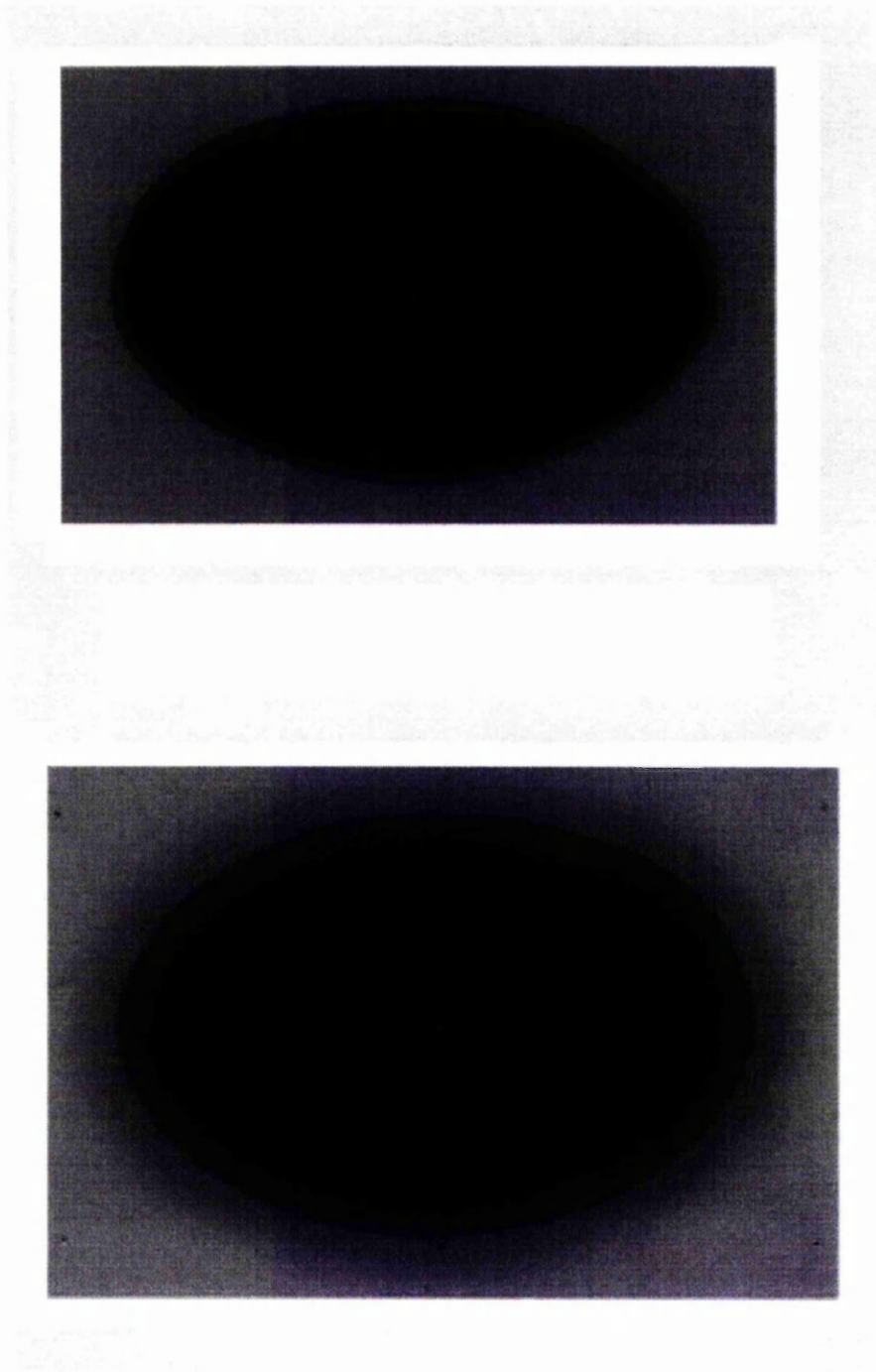


Figure 4.4. Film exposures of Breast Boost Cutout 4 exposed to 16 MeV (top) and 6 MeV electron beams. The projection at 100 cm SSD of the major and minor axes of the physical ostalloy measures 10.2 cm x 6.5 cm.

For each cutout, optical density measurements were made on 4 axes: the collimator X and Y axes and 2 further axes at 65° and 115° to the Y axis in the case of breast boost cutout number 1 and at 60° and 120° to the Y axis for all other breast boost cutouts.

The axis orientations for BB2 - BB6 are shown schematically in figure 4.5. Using the known value of optical density corresponding to 90% dose (OD_{90}), the distance along each axis at which the dose falls to 90% was now determined. In this way, eight points at which the absorbed dose falls to 90% of the maximum dose can be identified for each cutout at each energy.

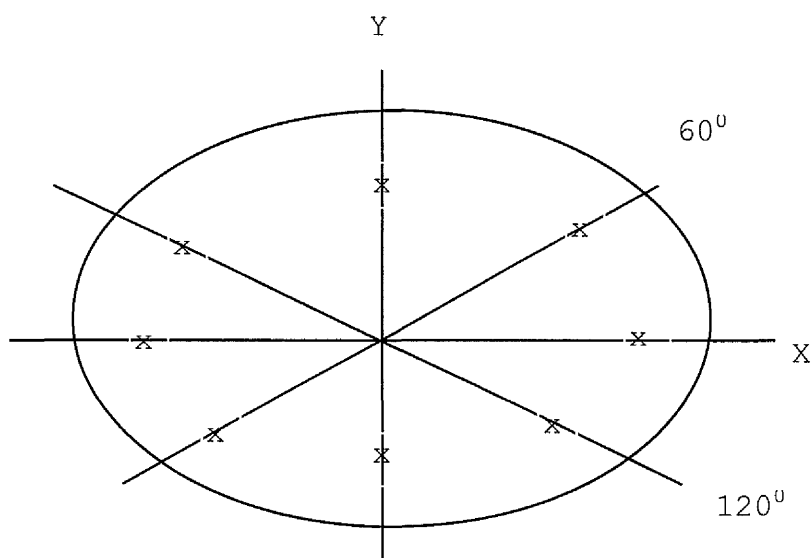


Figure 4.5. Schematic diagram showing axes for optical density measurements in breast boost cutouts (BB2 - BB6). "x" indicates a typical location for 90% dose.

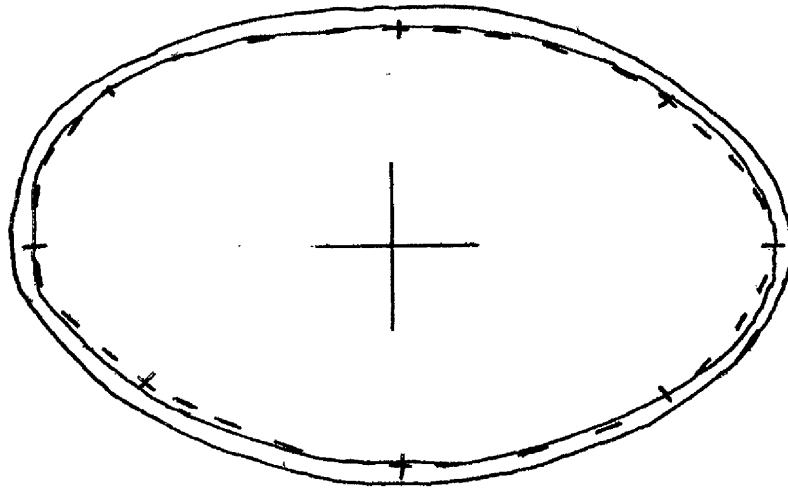


Figure 4.6. Projection of Breast Boost Cutout 4 in a plane perpendicular to the beam central axis for 16 MeV (above) and 6 MeV (below) electron beams. Within the cutout edge, two isodose lines are shown corresponding to 90% dose. Dotted isodose line - measured data, solid isodose line – TMS calculation.

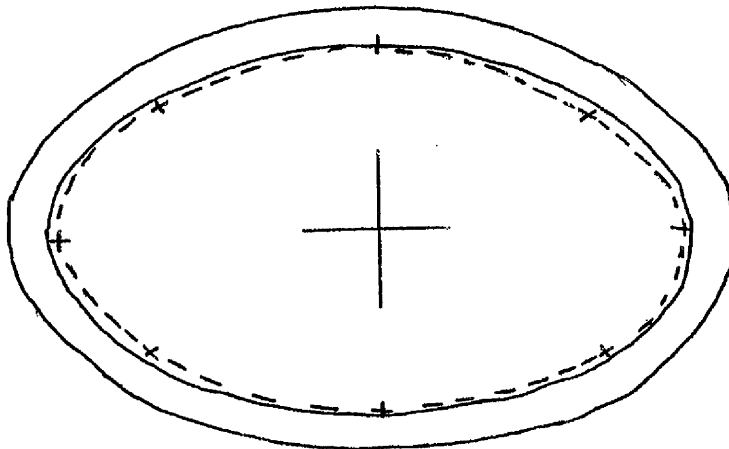


Figure 4.6 depicts a projection of the inside ostalloy edge of BB4 as it appears at 100cm SSD viewed with a diverging light field originating optically at the physical electron source. Also shown are the eight measured points corresponding to 90% of maximum dose and an interpolated 90% isodose line for electron energies 6 and 16 MeV. Measured data corresponds to depths below the phantom surface of 10mm and 15mm for 6 MeV and 16 MeV respectively. The TMS-generated 90% isodose line is also shown.

4.4 Discussion

This work has compared 2-dimensional dose profiles in the penumbra region of electron fields obtained by two methods: quantitative film dosimetry and the calculation algorithm of the HELAX TMS planning computer. Isodose profiles corresponding to 90% and 10% of central axis dose have been obtained for planes perpendicular to the beam central axis. Beam shaping apertures considered include 10 x 10 cm plain cutouts and a series of ellipses of varying eccentricity.

4.4.1. The effect of bremsstrahlung on film response.

The results clearly demonstrate the value of comparing film measurements in the penumbra region with data measured by diode. Evidence of a non-linear film response in the penumbra region is found in the comparison of OD_{90} (the film optical density at the position predicted by diode measurement to correspond to 90% dose in the penumbra) with central axis optical density. The ratio of these measurements would always be 0.9 for a film responding linearly to absorbed dose. At each beam energy, however, the ratio is above 0.9 when calculated for the 10 x 10 cm cutout. At beam energies of 16 and 20 MeV the discrepancy is larger than the estimated uncertainty of the film measurements, indicating a systematic difference in the film and diode measurements of relative dose in the penumbra region.

As discussed above, the likely cause for this increased film sensitivity in the penumbra is the contribution to absorbed dose made by low energy bremsstrahlung originating at the cutout and applicator. The transmission factor for 12 MeV electrons traversing 11mm of ostalloy is less than 5% [27]. For 20 MeV electrons the figure rises to approximately 10%. There are, therefore, far more electron interactions at the downstream edge of the cutout when this is used to define the higher energy beams. Increased production of low energy bremsstrahlung in this region of the cutout for high energy beams is also, therefore, more likely. This may well provide an explanation of the increase in non-linearity of the film response for 16 and 20 MeV beams. The non-linearity at 16 and 20 MeV is reduced if the thickness of ostalloy is increased to 22mm, for which the transmission factor is less than 5% for all beam energies.

4.4.2 Measurement and calculation uncertainties

Both the measured and calculated data are subject to factors which limit their accuracy. There are several uncertainties relating to the measured data: (1) the accuracy with which the film is positioned in relation to the densitometer, (2) the degree to which film sensitivity is reproducible, (3) densitometer resolution and (4) accelerator stability.

Films required to be scanned by the densitometer along axes of pre-defined angle with respect to the collimator y-axis. During optical density measurements, the maximum deviation from the correct scan orientation was estimated to be 0.5° which, for a flat-sided cutout, corresponds to an axis displacement of ± 0.2 mm. An error of this magnitude is sufficiently small to be disregarded.

The film used was Kodak XV2 verification film. For electron interactions, this film has a linear relation between optical density and absorbed dose for values of the latter used in this work [48]. As this work compares optical density at a pre-determined location on one film exposed to a 10 x 10 cm field with that found on other films exposed separately, it is necessary to consider variations in film

sensitivity to define measurement accuracy. It has been noted [68] that intra- and inter-film variations in sensitivity are likely to be no greater than $\pm 1\%$ and $\pm 1.5\%$ respectively. The scanning densitometer used to read the films was capable of resolving single monitor unit increments in absorbed dose which, in this case, corresponds to approximately 2% of absorbed dose. It is thus reasonable to assume that random uncertainties in its sensitivity are no greater than $\pm 1.0\%$. Accelerator stability is monitored daily and does not exceed $\pm 1.0\%$.

Taken cumulatively these errors result in an uncertainty in dose measurements of approximately $\pm 2.5\%$. In regions of steep dose gradient the resulting uncertainty in isodose position is no more than ± 0.5 mm. Adding this to the ± 0.5 mm intrinsic spatial resolution of the densitometer results in a total uncertainty in penumbral isodose position of no more than ± 1.0 mm.

The precision of the calculated data depends on (1) the resolution of the calculation grid (2.5 mm) and (2) the number and spacing of the pencil beams used by the calculation algorithm. Calculation accuracy depends on the detail with which electron transport and scatter processes within and upstream of the phantom are modelled. Of particular relevance for cutout penumbras at shallow depth is the modelling of electron scatter in the applicator and at the edges of the cutout. These phenomena are machine-specific and therefore it is important to recognise that errors in absorbed dose calculations due to limitations in the algorithm are also machine-specific.

4.4.3 Discrepancies between the measured and calculated data

For the majority of cutout geometries there is good agreement between TMS and the measured data in the position of the 90% isodose line. The displacement of the calculated from the measured 90% line showed deviations of no more than 1.0 mm for the elliptical cutouts at all energies between 6 and 20 MeV. For the 10 x 10 cm plain cutout, positional deviations in the 90% isodose line were 1.5 mm or less where the square side of the cutout intersects the X and Y axes. The same

maximum positional deviation was observed at the right-angled corners of the cutout. Calculated positions of the 90% isodose line, therefore, lay within the range of error of the measured data for all cutout geometries.

Deviations in the 10% isodose line for the 10 x 10 cm square cutout were slightly higher for all energies. TMS underestimates the displacement of the 10% isodose line from the beam central axis on all the profile axes considered at all energies. The mean discrepancy is 2mm and is as large as 3.5mm for the 315° corner of the cutout with a 6 MeV beam energy. As with the 90% isodose line, calculation accuracy shows no significant dependence either on beam energy or on location in the cutout.

ICRU report 42 [23] states that a computed dose distribution may be considered accurate if the calculated position of an isodose line lies within 2 mm of its actual position. The inaccuracy in the calculated position of the 10% line is, therefore, notable. Blomquist [19] reported similar findings and offered an explanation for the discrepancy by referring to the contribution to dose made by scattered electrons from the applicator and cutout. The influence of this scatter on beam penumbra has been previously described [29] and is often modelled using a virtual SSD which varies with beam size and energy. TMS uses a combination of measured full width at half maximum data and a r.m.s. scattering angle supplied by the user at commissioning to define penumbra position and width respectively. There is no explicit modelling of applicator and cutout scatter. The user-supplied parameters are optimised for the positions of the 90% and 50% isodose lines, and so the calculated position of the 10% isodose line is prone to greater error.

As well as scattered electrons, it has been suggested [78] that leakage of primary radiation through the applicator walls contributes significantly to absorbed dose at depths up to the depth of dose maximum in the extreme periphery of the beam. This leakage is not modelled by TMS. Underestimation of the displacement of the 10% isodose line from the beam central axis (as found here) is consistent with the algorithm's failure to include the contribution made by leakage radiation.

The measured and calculated data show a similar energy dependence in the distance from the cutout edge to the 90% isodose for the 10 x10 cm and elliptical cutouts. Energy dependence is also apparent in the position of the 10% isodose line and in the distance between the 10% and 90% isodose lines (the penumbra width). Measured penumbra width for the 10 cm cutout varies from 13 mm for the 6MeV beam to 8.5 mm for the 20 MeV beam. Calculated penumbra width varies from 10 mm (6 MeV) to 6.5 mm (20 MeV). The discrepancy between measured and calculated penumbra width is due almost entirely to the discrepancy in the 10% isodose line. Both the measured and calculated data show penumbra width remaining approximately constant for beam energies between 6 and 12 MeV (inclusive). There is then an abrupt decrease in width at 16 MeV, the 20 MeV field maintaining this reduced value.

The energy dependence of beam penumbra width has its origins in multiple scattering theory [31]. As discussed above, electron scatter prior to the intersection with the phantom is characterised by means of a r.m.s. scattering angle. This parameter then determines the spread of the pencil beams used by TMS to assess dose at depth in the penumbra. The calculations, though giving rise to some inaccuracy in the 10% isodose line, have adequately reproduced the pattern of energy dependence in beam penumbra width.

Appendix A4.1

Dose response of the measurement film

Figure A4.1 (below) illustrates the sensitivity and reproducibility of the measurements made with Kodak XV2 verification film. Optical density at the field centre of a 60 x 60 mm cutout was recorded for a series of 6 MeV fields. Applied dose was increased by 2 cGy for each successive field.

Also shown is the best straight line fit for the measured data

Slope = 2.28 ± 0.05 cGy/vertical scale division.

Intercept = 35.2 ± 2 vertical scale divisions.

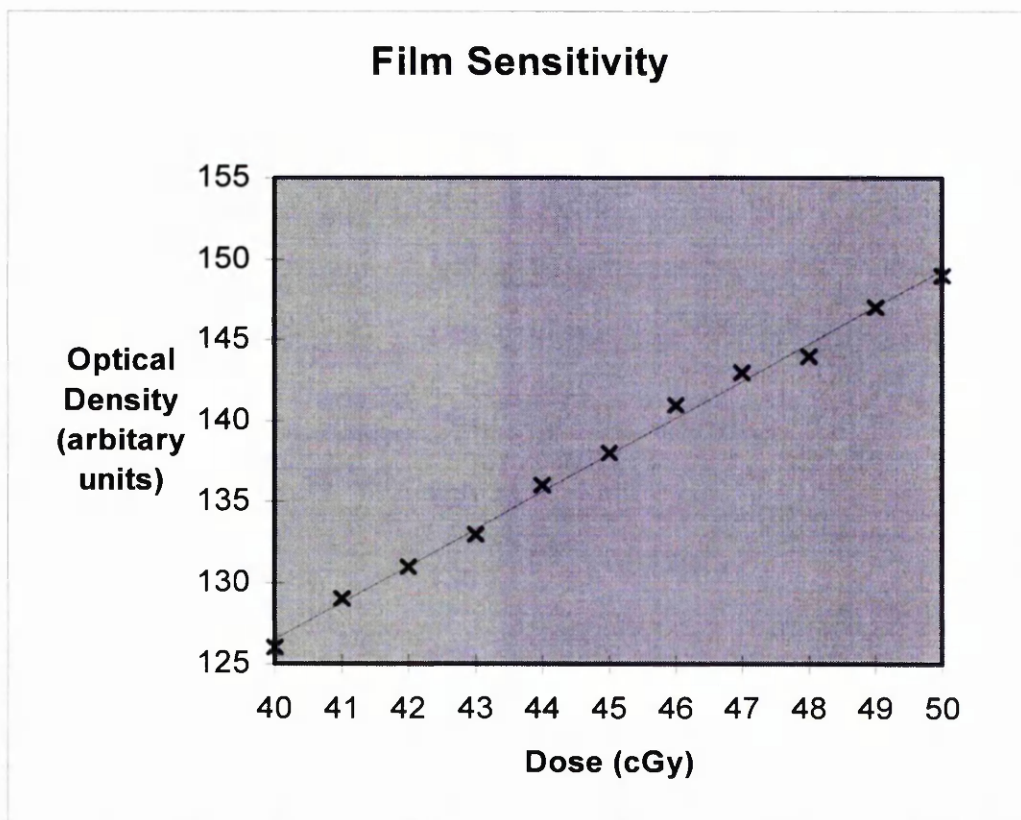


Figure A4.1. Variation of optical density with applied monitor units for Kodak XV2 verification film. Film was exposed to a 6 MeV 6 x 6 cm field in a TEMEX phantom.

CHAPTER 5

CALCULATION OF ABSOLUTE DOSE

5.1 Introduction

An adequate description of a radiotherapy treatment usually requires the treatment plan to contain a description of the relative dose distribution. More fundamentally, the plan must always contain a statement relating the measurement of radiation by the treatment unit's ionisation chamber (in monitor units) to the absolute dose (in cGy) at a specified point in the patient. For most single field treatments, whether given with electrons or photons, this point is chosen as the depth of dose maximum on the beam central axis (the D_{\max} point). This point usually coincides with the centre of the treatment area and avoids regions of steep dose gradient. Confirmation of the suitability of this point for dose prescription is provided by the ICRU in report number 50 [67].

Most treatment planning systems allow the user to move the dose prescription point away from the D_{\max} point if necessary, and hence require the point to be chosen explicitly. It is then referred to as the *normalisation* point. For a single field treatment, the number of monitor units required to give a dose of 100 cGy to the normalisation point is referred to as the *output* of the field. Thus, in any given situation in which an electron field is incident on a patient or phantom, specification of the output (from the treatment plan) and the intended prescription dose (from the clinician) is sufficient to calculate the required monitor units.

Traditionally, treatment planning systems have calculated output by referring to a look-up table of measured values [79,80]. When the field being modelled falls within the scope of the look-up table, this method has the advantage of providing an output value with a certain known accuracy. The disadvantage of this system is that it requires the user to perform many time-consuming dosimetry measurements. An alternative approach is to supply the planning system with a limited set of reference measurements and use a beam modelling algorithm to calculate the output for a given field in relation to the reference measurements. As well as

requiring fewer measurements, this method has the flexibility to calculate outputs for non-standard conditions such as irregularly shaped fields.

The two treatment planning systems under consideration here adopt differing approaches to the calculation of output. The Cadplan system depends largely on measurements while Helax TMS makes use of both measured and calculated data. The formalism behind this latter, more complex, method may be applied to both electron and photon fields, and has been discussed at length [81,82]. An assessment of the accuracy of the Cadplan and TMS monitor unit calculations provides a comparison of two different methodologies. For Cadplan the accuracy of the final monitor unit value depends on the accuracy of the data in the look-up table and the way in which the system arrives at a choice of look-up data. The accuracy of the TMS monitor unit calculation depends on the completeness of the theoretical formalism in use, as well as the accuracy of the initial measurement set incorporated therein.

In this work, output values predicted by the treatment planning systems were assessed by comparison with measurements made with an ion chamber in a water phantom. The inclusion of more complex phantom geometries for certain comparisons required associated output measurements to be made with thermoluminescent dosimeters. These were calibrated by comparison with ion chamber measurements. While introducing an additional element of uncertainty, the use of TLD in absolute dose determination is well-established [31,83].

5.2 Materials and Methods

5.2.1 Field set-up and phantom geometry

The accuracy of monitor unit calculations performed by the treatment planning computers was assessed for a variety of beam shapes, phantom geometries and source-skin distances (SSDs). Dose calculations were performed using Helax TMS v4.1A and Varian Cadplan v3.1.1. Exposures were made with a Varian 2100C linear accelerator (Varian Associates, as before) at beam energies in the

range 6 to 20 MeV. Table 1 provides a summary of the four basic experiments carried out. Experiments 1 and 2 examined the variation in output with SSD and field cutout size respectively. Experiments 3 and 4 reproduced two situations first discussed in chapter 2: a beam incident on a plane phantom at an angle of 30° , and a beam incident normally on a phantom containing a tapered bolus edge. The four experiments are discussed in detail below.

1. *Extended SSD.* As discussed in chapter 3, electron treatments of the head and neck often require the use of SSDs greater than 100 cm in order to provide clearance between the patient's shoulder and the treatment applicator. The accuracy of monitor unit calculations for 10 x 10 cm and 5 x 5 cm fields was assessed for the SSD range: 100 cm – 120 cm. SSDs greater than 110 cm are rarely used in clinical practice, but an examination of the output calculation at SSDs of up to 120 cm provided useful information on trends in the relation between output and SSD.

Five beam energies in the range 6 – 20 MeV were considered for the 10 x 10 cm field. For the 5 x 5 cm field, only those beam energies at the upper and lower limits of the range in common clinical use were considered i.e. 6 MeV and 16 MeV. Measurements were made in a mini water phantom supplied by QADOS Ltd. This device can be adapted to house a variety of parallel plate chambers for electron dosimetry. The internal dimensions of 29.5 x 35 x 29.5 cm provide a large enough margin to ensure equilibrium of scatter into the central axis for the field sizes and beam energies considered in this work [34].

Both planning systems use the concept of a virtual source to model the effects that scatter in the machine head have on the output at extended SSD. The virtual source concept is used widely in electron dosimetry, and has been discussed at length in the literature [37,47]. Scattering events in the applicator cause an increase in the mean scattering angle of electrons. This, in turn, causes the beam to spread out more rapidly beyond the applicator than a simple inverse square expansion would indicate. The beam thus appears to originate from a virtual source situated downstream of the physical source. A reduction in beam fluence

results from the increased beam area beyond the applicator, and hence the required output is greater than would be required for a beam exhibiting inverse square behaviour. The distance from the physical to the virtual source position, Z_{virtual} , is that distance which allows the output at extended SSD, OP_{SSD} , to be described by an inverse square law of the form

$$OP_{\text{SSD}} = OP_{\text{standard}} * (SSD - Z_{\text{virtual}} + D_{\text{max}})^2 / (SSD_{\text{standard}} - Z_{\text{virtual}} + D_{\text{max}})^2 \quad (1)$$

where OP_{standard} is the output at the standard source skin distance, SSD_{standard} . By substituting a measured or calculated value of OP_{SSD} in equation (1), and then re-arranging the terms, the implied location of the virtual source can be calculated. This method was employed to calculate the value of Z_{virtual} implied by both the measured and computed outputs.

2. *Field size.* The use of ostalloy cutouts to define field sizes smaller than the plain applicator was discussed in chapter 4. A 10 x 10 cm applicator was fitted with a series of field-defining cutouts of successively smaller square side. The smallest field aperture considered was 3 x 3 cm. Fields smaller than this do not achieve scatter equilibrium on the central axis and are rarely used clinically due to the resulting unfavourable depth dose distribution.

3. *Oblique incidence.* The relative isodose distribution for this field arrangement was considered in chapter 2. To complement this, the experimental set-up was reproduced, and an assessment made of the monitor unit calculation. As before, an obliquely incident field intersects a WTe solid water phantom at an angle of 30° to the vertical, at a SSD of 102 cm. Comparison of measured and calculated output was performed at a point 2.7 cm along the beam central axis. This point was chosen to correspond with the D_{max} point for 12 MeV electrons. It was used as the normalisation point for the relative dose distribution shown in figures 2.8 and 2.9 on pages 17 and 18.

4. *Bolus Edge.* As with the oblique incidence experiment, the relative dose distribution for the bolus phantom was considered in chapter 2. The Bolus

phantom consists of a WTe solid water foundation overlaid with a PMMA block with an edge tapering at 45° (see figure 2.1 (4), page 13). To coincide with a region of reasonable dose homogeneity, the relative dose distribution was normalised to a point 7.0 cm distant from the beam central axis at a depth of 2.7 cm. This point was chosen for the assessment of output.

5.2.2 Measurement devices

Output measurements for experiments 1 and 2 were made with an ion chamber in a water phantom. This is universally recognised as the most accurate method of measuring absorbed dose per monitor unit [34,84,85]. For experiment 1, and for field sizes greater than 4 cm x 4 cm in experiment 2, measurements were made with a Roos 34001 parallel plate chamber (Gothic Crellon Ltd, 3 The Business Centre, Molly Millars Lane, Wokingham RG11 2EY). The chamber was interfaced to a NE 2570 / 1 electrometer (NE Technology Ltd, Bath Road, Beenham, Reading, Berkshire RG7 5PR). The Roos chamber has a relatively large cross-section with a collecting electrode diameter of 16 mm. For field sizes of 4 cm x 4 cm or less, measurements were made with the smaller NACP chamber (QADOS Ltd, as before). This device has a collecting electrode diameter of 10 mm and avoids the possibility of the field penumbra infringing on the chamber's

| Experiment | SSD (cm) | Energy (MeV) | Field Size (cm) | Measurement Point | Phantom Material | Measurement Technique |
|-----------------------------|-------------|-----------------|-----------------------|---|---------------------|--------------------------|
| 1. Extended SSD | 100 – 120 | 6 – 20 | 10 x 10, 5 x 5 | D_{max} | Water | Ion chamber |
| 2. Field size. | 100 | 6, 16 | Variable | D_{max} | Water | Ion chamber |
| 3. Oblique incidence | 102 | 12 | 19 x 19 | D_{max} distance along central axis | WTe solid water | TLD |
| 4. 45° bolus edge | 100 | 12 | 19 x 19 | 7 cm lateral, depth = D_{max} | WTe solid water | TLD |

Table 5.1. Summary of experiments undertaken to compare monitor units measured in four situations with those calculated by the Helax TMS and Cadplan planning computers.

active volume.

Measurements with the Roos chamber were carried out according to the IPEMB 1996 code of practice [8], currently recommended for electron dosimetry in the UK. Appendix A5.1 contains an example of the calculations required to convert measurements made with the Roos chamber from ionisation to absorbed dose. A description of the environmental and chamber related correction factors involved in the calculation is also given.

The NACP chamber was calibrated against the Roos chamber. This was achieved by comparing ionisation recorded by the NACP chamber with absorbed dose measured by the Roos chamber. Immediately prior to its use in assessing the 3 x 3 cm and 4 x 4 cm fields, the NACP chamber was used to record ionisation at the D_{\max} point for a 10 x 10 cm field in the water phantom. Both 6 and 16 MeV fields were considered. The chamber was then replaced with the Roos model, and this chamber used to measure absorbed dose for the same field size, energies and monitor units. The ratio of absorbed dose (Roos) to ionisation (NACP) was then calculated. Subsequent measurements of ionisation made with the NACP chamber for small fields were converted to absorbed dose by applying a calibration factor equal to this ratio.

Due to the extra calibration step, the measurements with the NACP chamber were not made in strict accordance with the code of practice. Any errors introduced by this extra step are likely to be very small, however, since the long term reproducibility of both chambers is better than 0.5% [34].

TLDs were chosen to assess output for the oblique incidence and bolus phantoms because of their small size. TLD measurements were preferable to those of an ion chamber because experiments 3 and 4 require measurements to be made in regions containing a dose gradient. In the case of the obliquely incident field, an ion chamber measurement would require the entry face of the chamber to be situated at an angle of 30° to the horizontal to facilitate normal incidence of the beam central axis. Consequently, one side of the chamber would be closer to the phantom

surface, resulting in a dose gradient across the chamber. The bolus phantom contains steep dose gradients due to the scattering effect of the bolus edge. Output measurements were made in the most homogeneous dose region but the relatively large surface area of parallel plate chambers would still result in an appreciable dose gradient across the chamber, as an examination of figure 2.12 shows. The detector requires a small cross-sectional area to reduce errors associated with averaging a changing dose over the detector volume. Using TLD is, therefore, preferable to ion chamber dosimetry.

TLDs were of the lithium fluoride square chip variety and were described in detail in chapter 2. Prior to experiments 3 and 4, a batch of 20 TLDs was selected and calibrated against the Roos chamber. To achieve this, each of the TLDs was first assigned a relative sensitivity according to the method described in appendix A2.1. The TLDs were then annealed using a temperature cycle recommended by the manufacturer (1 hour at 400°C followed by 14 hours at 80°C). Ten TLDs were exposed to an electron beam under reference conditions (10 x 10 field, 100 cm SSD). This exposure was made with a set number of monitor units, with TLDs situated at the depth of dose maximum in a WTe solid water phantom. A beam energy of 12 MeV was selected since this was the energy at which subsequent TLD output measurements were made. The solid water was then replaced with the water tank, and the Roos chamber used to measure the absorbed dose delivered under the same reference conditions. A batch calibration factor was then assigned to all 20 TLDs. The remaining 10 TLDs were then divided into two batches of 5 and used to measure output for the obliquely incident and bolus fields.

5.3 Results

5.3.1 Experiment 1. Variation of output with SSD

Figures 5.1 – 5.4 show the variation in output with SSD for field sizes of 10 x 10 cm and 5 x 5 cm at beam energies of 6 and 16 MeV. Measured values are compared to those calculated by the two treatment planning systems. Both planning systems are constrained to yield an output of 100 MU / 100cGy at all

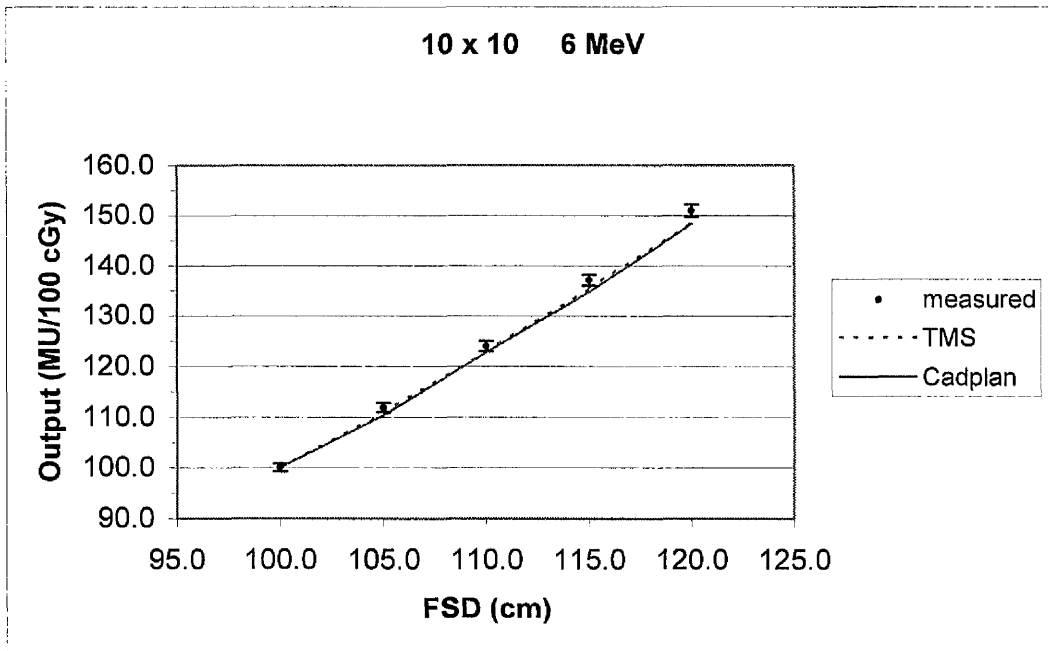


Figure 5.1. Variation of output with SSD for a 6 MeV, 10x10 cm electron field (experiment 1). Measurements were made with an ion chamber in a water phantom. Calculations performed by Helax TMS and Varian Cadplan.

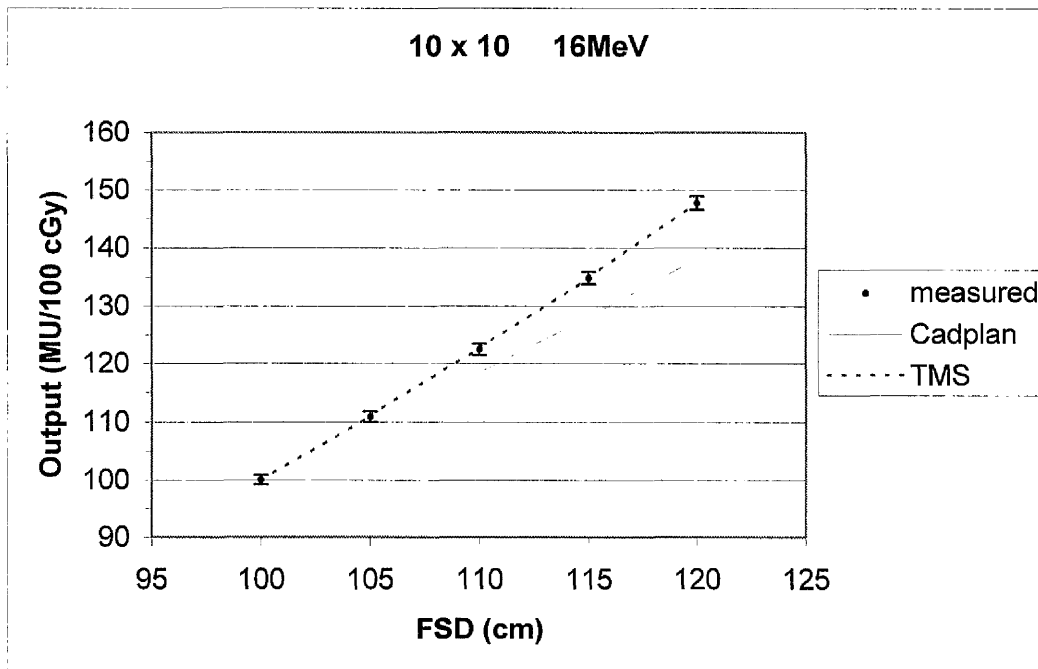


Figure 5.2. Variation of output with SSD for a 16 MeV, 10x10 cm electron field (experiment 1). Measurements were made with an ion chamber in a water phantom. Calculations performed by Helax TMS and Varian Cadplan.

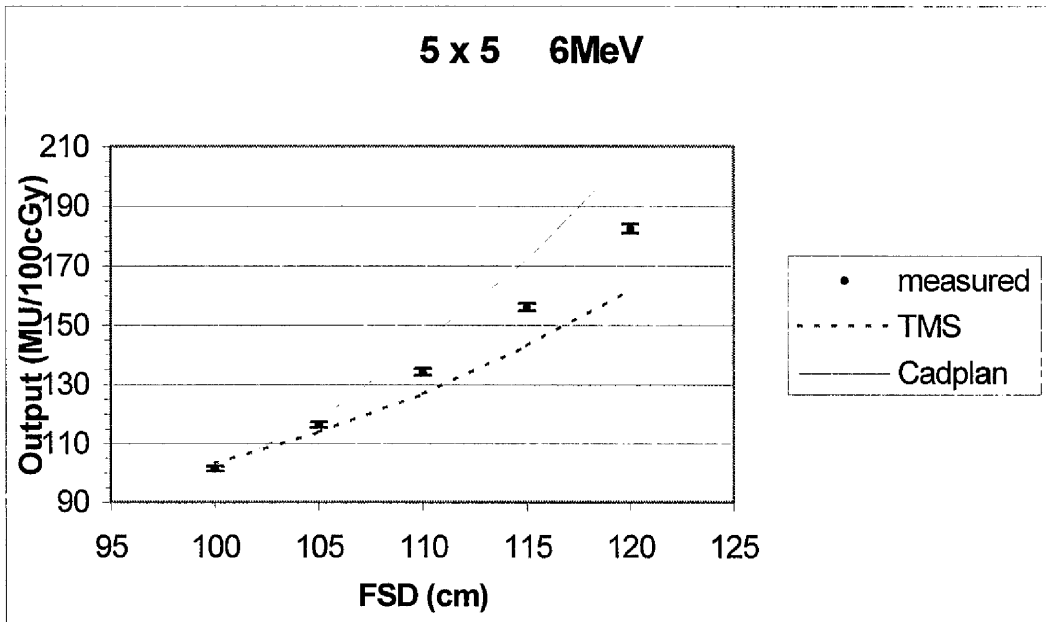


Figure 5.3. Variation of output with SSD for a 6 MeV, 5 x 5 cm electron field (experiment 1). Measurements were made with an ion chamber in a water phantom. Calculations performed by Helax TMS and Varian Cadplan.

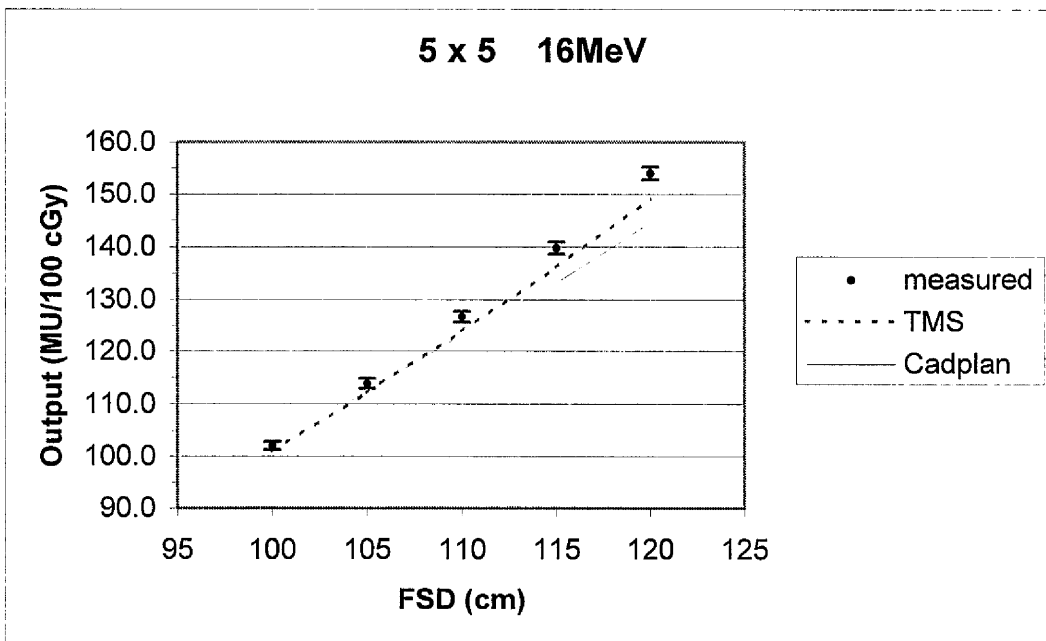


Figure 5.4. Variation of output with SSD for a 16 MeV, 5 x 5 cm electron field (experiment 1). Measurements were made with an ion chamber in a water phantom. Calculations performed by Helax TMS and Varian Cadplan.

beam energies for a 10 x 10 cm field size at 100 cm SSD. For the measured outputs, there is a systematic difference between the IPEMB 1996 dosimetry protocol, and the earlier protocol in use at the time the linear accelerator used in this work was commissioned. The impact of this systematic difference is discussed in section 5.4. In order to aid clarity in comparing the trends in the relation between output and SSD, the effects of this difference were removed by normalising the measured outputs to 100 MU/ 100 cGy for a 10 x 10 cm field at 100 cm SSD for both 6 and 16 MeV energies.

The IPEMB quote an estimated uncertainty of 2.5% (1 standard deviation) in the measurement of absolute dose [34]. In assessing the uncertainty of measured outputs in a comparison with calculations, this uncertainty is not relevant since the planning computers merely reproduce the measured output at 100 cm SSD. The magnitude of uncertainty in relative output measurements at *extended* SSD, is therefore related only to any additional uncertainties arising from taking these further measurements. Reproducibility in measurements of a single dose value were estimated at 0.1% (1 s.d.) for this work. The IPEMB quote an inter-measurement uncertainty of 0.8% due to set-up errors and limitations in the instrument readout. A pragmatic approach is to quote the error in relative dose measurements made with the Roos chamber in this work as the larger of the these two figures i.e. +/- 0.8%.

Of the four fields shown in figures 5.1 – 5.4, the largest discrepancies between measured and calculated data arise for the 5 x 5 cm, 6 MeV field. The measurements demonstrate a significantly steeper gradient in the relation between output and SSD for this field. This steeper gradient has not been reproduced accurately by either planning system. Table 5.2 shows the discrepancies between the measured and calculated outputs at 110 cm and 120 cm SSD for beam energies 6 and 16 MeV at the 10 x 10 cm field size. The table also shows discrepancies at the 5 x 5 cm field size.

| SSD (cm) | 110 | | | | 120 | | | |
|-----------------|---------|------|-------|------|---------|------|-------|------|
| Field size (cm) | 10 x 10 | | 5 x 5 | | 10 x 10 | | 5 x 5 | |
| Energy (MeV) | 6 | 16 | 6 | 16 | 6 | 16 | 6 | 16 |
| TMS (%) | -0.9 | +0.2 | -5.5 | -2.2 | -1.5 | +0.1 | -11.2 | -3.8 |
| Cadplan (%) | -3.2 | -3.3 | +7.5 | -2.8 | -0.3 | -6.4 | +13.6 | -6.2 |

Table 5.2 Discrepancies between calculated and measured output for various electron fields at 110 cm and 120cm SSD. Percentage discrepancies are positive where the planning system's calculation exceeds the measurement.

Figures 5.1 to 5.4 and table 5.2 demonstrate increasing errors in the calculated output as the SSD increases. To investigate the cause of this trend, the relation between output and SSD used by the planning computers was assessed by calculating the virtual SSD implied by their output values. This was done by re-arranging equation 1 and finding the mean value of Z_{virtual} over the SSD range 105 – 120 cm at a each combination of field size and energy. The results are shown in figures 5.5 and 5.6. The virtual SSD implied by the measured output / SSD relation is also shown. In addition to beam energies 6 and 16 MeV, figure 5.5 (for the 10 x 10 cm field size) includes data for beam energies 9, 12 and 20 MeV.

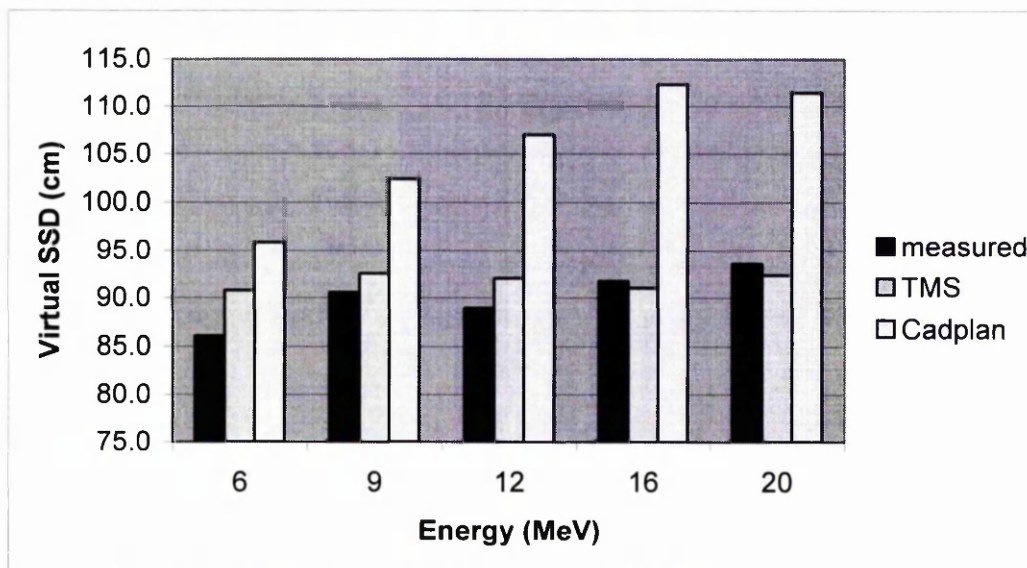


Figure 5.5. Virtual SSDs values implied by the variation of output with SSD in the measured and calculated data for a 10 x 10 cm electron field. Calculations performed according to equation 1.

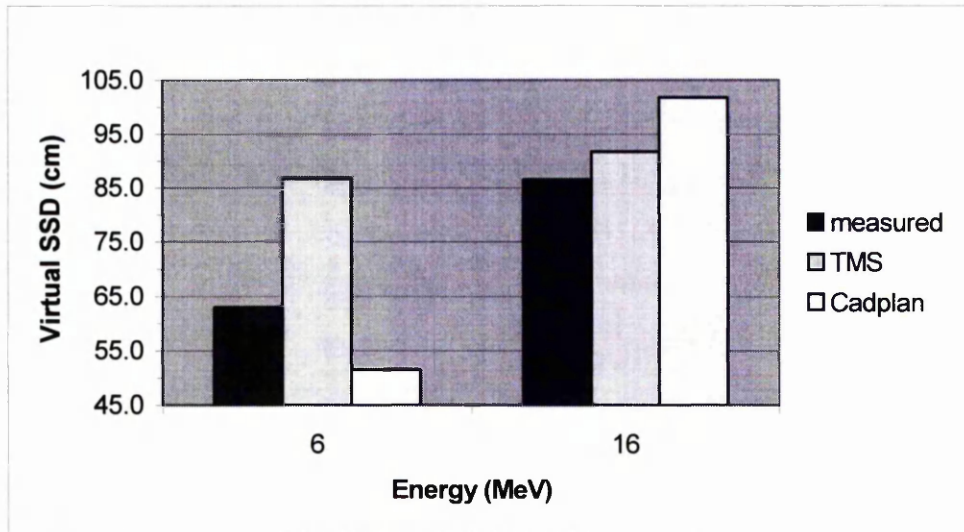


Figure 5.6. Virtual SSDs values implied by the variation of output with SSD in the measured and calculated data for a 5 x 5 cm electron field. Calculations performed according to equation 1.

Figure 5.5 reveals a serious flaw in the calculation performed by Cadplan for the 10 x 10 cm field. Virtual SSDs identical to the measured values were supplied to this system prior to the assessment. These should be reflected in the calculated virtual SSDs but are not. Furthermore, the values of virtual SSD actually apparent in the calculated data are greater than 100 cm for beam energies 9 – 20 MeV. Thus, calculated electron fluence beyond the applicator falls off less rapidly with SSD than an inverse square law based on the physical source position would dictate. Physically, this is unrealistic.

Measured values of virtual SSD are considerably smaller for the 5 x 5 cm field than for the 10 x 10 cm field. Furthermore, at the smaller field size, figure 5.6 reveals that the measured virtual SSD shows a clear energy dependence. It is significantly reduced at the lower beam energy. The explanation for this lies in the increased role of scatter from the cutout to the D_{max} point on the central axis at the standard SSD for the small, low energy field. This scatter contribution diminishes very rapidly at extended SSD and causes this field to exhibit a very small virtual SSD.

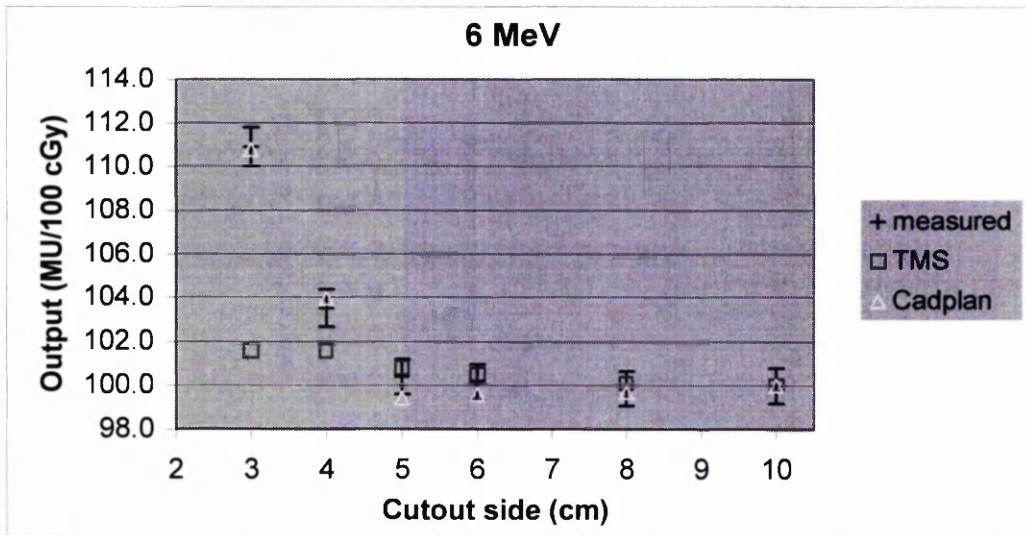


Figure 5.7. Variation in output with field size for a 6 MeV electron field at 100 cm SSD. Measured data was collected with an ion chamber in a water phantom, and has error bars displayed.

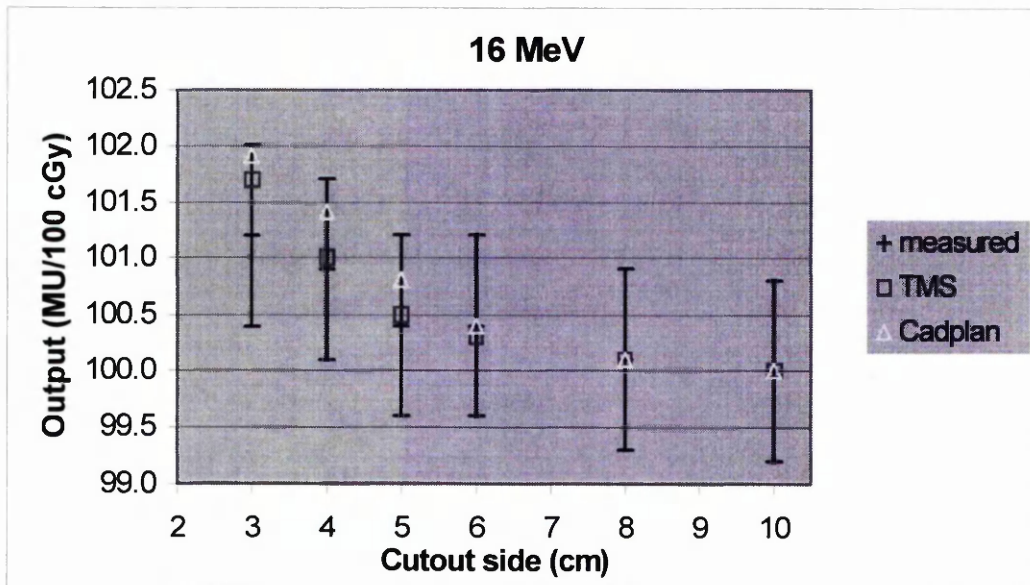


Figure 5.8. Variation in output with field size for a 16 MeV electron field at 100 cm SSD. Measured data was collected with an ion chamber in a water phantom, and has error bars displayed.

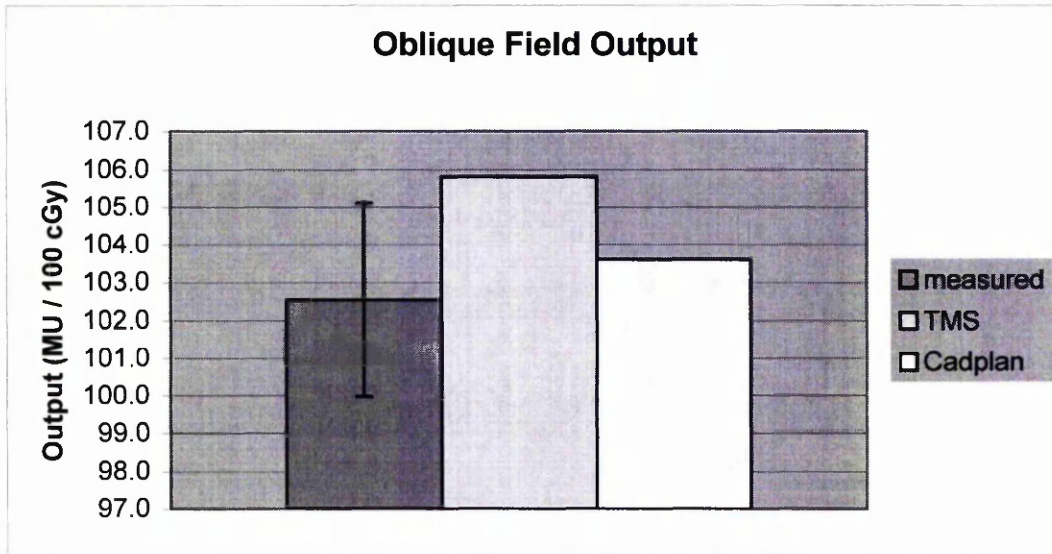


Figure 5.9. Measured and calculated outputs for a 12 MeV, 10 x 10 cm electron field incident on a plain phantom at an angle of 30° to the vertical. Output values are relative to the same field with normal incidence.

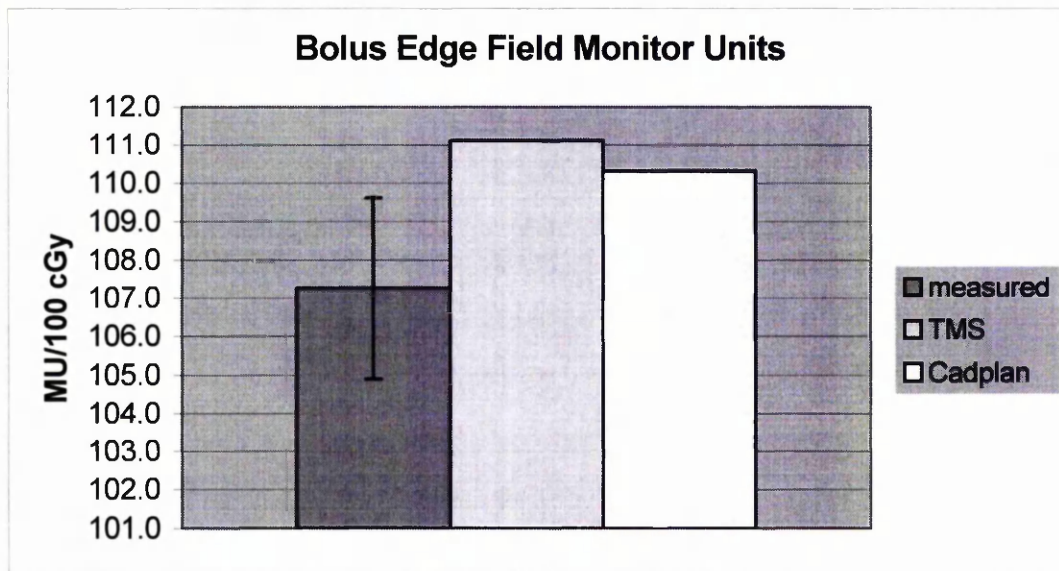


Figure 5.10. Measured and calculated outputs for a 12 MeV, 10 x 10 cm electron field incident on a surface containing a tapered bolus edge. Output values are relative to the same field incident on a plain phantom.

5.3.2 Experiment 2. Variation of output with field size

The relation between output and field size is shown in figures 5.7 and 5.8. A 10 x 10 cm applicator was fitted with successively smaller ostalloy cutouts of thickness 11 mm to produce the required field size variation. Beam energies of 6 and 16 MeV were considered. The lower beam energy was not modelled accurately by the TMS algorithm at field sizes smaller than 5 x 5 cm. Loss of side scatter equilibrium for these fields results in a sharp increase in measured output, typically of the order of 10% on reducing field size from 5 x 5 cm to 3 x 3 cm. The theoretical extrapolation from a plain 10 x 10 cm field size used by TMS has failed to model this loss of side scatter. Reliance on a stored table of output versus field size, however, allows Cadplan to reproduce the effect accurately.

5.3.3 Experiments 3 and 4. Oblique incidence and bolus fields

Outputs for the obliquely incident and tapered bolus fields are shown in figures 9 and 10. The beam energy is 12 MeV in each case. Outputs were measured with TLDs. The estimated uncertainty in measured output was +/- 2.2%. This figure is justified in section 5.4 (Discussion).

The output for the 30° oblique field calculated by TMS exceeds the measured value by 3.4%, while Cadplan proves accurate to within 1%. Both planning systems calculate higher outputs for the bolus phantom than those indicated by the measurements: TMS by 3.9% and Cadplan by 2.7%. A known systematic error in the value of the standard output supplied to the planning systems at the commissioning stage contributes to the size of these discrepancies. This is discussed in section 5.4.4. The impact on overall treatment accuracy of the errors in output value can only be assessed properly when considered with the respective isodose distributions shown in chapter 2.

5.4 Discussion

The aim of this work was to assess the accuracy of two treatment planning systems, Helax TMS v4.1A and Varian Cadplan v3.1.1, in the calculation of electron output. Experiments were performed to test the calculation accuracy under conditions removed from the standard reference conditions, where output is pre-defined in the planning systems. Four such situations were considered: extended SSD; reduced field size; oblique incidence; and incidence on a tapered bolus edge.

5.4.1 Measurement and Calculation Uncertainties

The accuracy of output calculations made by the treatment planning systems was assessed by comparison with ion chamber and TLD measurements. Ion chamber measurements were made in accordance with the IPEMB 1996 code of practice. Chamber measurements were used to assess output directly, and as a means of calibrating TLD devices. The reproducibility of measurements made with the Roos chamber in this work was approximately 0.1%, though an inter-measurement uncertainty of +/- 0.8% has been quoted in accordance with IPEMB recommendations [34].

This random uncertainty is small in comparison with the systematic discrepancies which can be expected in a comparison with planning computer calculations. One such systematic discrepancy is introduced purely because of the choice of dosimetry protocol. The original output measurements on which both planning systems base their calculations were made in accordance with the HPA (1985) code of practice [86]. It has been noted that output measurements made in accordance with this protocol may differ from those made under the current IPEMB protocol by as much as 1.5 % [87]. In fact, for a 12 MeV 10 x 10 cm field, measurements made in this work revealed a 1.2% decrease in measured output (in MU/100cGy) on moving from the HPA to IPEMB protocols. This effect may be ignored in the comparisons involving SSD and field size variations. Here, measured and calculated outputs were normalised to 100% for a 10 x 10 cm,

100 cm SSD field to aid clarity. The difference will, however, contribute to any discrepancy between measured and calculated output for the oblique incidence and tapered bolus experiments, where absolute output values were considered.

There are many other factors which could introduce systematic errors to the calculated outputs. The relation between beam fluence at the accelerator monitor chamber and absorbed dose at depth in a patient or phantom is a complex one. The physical interactions undergone by electrons which influence this relation may be divided into two broad categories: those occurring in the machine head, and those occurring in the phantom. Machine head interactions include scatter (both forwards to the phantom and back to the chamber) from metallic objects such as the secondary collimators, applicator and cutout, and modifications to the beam fluence profile caused by the scattering foil. Phantom interactions consist largely of multiple small angle scattering events with atomic electrons in the phantom material. Thus a change in, for example, applicator size, or the addition of bolus to the phantom surface, could both alter the electron fluence at a given point within the phantom. To calculate the monitor units required to give a particular dose in the phantom with acceptable accuracy, a planning computer must either model these effects explicitly or screen them out by relying on measured data.

5.4.2 Experiment 1. Variation of output with SSD

Experiment 1 considered the variation in output with SSD. At SSDs beyond the standard distance of 100 cm, the beam area expands, resulting in reduced electron fluence at the central axis. There is a consequent increase in output which, in the case of photon fields, can be calculated with great accuracy by applying a simple inverse square correction i.e. the beam fluence varies as the inverse of the square of the source to phantom distance. The output, therefore, varies as the square of the source to phantom distance. For electron fields, scatter events in the machine head cause the beam area to expand more rapidly, causing this simple inverse square relation to breakdown. Moreover, the degree to which scatter affects the beam area beyond the standard SSD is dependent on beam energy and applicator size

[48,88]. This work has examined the relation between output and SSD for beam energies in the range 6 to 20 MeV at field sizes of 10 x 10 cm and 5 x 5 cm.

Output values at 100 cm SSD are supplied to both TMS and Cadplan at the commissioning stage. Data is supplied for all available beam energies at each of the standard square applicator sizes (6, 10, 15, 20 and 25 cm). For Cadplan, data is also supplied at intermediate field sizes and for sizes below 6 x 6 cm. The two planning systems use different methodologies to extrapolate this basic data to calculate output at extended SSDs. Cadplan adopts a three stage process. Firstly, any effects that the algorithm employed by Cadplan to calculate phantom scatter has on absorbed dose at the D_{\max} depth at reduced field size are reversed by application of a field size factor from a stored data table. Secondly, the output at 100 cm SSD for the appropriate field size is found from a second stored data table. Finally, the treatment field output is calculated by applying an inverse square correction using a virtual SSD found by referring to a third data table. Values for the first table are inferred by the user at the commissioning stage using a protocol provided by the manufacturers. The second and third tables use measured data. Values of virtual SSD measured in this work were used in the third data table.

TMS attempts to model the electron fluence at extended SSD by expanding the beam such that the centre of the penumbra is consistent with a set of full width at half maximum (FWHM) measurements. These are made at the standard and extended SSD at the commissioning stage. For a given field at extended SSD, this allows the surface fluence on the beam central axis relative to a reference beam to be calculated. Phantom scatter is then added explicitly in order to calculate the fluence at the normalisation point, and the output calculated.

For the 10 x 10 cm field size, the calculation of output by Cadplan is not accurate. The calculated output often falls outwith the uncertainty range in the measurements, as figures 5.1 and 5.2 show. The calculation becomes progressively less accurate as the SSD is increased. Table 5.2 shows, for example, that output for the 16 MeV field is underestimated by 3.3% at 110 cm SSD, and by 6.4% at 120 cm SSD. Figure 5.5, which shows the values of virtual SSD implied

by the measured and calculated outputs, illustrates the reason for the increased error in calculated output at higher SSDs. For all the beam energies, Cadplan fails to reproduce the values of virtual SSD in its own tables. The result is a divergence from measurements in the output / SSD relation giving increasing errors in the calculated outputs as the SSD is increased. Varian has been approached about this but has yet to offer an explanation for this failure.

Cadplan shows a similar failure to reproduce the correct values of virtual SSD for the 5 x 5 cm field. The most serious consequence of this arises for the 6 MeV field, which has the smallest of all measured virtual SSDs, and therefore, an output which increases very rapidly with SSD. In contrast to the 10 x 10 cm field, Cadplan overestimates the output. The error increases with SSD to reach 13.6% at 120 cm.

There are no known flaws in the calculation algorithm which would explain Cadplan's failure to reproduce the relation between output and SSD. While this situation persists, the magnitude of the errors precludes the clinical use of Cadplan for output calculations at extended SSD.

The TMS calculation of output proved accurate to within 1% at all SSDs for the 10 x 10 cm, 16 MeV field. Accuracy at 6 MeV for this field size was to within 1.5%. As with Cadplan, the smaller 5 x 5 cm field is not modelled as accurately. Calculated outputs are consistently less than the measured values. At 110 cm, the discrepancies are 5.5% and 2.2% for 6 and 16 MeV fields respectively. The corresponding figures at 120 cm SSD are 11.2% and 3.8%.

Inadequacies in the TMS algorithm cause the large discrepancies at 6 MeV. The FWHM method may be accurate in describing field edge position but there is no reason to believe it provides an accurate indication of relative electron fluence on the central axis, nor, therefore, of the beam output. Furthermore, while phantom scatter is explicitly modelled, scatter from the applicator and cutout are not. Any contribution these make to the beam fluence on entry to the phantom is, therefore,

ignored. As with Cadplan, the use of TMS to calculate outputs at extended SSD is not advisable.

5.4.3 Experiment 2. Variation of output with field size

Experiment 2 examined the relation between field size and output. Beam energies of 6 and 16 MeV were considered for a 100 cm SSD field incident normally on a water phantom. A 10 x 10 cm field defined by a plain applicator was reduced in size by introducing successively smaller square ostalloy cutouts. The addition of these field-defining apertures was modelled on the planning systems by defining aperture blocks in the beam's eye view image.

Both planning systems use a ray-tracing method to determine the position of the blocks in relation to any given point in the phantom, and to the physical electron source. Cadplan then uses this information to calculate an equivalent field size which is used to look up an output value from a stored data table. For the 10 x 10 cm applicator, this table contains measured output values for square fields measuring from 2 x 2 cm upwards. The stored output values agree with those measured in this work to within 0.5%. In contrast to this, TMS attempts to integrate scatter contributions to dose at the normalisation point from pencil beams in the open field. The resulting dose is then compared to that which would have been calculated for a 10 x 10 cm reference field (for which the output is known), and the monitor units scaled accordingly.

As would be expected of a system which simply refers to a look-up table of output versus field size, Cadplan predicts the former with acceptable accuracy for all field sizes at both energies. Calculated and measured values agree to within the measurement uncertainty of 0.8%. This provides confirmation that the field defining apertures are being interpreted correctly in a geometrical sense, and an appropriate equivalent field size calculated.

At 16 MeV, the TMS output calculation proves accurate to within 1% for all field sizes. This level of accuracy is not, however, maintained at 6 MeV. Here the

calculated and measured outputs agree to within 1% for field sizes of 5 x 5 cm and above, but for the 4 x 4 cm and 3 x 3 cm fields, there are discrepancies of 1.8% and 8.4% respectively. There is an obvious failure by TMS to reproduce the sharp increase in output measured for the smallest field sizes. Physically, the increase in output is caused by loss of side scatter equilibrium on the beam central axis. While this provides a difficult test, the explicit modelling of phantom scatter carried out by TMS should reproduce the effect adequately. Helax could not offer an explanation for this failure, but indicated that they expect future software releases to be more accurate.

5.4.4 Experiments 3 and 4. Oblique incidence and bolus fields

Experiments 3 and 4 examined output calculations for two specific set-up geometries. Firstly, a field incident obliquely on a plain WTe electron solid water phantom, and secondly, a field normally incident on the same phantom with a tapering PMMA block mounted on the beam entry surface to simulate a bolus edge.

Since the obliquely incident field measures 10 x 10 cm, and has a SSD of 102 cm, the beam fluence profile on entry to the phantom is close to that of a standard 10 x 10 cm beam. To a large extent, therefore, the experiment tests the ability of each planning computer to compute phantom scatter from the oblique field in relation to a normally incident field. Similarly, accurate computation of the phantom scatter imposed on a standard 19 x 19 cm field by the presence of the bolus is crucial in this simulation.

It has been reported that oblique incidence tends to increase dose at the D_{\max} point [38]. This effect has not been reproduced in these measurements. As discussed above, a 1.2% difference between calculated and measured outputs was expected to occur due to a systematic difference between dosimetry measurements made in this work and those used to supply data to the planning computers. Calculated outputs from both planning computers were expected to be 1.2 % higher than the measured values. After subtracting this amount from the calculated

values, Cadplan calculates output for the oblique field to within 0.5% of the measured value while TMS overestimates this output by 2.2%. As discussed in chapter 2, the uncertainty in TLD measurements of relative dose is approximately +/- 2.0%. To find the uncertainty in a TLD measurement of absolute dose, this figure must be added, in quadrature, with the 0.8% uncertainty in ion chamber measurements used to calibrate the TLDs. This addition yields an uncertainty in TLD output measurements of +/-2.2%. For TMS, discrepancies between measured and calculated output for the oblique field are, therefore, just within the uncertainty range of the measurements, and are therefore insignificant.

Both systems overestimate outputs for the bolus experiment: after subtracting the 1.2 % systematic error from the calculated data, TMS overestimates by 2.7% and Cadplan by 1.9%. The result of the Cadplan calculation lies, therefore, within the expected range, while that of TMS falls just outside. The point at which output was measured and calculated in the bolus phantom was subject to a dose gradient, as an examination of figure 2.12 shows. Consequently, there will be some additional uncertainty in the measured output for this experiment due to the uncertainty in the TLD position. The discrepancy in the TMS calculation, is therefore unlikely to be significant.

Samuelsson *et al* [20] report consistent underestimation of outputs by Cadplan for test geometries involving off-axis normalisation, as is the case in the bolus experiment. This is caused by the computer model's failure to account for modifications to the beam fluence introduced by the scattering foil. The TMS algorithm has the same omission. If present, this effect would partially offset the overestimation in calculated output caused by errors in the phantom scatter algorithms, and suggests therefore, that the errors in phantom scatter are larger than the figures quoted above.

Appendix A5.1

Conversion from ionisation to absorbed dose with Roos 34001 chamber

For measurements made with the Roos chamber, the IPEMB 1996 Code of Practice [34] states that the absorbed dose to water, D_w , at a depth Z is:

$$D_{w,z} = M \times N_{D,air} \times S_{w/air} \times P_{ch} \quad (1)$$

Where M is the corrected chamber reading in arbitrary units given on the electrometer display; $N_{D,air}$ is a calibration factor relating the chamber reading to absorbed dose to air, and arises from the calibration of the Roos chamber against a secondary standard chamber; $S_{w,air}$ is the (energy dependent) water to air stopping power ratio at depth Z , and P_{ch} is the chamber perturbation factor.

The values of $S_{w/air}$ and P_{ch} are tabulated in the Code of Practice. $S_{w/air}$ has a value of 1.039 for a 12 MeV beam, for example, while P_{ch} has a value of 1.000 for the Roos chamber. The value of $N_{D,air}$ was assessed when the Roos chamber was calibrated against the secondary standard in accordance with the Code of Practice.

Corrections to the chamber reading, M , were made for the effects of ion recombination; the chamber polarity; and the temperature and pressure. Ion recombination can have a significant impact on collector efficiency; its effects were corrected for by assessing the ratio of chamber readings at full to half voltage. The correction factor for the effects of temperature and pressure, $f_{T,P}$ is given in the Code of Practice as

$$f_{T,P} = (273.15 + T)(1013.25) / (293.15)P \quad (2)$$

where T and P are the temperature and pressure respectively.

CHAPTER 6

CONCLUSIONS

This work examined the accuracy of dose calculations performed by the Varian Cadplan and Helax TMS treatment planning systems. Calculated doses were compared with measurements made in electron beams produced by a Varian 2100C linear accelerator.

The degree of accuracy required by a treatment planning system is that which is acceptable to the clinician responsible for the patient's treatment. In practice, this will usually coincide with the criteria for accuracy laid down by the International Commission on Radiation Units and Measurements (ICRU). The ICRU have stipulated limits on the discrepancy with the actual dose value that a calculated dose may have. In this work, the "actual" value of dose was determined by measurement. Calculated doses, therefore, were proven to be inaccurate only if they fell outside the range of values defined by the uncertainty limits of the measurements.

In assessing the accuracy of dose calculation by a treatment planning system, it is important to specify the defect in the calculation algorithm which caused a given error. Only then can the information be used to assess the likely impact of this defect on a range of situations. For the two treatment planning systems under consideration, this is best achieved by considering the calculation of relative and absolute doses separately since quite distinct algorithms are employed in their calculation.

The calculation of relative dose was assessed in chapters two, three and four. Chapter two examined planar isodose distributions in three situations: oblique incidence of the electron beam; incidence on an irregular surface designed to resemble a region of bolus; and incidence on a phantom containing a small cylindrical air cavity. Chapter three considered the nature of the electron beam penumbra at extended FSD, and how this affects the optimum gap required between abutting electron and photon fields. Chapter four examined the shape of

the region enclosed by the 90% isodose line in situations where beam-defining inserts are used.

In drawing conclusions on the suitability of the treatment planning systems for clinical use, it is reasonable to place greater emphasis on the results from chapter two. This is because the clinical situations simulated in this comparison require the use of a treatment planning system for dose calculation more often than those described in chapters three and four.

Of the three practical situations assessed in chapter two, those relating to oblique incidence and incidence on a surface containing a bolus edge were calculated with generally acceptable accuracy by both planning systems. Some exceptions were noted, however. TMS produced significant errors at the low dose margin of the distal penumbra for the oblique field. Both planning systems incorrectly estimated the hot spot dose caused by scattered electrons under the bolus edge. The general form of these dose distributions was, however, calculated with sufficient accuracy by both planning systems to justify their clinical use. The calculated dose distributions must, of course, be interpreted with caution. The planning computers should not be relied on in situations where the dose outside the nominal edge of an oblique field, or in the highest dose area underneath a bolus edge, require to be known precisely.

Reliance on the planning computers' calculation would also be inadvisable if the electron beam under consideration passes through a patient or phantom containing a small air cavity. Both planning systems significantly underestimated (by 10%) the doses immediately downstream of a 1.5 cm diameter air cavity. The error was caused by the semi-infinite slab approximation used in modelling lateral electron scatter. For this reason, it is likely that a similar *overestimation* in dose will occur downstream of a small area of high density. Neither planning system, therefore, can be relied on to calculate accurately clinical dose distributions in the vicinity of small air cavities such as the trachea, nor small areas of raised density such as bones.

The comparison of measured and calculated electron beam penumbra (considered in chapter three) demonstrated that the simplified model of electron scatter in air used by the planning systems provides insufficient accuracy at extended SSD. Whereas the position of the penumbra centre was predicted with acceptable accuracy, the penumbra width was not. Interpretation of computed penumbras thus requires caution, particularly at the low and high dose margins of the penumbra. Since these are often important clinically, computed isodose distributions should not be relied on at SSDs beyond 105 cm. If information on the dose coverage at extended SSD is required, it would be preferable to consult measured data. The same precaution should be observed when positioning an extended SSD electron field with abutting photon fields. Optimum gap sizes (determined from measurements) between extended SSD electron fields and isocentric parallel opposed photon fields were tabulated in chapter three for this purpose.

Chapter four confirmed the suitability of the TMS system for displaying the 90% isodose line arising from the use of various field-shaping inserts. When a plane normal to the beam central axis is considered, the calculated 90% isodose line may thus be used as a template to indicate the extent and shape of the region receiving this dose. It has been proposed that the TMS system be used to produce 90% dose templates for the standard range of elliptical beam shaping inserts used in breast boost radiotherapy at the Beatson Oncology Centre. The results of chapters two and three demonstrate that these templates may only be applied to treatments at the standard SSD, and which do not involve a significantly oblique angle of incidence. The majority of electron boost treatments to the breast are likely to satisfy these conditions.

While chapters two, three and four revealed specific instances of inaccuracy in the calculation of relative dose by both planning systems, chapter five showed a great many errors in the calculation of absolute dose. The comparison of measured and calculated monitor units demonstrated that the TMS system uses insufficient detail when modelling head scatter events to provide reliable results for electron fields with dimensions less than 5 x 5 cm. Cadplan's reliance on measured data,

however, gave better results.

In contrast, Cadplan's use of measured data did not lead to the accurate calculation of monitor units for 10 x 10 cm fields at extended SSD. Significant errors arose due to an inability to reproduce values of virtual SSD stored in this system's own data tables. This matter has been taken up with the manufacturer but has not been resolved at the time of writing. As with small fields, the calculation accuracy obtained by TMS at extended SSD suffered because head scatter events were not modelled explicitly. Only an implicit model characterised by a r.m.s. scattering angle optimised, not for the monitor unit calculation, but for reproduction of the field penumbra profile, was used. As a result, unacceptable errors in calculated monitor unit values arose for a variety of beam energies and sizes at SSDs above 100 cm.

The comparison of measured and calculated absolute dose revealed serious deficiencies in the monitor unit calculation algorithms of both TMS and Cadplan. Their use for monitor unit calculations for electron beams is, therefore, not recommended. Relative electron dose distributions from both planning systems may, on the other hand, be relied upon in a clinical setting provided care is taken in interpreting dose distributions. The physicist and clinician must be particularly aware of the potential errors in the calculation of electron beam penumbra, and dose distributions surrounding surface irregularities and small heterogeneities.

Future work

Algorithms for the calculation of absorbed dose from clinical electron beams are evolving continuously. The next step forward for commercially available treatment planning systems is likely to be the introduction of the phase space evolution algorithm. This involves a more complete description of the position, direction and energy (or *phase*) of electrons than that of the generalised Gaussian pencil beam. As with any new beam calculation algorithm, a rigorous comparison with measured data will be required before phase space evolution models of

electron behaviour are introduced clinically. The experiments developed in this work to test the accuracy of pencil beam algorithms would be equally suitable in these future comparisons. Adopting these tests again would, moreover, allow the direct comparison of the phase space evolution and pencil beam algorithms.

REFERENCES

1. Harvey R A, Haas L and Laughlin J S, 1952. Betatron cancer therapy. *Radiology* 58, 23 – 34.
2. Koh W J, Austin-Seymour M M, Russel K J, Griffin B R, Laramore G E and Griffin T W, 1990. Current use of electron beam therapy in the United States. *Radiologica Medica* 80 (4,1): 26 – 27.
3. Reisner K and Haase W, 1990. Electron beam therapy of primary tumours of the skin. *Radiologica Medica* 80(4,1): 114 – 115.
4. Dobrowski W, Schlappack O, Karcher K H, Pavelka R and Kment G, 1986. Electron beam radiotherapy in treatment of parotid neoplasm. *Radiotherapy and Oncology* 6(4): 293 – 299.
5. Ray G R and Fish V J, 1983. Biopsy and definitive radiation therapy in stage I and II adenocarcinoma of the female breast: analysis of cosmesis and the role of electron beam supplementation. *Int. J. Radiation Oncology Biol. Phys.* 9: 813 – 818.
6. Rosenwald J C, Aletti P and Bey P, 1990. Use of electrons for radiotherapy in France. *Radiologica Medica* 80(4,1): 15 – 19.
7. Laughlen J S, 1967. Physical aspects of high energy electron therapy. *American. J. Roentgenology, Radium Therapy & Nuclear Medicine.* 99(4): 915 – 923.
8. Poretti G G and Ionesco-Farca F, 1978. Use of the computer in high energy electron therapy. *Radiologica Clin.* 47: 139 – 153.

9. Bethe H A, Rose M E and Smith L P, 1938. The multiple scattering of electrons. *Proc. Amer. Phil. Soc.* 78: 573.
10. Eyges L, 1948. Multiple scattering with energy loss. *Phys. Rev.* 74: 1534-1535.
11. Hogstrom K R, 1990. Dose calculation algorithms for electron beams [review]. *Phys. Med. Biol.* 37: 900 - 924.
12. Hogstrom K R, Mills D, and Almond P R, 1981. Electron beam dose calculations. *Phys. Med. Biol.* 26: 445 – 459.
13. Brahme A, Lax I and Andreo P, 1981. Electron beam dose planning using discrete Gaussian beams: Mathematical background. *Acta. Radiol. Oncol.* 20: 147 – 158.
14. Hogstrom K R, 1991. Treatment planning in electron beam therapy [review]. *Frontiers of Radiation Therapy and Oncology.* 25: 30 – 52; discussion: 61 – 63.
15. Lax I, Brahme A and Andreo P, 1983. Electron beam dose planning using Gaussian beams. Improved radial dose profiles. *Acta. Rad. Suppl.* 364: 49 – 60.
16. McShan D L, Fraass B A and Ten Haken R K, 1994. Dosimetric verification of a 3-D electron pencil beam dose calculation algorithm. *Med. Phys.* 21: 13 – 23.
17. Cheng A, Harms W B, Gerber R L, Wong J W and Purdy J A, 1996. Systematic verification of a three dimensional electron beam dose calculation algorithm. *Med. Phys.* 23: 685 – 693.
18. Muller-Runkel R and Cho Sang-Hyun, 1997. Evaluation of a commercial three dimensional electron pencil beam algorithm. *Med. Phys.* 24: 91 – 101.

19. Blomquist M, Karlsson M and Karlsson M, 1996. Test procedures for verification of an electron beam pencil beam algorithm implemented for treatment planning. *Radiotherapy and Oncology* 39: 271 – 286.
20. Samuelsson A, Hyodynamaa S and Johansson K-A, 1998. Dose Accuracy check of the 3D electron beam algorithm in a treatment planning system. *Phys. Med. Biol.* 43: 1529-1544.
21. Dose Formalism and Models in Helax-TMS, 1998. Helax AB, Box 1704, S-751 47 Uppsala, Sweden.
22. Cadplan External Beam Modelling Physics, 1999. Varian Medical Systems Finland Oy, Metsanneidonkuja 8, FIN-02130 Espoo, Finland.
23. Use of computers in external beam radiotherapy procedures with high energy photons and electrons. ICRU report 42. International Commission on Radiation Units and Measurement, Bethesda, MD, 1987.
24. McLellan J, Papiez L, Sandison G A, Huda W and Therrien P, 1992. A numerical method for electron transport calculations. *Phys. Med. Biol.* 37: 1109 – 1125.
25. Kapur A, Ma C M, Mok E C, Findlay D O and Boyer A L, 1998. Monte Carlo calculations of electron beam output factors for a medical linear accelerator. *Phys. Med. Biol.* 43: 3479 - 3494.
26. Jera R, Keall P J and Ostwald P M, 1998. Comparisons between MCNP, EGS4 and experiment for clinical electron beams. *Phys. Med. Biol.* 44: 705 - 717.
27. Werner B L, Khan F M and Deibel F C, 1982. A model for calculating electron beam scattering in treatment planning. *Med. Phys.* 9: 180 – 187.

28. Lax I and Bramhe A, 1985. Electron beam dose planning using Gaussian beams. Energy and spatial scaling with inhomogeneities. *Acta Rad. Onc.* 24: 75 – 85.
29. Andreo P and Ahnesjö A, 1991. Electron pencil beams in different media: A comparison between the EGS and ITS Monte Carlo codes. Proceedings of World Congress of Medical Physics and Biomedical Engineering, Kyoto, Japan.
30. Attix H (ed.) 1967. Luminescence Dosimetry: pp 3-14. US Atomic Energy Commission, Springfield, Virginia.
31. Radiation Dosimetry: Electron Beams with Energies Between 1 and 50 MeV, ICRU Report No. 35: 91 - 92. International Commission on Radiation Units and Measurement, Bethesda, MD, 1984.
32. Mayles W P M, Heisig S and Mayles H M O, 1993. In Williams J R and Thwaites D I (eds.), *Radiotherapy Physics in Practice*. Oxford University Press, Oxford pp 233 – 234.
33. Essers M and Mijnheer B J, 1999. *In vivo* dosimetry during external photon beam dosimetry. *Int. J. Radiation Oncology Biol. Phys.* 43: 245 – 259.
34. Thwaites D I, Burns D T, Klevenhagen S C, Nahum A E, and Pitchford W G, 1996. The IPEMB code of practice for electron dosimetry for radiotherapy beams of initial energy from 2 to 50 MeV based on an air kerma calibration. *Phys. Med. Biol.* 41: 2557 – 2603.
35. Nisbet A and Thwaites D I, 1998. An evaluation of epoxy resin phantom materials for electron dosimetry. *Phys. Med. Biol.* 43: 1523 – 1528.

36. Mobit N, Nahum A E and Mayles P, 1996. The energy correction factor of LiF thermoluminescent dosimeters in megavoltage electron beams: Monte Carlo simulations and experiments. *Phys. Med. Biol.* 41: 979 - 993.
37. Roback D M, Khan F M, Gibbons J P and Sethi A, 1995. Effective SSD for electron beams as a function of energy and beam collimation. *Med. Phys.* 22: 2093 – 2095.
38. Khan F M, Deibel F C and Soleimani-Meigooni A, 1985. Obliquity correction for electron beams. *Med. Phys.* 12: 749-753.
39. Lax I, 1986. Inhomogeneity corrections in electron-beam dose planning. Limitations with the semi-infinite slab approximation. *Phys. Med. Biol.* 31(8): 879 – 892.
40. Lee A W M, Law S C K, Foo W *et al*, 1993. Nasopharyngeal carcinoma: local control by megavoltage radiation. *Br. J. Radiol.* 66: 528-536.
41. Sykes A J, Allan E, Irwin C, 1996. Squamous cell carcinoma of the lip: the role of electron treatment. *Clinical Oncology* 8(6): 384-386.
42. Coleman C W, Roach M 3rd, Ling S M *et al*, 1997. Adjuvant electron-beam IORT in high-risk head and neck cancer patients. *Frontiers of Radiation Therapy and Oncology.* 31: 105-111.
43. Papiez E and Dunscombe P B, 1992. Matching photon and electron fields in the treatment of head and neck tumours. *Med. Phys.* 19(2): 335-341.
44. Reisinger S A, Ayyanger K, Flanders A *et al*, 1995. Potential underdosing with the use of electron beam therapy in patients with cervical adenopathy and advanced head and neck cancer. *Medical Dosimetry* 20(1): 7-10.

45. Sun C, Cheng C, Shimm D S and Cassady J R, 1998. Dose profiles in the region of abutting photon and electron fields in the irradiation of head and neck tumors. *Medical Dosimetry* 23(1): 5-10.
46. Khan F M, Sewchand W W and Levitt S H, 1978. Effect of air space on depth dose in electron beam therapy. *Radiology* 126. 249-251.
47. Cygler J, Li X A, Ding X D and Lawrence E, 1997. Practical approach to electron beam dosimetry at extended SSD. *Phys. Med. Biol* 42: 1505-1514.
48. Khan F M, Doppe K P, Hogstrom F R *et al* 1991. Clinical electron beam dosimetry: Report of AAPM Radiation Therapy Committee Task Group No. 25. *Med. Phys* 18: 73-107.
49. Das I J, McGee K P and Cheng C, 1995. Electron beam characteristics at extended treatment distances. *Med. Phys.* 22(10): 1667-1674.
50. Rikner G and Grusell E, 1987. General specifications for silicon semiconductors for use in radiation dosimetry. *Phys. Med. Biol.* 32(9): 1109-1117.
51. Rikner G, 1985. Characteristics of a p-Si detector in high energy electron fields. *Acta. Radiol.* 24(1): 71-74.
52. Das I J, Cheng C W and Healey G A, 1995. Optimum field size and choice of isodose lines in electron beam treatment. *Int. J. Radiation Oncology Biol. Phys.* 31(1): 157 – 163.
53. Lax I, 1986. Development of a generalised Gaussian model for absorbed dose calculation and dose planning in therapeutic electron beams. PhD thesis, University of Stockholm: 35 - 37.

54. Huizenga H and Storchi P R M. The in-air scattering of clinical electron beams as produced by accelerators with scanning beams and diaphragm collimators. *Phys. Med. Biol.* 32: 1011-1029.
55. Johnson J M and Khan F M, 1994. Dosimetric effects of abutting extended source to surface distance electron fields with photon fields in the treatment of head and neck cancers. *Int. J. Radiation Oncology Biol. Phys.* 28(3): 741-747.
56. Khan F M, Moore V C and Levitt S H, 1976. Field shaping in electron beam therapy. *British Journal of Radiology*, 49, 883-886.
57. Nair R P, Nair T K M, and Wrede D E, 1983. Shaped field electron dosimetry for a Philips SL75/10 linear accelerator. *Med. Phys.* 10(3), 356-360.
58. Bukovitz A G, Saini D, Gur D and Sweeney L E, 1980. Dosimetric evaluation of a variable field electron beam applicator. *Med. Phys.* 7(3), 226-9.
59. Jamshidi A, Kuchnir F T, and Reft C S, 1987. Characteristic parameters of 6-22 MeV electron beams from a 25-MeV linear accelerator. *Med. Phys.* 14(2) 282-288.
60. Al-Ghazi M S, Lingman D, Arjune B *et al*, 1991. Characteristic parameters of 6-21 MeV electron beams from a 21 MeV linear accelerator. *Med. Phys.* 18(4), 821-828.
61. Sabbas A M, Jette D, Rozenfeld M *et al*, 1987. Collimated electron beams and their associated penumbra widths. *Med. Phys.* 14(6), 996-1006.

62. Touboul E, Belkacemi Y, Lefranc J *et al*, 1995. Early breast cancer: influence of type of boost (electrons vs iridium-192 implant) on local control and cosmesis after conservative surgery and radiation therapy. *Radiotherapy and Oncology* 34, 105-113.
63. Schmidt-Ullrich R K, Wazer D E, Dipertillo T *et al*, 1993. Breast conservation therapy for early stage breast carcinoma with outstanding 10-year locoregional control rates: a case for aggressive therapy to the tumor bearing quadrant. *Int. J. Radiation Oncology Biol. Phys.* 27, 545-542.
64. Pezner R D, Lipsett J A, Desai K *et al*, 1988. To Boost or not to boost: decreasing radiation therapy in conservative breast cancer treatment when “inked” tumor resection margins are pathologically free of cancer. *Int. J. Radiation Oncology Biol. Phys.* 14, 873-877.
65. Machtay M, Lanciano R, Hoffman J and Hanks G E, 1994. Inaccuracies in using the lumpectomy scar for planning electron boosts in primary breast carcinoma. *Int. J. Radiation Oncology Biol. Phys.* 30(1), 43-48.
66. Gilligan D, Hendry J A and Yarnold J R, 1994. The use of ultrasound to measure breast thickness to select electron energies for breast boost radiotherapy. *Radiotherapy and Oncology.* 32 265-267.
67. Prescribing, Recording, and Reporting Photon Beam Therapy. ICRU report 50. *International Commission on Radiation Units and Measurement, Bethesda, MD, 1993.*
68. Dutreix J and Dutreix A, 1969. Film dosimetry of high energy electrons. *Ann. N.Y. Acad. Sci.* 161, 33.

69. Hettinger G and Svensson H, 1967. Photographic film for determination of isodoses from betatron electron radiation. *Acta. Radiol.* 6, 61.
70. Feldman A, De Almeida C E and Almond P R, 1974. Measurements of electron beam energy with rapid processed film. *Med. Phys.* 1, 74.
71. Anderson D W and St. George F, 1979. Compression of film and ion chamber systems for depth-dose measurements for a 25MV beam. *Phys. Med. Biol* 24(3), 636-638.
72. Williamson J F, Khan F M and Sharma S C, 1980. Film dosimetry of megavoltage photon beams: A practical method of isodensity-to-isodose curve conversion. *Med. Phys.* 8(1), 94-98.
73. Tsai Y S, 1974. Pair production and bremsstrahlung of charged leptons. *Rev. Mod. Phys.* 46, 815.
74. Koch H W and Motz J W, 1959. Bremsstrahlung cross-section formulas and related data. *Rev. Mod. Phys.* 31, 921.
75. Lax I and Brahme A, 1980. On the collimation of high energy electron beams. *Acta. Radiol. Oncol.* 19, 199.
76. Stacy A J, Bevan A R and Dickens C W, 1961. A new phantom material employing depolymerised natural rubber. *Br. J. Radiol.* 34, 510-513.
77. Klevenhagen S C, 1985. Physics of Electron Beam Therapy, p85. (Bristol: Adam Hilger Ltd).
78. Shiu A S, Tung S and Hogstrom K R, 1992. Verification data for electron beam dose algorithms. *Med Phys.* 19(3), 623-636.

79. Milan J and Bentley R E, 1974. The storage and manipulation of dose data in a small digital computer. *Br. J. Radiol* 47(554): 115-21.
80. Cunningham J R, Shrivastava P N and Wilkinson J M, 1972. Program IRREG: calculation of dose from irregularly shaped radiation beams. *Comput. Progr. Biomed.* 2: 192 – 199.
81. Ahnesjö A, Saxner M and Trepp A, 1992. A pencil beam model for photon dose calculation. *Med. Phys.* 19: 263 – 273.
82. Ahnesjö a, Knoos T and Montelius A, 1992. Application of the convolution method for calculation of output factors for therapy photon beams. *Med. Phys.* 19: 295 – 301.
83. Wood J J and Mayles W P, 1995. Factors affecting the precision of TLD dose measurements using an automatic TLD reader. *Phys. Med. Biol.* 40(2): 309 – 313.
84. The use of plane parallel ionisation chambers in high energy electron and photon beams, an international code of practice for dosimetry, IAEA Technical Report Series 381. *International Atomic Energy Agency, Vienna, Austria, 1997.*
85. American Association of Physicists in Medicine, Task Group 39. The calibration and use of parallel plate ionisation chambers for dosimetry of electron beams: an extension of the 1983 AAPM protocol. *Med. Phys.* 21: 1251 – 1260.
86. Hospital Physicists Association, 1985. Code of practice for electron beam dosimetry in radiotherapy. *Phys. Med. Biol.* 30: 1169 – 1194.
87. Nisbet A, Thwaites D I, Nahum A E and Pitchford W G, 1998. An experimental evaluation of recent dosimetry codes of practice. *Phys. Med. Biol.* 43: 1999 – 2014.

88. Cecatti E R, Goncalves S G P and Silva M P, 1983. Effect of the accelerator design on the position of the effective electron source. *Med. Phys.* 10: 683 – 686.

